NTNU – Trondheim
Norwegian University of
Science and Technology

Method development and automated analysis of ultrasound images of phase-shift bubbles.

Snorre Sulheim

Master of Science in Physics and Mathematics	
Submission date:	Januar 2015
Supervisor:	Catharina de Lange Davies, IFY
Co-supervisor:	Annemieke van Wamel, IFY

Norwegian University of Science and Technology
Department of Physics

METHOD DEVELOPMENT AND AUTOMATED ANALYSIS OF ULTRASOUND IMAGES OF PHASE-SHIFT BUBBLES

SNORRE SULHEIM

Master of Science in Applied Physics
Department of Physics
The Faculty of Natural Sciences and Technology
The Norwegian University of Science and Technology

January 17, 2015

Supervisors:
Annemieke van Wamel
Andrew Healey
Professor Catharina de Lange Davies

PREFACE

This thesis concludes my Master of Science degree in Applied Physics at the Norwegian University of Science and Technology. The work has been conducted in collaboration with Phoenix Solutions AS and the Department of Physics at the Norwegian University of Science and Technology.

First, I would like to thank both Annemieke van Wamel and Andrew Healey for excellent supervising throughout this project. I appreciate that you let me take part in the very interesting development of the ACT™ concept. Annemieke van Wamel has provided crucial knowledge of microbubbles and tumors, in addition to daily help and support. Andrew Healey has contributed with indispensable enthusiasm, solutions to programming related problems, and knowledge of ultrasound physics. I would also like to thank Professor Catharina de Lange Davies for helpful supervising and proofreading. Finally, I wish to acknowledge my family and friends in Tindegruppa for proofreading and fruitful discussions.

ABSTRACT

Ultrasound mediated drug delivery is an important tool in the fight against cancer. A new concept called Acoustic Cluster Therapy (ACT™) is under development, and two pilot imaging studies have been performed on prostate cancer xenografts in mice. A large amount of raw ultrasound data has been recorded, but existing software can not perform the required image processing. The ACT™ concept is based on clusters of microbubbles and microdroplets. When exposed to diagnostic ultrasound, the microdroplets become microbubbles. This phase-shift from liquid to gas is followed by a microbubble growth to $\sim 30\,\mu\text{m}$. These phase-shift bubbles get stuck in the small capillaries of the tumor vasculature.

A complete program has been developed in MATLAB® to process the raw ultrasound data. The program is tailored to the unique properties of the phase-shift bubbles, and is able to reduce noise and motion artefacts, to visualize the contrast agent, and to count the number of ultrasound activated phase-shift bubbles. The program produces high quality videos, displaying both free flowing contrast agent and identified, stuck phase-shift bubbles.

The program was validated against a synthesized data set, and we found that the program counted accurately up to $\sim 2\,\text{bubbles}/\text{mm}^2$. A saturation was experienced above this threshold, and too few bubbles were counted.

The program was applied to a data set of 16 tumors, divided into four groups based on different ACT™ cluster dose and activation ultrasound settings. A significant difference ($p = 0.023$) was found between the different doses, while no significant difference ($p = 0.146$) was found between the different activation ultrasound settings. There was neither a correlation between the tumor size and the number of stuck phase-shift bubbles. The results show very good correlation with the resultss obtained from manual counting.

SAMMENDRAG

Bruk av ultralyd for å levere kreftmedisin lokalt i kreftvev er et viktig fremskritt innenfor kreftbehandling. Et nytt konsept kjent som Acoustic Cluster Therapy (ACT™) er under utvikling innenfor dette fagfeltet. ACT™ konseptet er basert på oljedråper og gassbobler i mikroskala, som holdes sammen ved hjelp av elektrostatiske krefter. Når klusterene eksponeres for ultralyd vil mikroboblene oscillere og overføre energi til mikrodråpene. Dette gjør at mikrodråpene fordamper og danner store gassbobler. Kreftmedisin kan løses i dråpene, og medisinen frigjøres når dråpene fordamper. De aktiverte gassboblene er store nok til å sette seg fast i kapillærene i kreftvevet i opptil flere minutter. Ved å gjennomføre to pilotstudier på prostata kreft implantert på mus, har man tilegnet seg ultralydbilder og film av disse gassboblene. Det finnes ikke tilfredsstillende programvare for behandling av disse ultralydbildene med identifisering av stasjonære gassbobler.

Et automatisert program er utviklet i MATLAB®, skreddersydd ACT™ konseptet, for å utføre den nødvendige prosesseringen. Den nyutviklede programvaren både visualiserer, identifiserer og teller stasjonære gassbobler, i tillegg til å redusere støy og bevegelse.

Et kunstig datasett, med et randomisert, kjent antall gassbobler, er konstruert basert på reelle ultralydbilder. Ved å behandle det kunstige datasettet har vi avdekket begrensningene til det utviklede programmet. Det viser seg at programmet teller riktig antall stasjonære gassbobler inntil $\sim 2\,\text{bubbles/mm}^2$. Over dette observeres en metning, og programmet teller for få bobler.

Ultralydbilder fra et *in vivo* studie på 16 tumorer er behandlet med dette programmet. De 16 tumorene er delt i fire grupper, basert på forskjell i konsentrasjon av ACT™ bobler og ultralydinnstillinger (mekanisk index) under behandlingen. Det er funnet en signifikant forskjell ($p = 0.023$) mellom antall stasjonære bobler i tumorene for høy og lav injisert dose ACT™ bobler. En signifikant forskjell ble derimot ikke funnet mellom de to forskjellige ultralydinnstillingene ($p = 0.146$). Stasjonære bobler i det samme datasettet er telt manuelt. Det er høy korrelasjon mellom de uavhengige resultatene fra manuell og automatisk databehandling.

CONTENTS

1

INTRODUCTION

Cancer is currently the most common cause of disease, with approximately 14.1 million new incidents worldwide every year (2012) [1]. In the United States, 1 of 4 deaths are caused by cancer [2], and only 50% of the persons diagnosed with cancer survive for 10 years.

The available treatments are rarely satisfying, giving limited results and negative side effects [3]. Chemotherapy, surgery, and radiotherapy are the main treatment options, often combined to achieve the best result. Chemotherapy is based on systemic administration of toxic drugs. These drugs damage healthy as well as cancerous tissue, limiting the dose to a survivable amount. This amount may be too low for the cancer to be successfully treated.

Targeted cancer treatment is an active field of research, where the goal is increased uptake of drug in cancerous tissue without harming healthy tissue. Several targeted treatments are already available, but none have so far been able to produce a precise, satisfying treatment. A reason to the limited success, is that the drug does not travel far enough into the tumor, after leaving the vasculature [4]. This leaves remote cancerous cells untreated.

Ultrasound may be the solution for precise and effective drug delivery. Microbubbles are already used as contrast agents in ultrasound examinations, and research has been conducted to use these bubbles as drug carriers as well. The main idea is to use ultrasound to trigger the release of the drug carried by the bubble. The drug might be loaded onto, or into, the shell encapsulating the microbubble. The thin shell of normal microbubbles is only able to carry small payloads. Therefore, thicker shells or different drug loading methods are under development [5][6].

Phoenix Solutions AS (Oslo, Norway) is developing a new concept for ultrasound mediated drug delivery. In this concept, clusters of encapsulated gas microbubbles and drug-loaded emulsion droplets, are used. When exposed to ultrasound, the microbubbles oscillate and initiate vaporization of the emulsion droplets. The phase-shift from liquid to gas releases the drug, and is followed by growth of the generated phase-shift bubbles to $\sim 30\,\mu\text{m}$. That is roughly ten times its initial size. These bubbles are large enough to block small vessels, keeping the drug present at the diseased site for an extended time. Low frequency ultrasound is applied, initiating oscillations of the large bubbles. Applying ultrasound together with microbubbles has been shown to enhance drug delivery through enhanced vessel permeability and sonoporation [7]. Similar mechanisms may be valid for the phase-shift bubbles. This new drug delivery concept is called Acoustic Cluster Therapy (ACT™), and can be regarded a theranostic (combining therapy and diagnostics) product. It is possible to image the clusters and phase-shift bubbles while performing drug delivery.

To test if the generation of the phase-shift bubbles can be done *in vivo*, an animal model is used. Prostate cancer xenografts located at the hind limb of mice, were subjected to ultrasound after intravenous injection of the ACT™ clusters. Phase-shift bubble activation was imaged using high frequency (16 to 18 MHz) ultrasound. These ultrasound images were recorded by Annemieke van Wamel and Andrew Healey.

Cancer tumors vary in size and vasculature, both between and within, different types of tumors. The vasculature may also vary between regions within a tumor. In order to proof a relationship between the ACT™ treatment and its anti-tumor effect, it is important to know the amount of drug deposited within the tumor. This amount depends on the number of stuck phase-shift bubbles. More stuck bubbles means more drug delivered, and more tumor tissue treated. By quantifying the number of stuck phase-shift bubbles after each treatment, it is possible to determine the optimal dose and ultrasound settings. The optimal dose and settings maximize the number of stuck phase-shift bubbles.

Currently the phase-shift bubbles are counted manually. That is time-consuming work, prone to subjectivity and lack of reproducibility. An automated program will increase the counting efficacy, and produce results with a known accuracy and precision. This will speed up the development of the ACT™ concept towards clinical trials.

Identification and counting of stuck bubbles in ultrasound images is a field of image processing with limited available literature. One approach is described by Needles et al., where microbubbles bound to vessel walls are differentiated from tissue and flowing microbubbles [8]. Subharmonic imaging is used to separate tissue and microbubbles, before a low-pass inter-frame filter is applied to remove the free flowing microbubbles. Because the large phase-shift bubbles have a weak subharmonic response, this method is not applicable. As far as we know, no other publicly available software is capable of counting the phase-shift bubbles.

Therefore, the main goal of this thesis is to develop a method to process the recorded data, and estimate the number of activated and stuck phase-shift bubbles, within the tumor. The developed method should produce high quality display and quantification of the phase-shift bubbles. Image processing involves motion correction, background subtraction and counting. The algorithm performing counting of phase-shift bubbles has to be validated, including an estimate of accuracy and precision. The algorithm should be applied to a data set containing ultrasound images of 16 tumors. The number of phase-shift bubbles in these 16 tumors has previously been counted manually by Andrew Healey. These manually obtained results will be used for comparison. A proper evaluation of the performance of the ACT™ concept is essential for further development toward clinical trials. This study should also investigate the effect of dose, tumor size and mechanical index on the number of stuck phase-shift bubbles.

2

THEORY

2.1 ULTRASOUND THEORY

Ultrasound is sound waves with frequency above 20 kHz, which is the upper limit of audible sound. For medical imaging, frequencies of 2 to 15 MHz are common [9]. In hospitals, ultrasound is a tool in daily use to image parts of the body. Like other medical imaging modalities - MR, CT, X-ray - energy is applied, and while the energy travels through the body, interactions occur. The image is then produced by measuring some aspect of the energy after the interactions. The image can successfully be created from knowledge of the energy before and after interaction, and from an understanding of the interaction mechanisms.

Ultrasound is generated by a transducer, and as the wave travels through the body, echoes are generated by partial reflection at every boundary. The amount of reflection depends on the relative change in acoustic impedance at the boundary. The echo is recorded by the transducer, and it is then displayed in the image according to its spatial origin. The speed of sound is approximately $1540\,\mathrm{m\,s^{-1}}$ for all soft body tissue, and it is thus possible to calculate the origin by measuring the time of travel of the echo [10].

The next sections review the major interactions of ultrasound with tissue; reflection, absorption and scattering. Then follows an overview of the interactions between ultrasound and microbubbles. The microbubbles interact strongly, and in a non-linear fashion even at moderate energies used for imaging.

2.1.1 *Imaging modalities*

Ultrasound images can be captured using several different modalities to enhance different properties of the tissue. The simplest modality is the amplitude-mode (A-mode), where a single element transducer is used to generate echoes along one line, and the received echoes are plotted as a function of depth. Brightness-mode (B-mode) use an array of transducers to generate a 2D (3D) map of a slice (volume) through the body, where the image brightness is proportional to the amplitude of the echo, originated from the corresponding location. Motion mode (M-mode) is generated from a sequence of A- or B-mode images to image tissue motion. Doppler imaging is another large field of imaging modes, where the Doppler effect is utilized to image the blood flow. This can be used to measure the velocity, direction and total blood flow. Non-linear imaging is another field of imaging modes used to enhance the visibility of contrast agents [10]. This is described in more detail in Section 2.1.10.

2.1.2 *Linear ultrasound wave propagation*

This section follow the general review given in the book *Ultrasound scattering in biological tissue*, written by Shung and Thieme [11]. Sound is pressure waves, and the pressure fluctuations cause temporal displacement of the medium, in which the wave is travelling. For most imaging purposes the displacement is along the direction of travel, this is called longitudinal waves. Solids can support transverse sound waves, but that is outside the scope of this thesis. The wavelength, λ, is determined by the frequency of the source and the phase velocity in the medium, c, i.e. $\lambda = {}^{c}/_{f}$. The phase velocity c is given by

$$c = \sqrt{\frac{1}{\rho\kappa}}, \tag{2.1}$$

where ρ and κ are the tissue density and compressibility, respectively [12]. The compressibility is a measure of the relative change in volume from change in pressure, that is $\kappa = -\frac{1}{V}\frac{\partial V}{\partial p}$. Here V is volume and p is pressure.

The propagation of a sound wave travelling in the x-direction can in a fluid be described by the wave equation, i.e.

$$\frac{\partial^2 W}{\partial x^2} = \frac{\rho_0}{G}\frac{\partial^2 W}{\partial t^2}. \tag{2.2}$$

Here W is the particle displacement, ρ_0 the density of the medium and G the bulk modulus [10]. The bulk modulus is the reciprocal of the compressibility, and is a measure of the volume stiffness. A general solution to this equation is

$$W = W_0 \exp^{i(kx-\omega t)}, \tag{2.3}$$

where ω is the angular frequency, $k = \omega/c$ the wave number, and c the phase velocity as given in Equation (2.1), with κ substituted by $1/G$. The pressure variations is then given by particle velocity $u_x = \frac{\partial W}{\partial t}$ as

$$p_x = \rho_0 c u_x. \tag{2.4}$$

It is important to emphasize the difference between the phase velocity and the particle velocity. The phase velocity is the velocity of energy carried through the medium, while the particle velocity is the velocity of the local displacement of particles.

The acoustic impedance Z of the medium is defined as the ratio between the excess pressure and the particle velocity,

$$Z = \frac{p}{u}. \tag{2.5}$$

Here $u = \vec{u} \times \vec{n}$ is a speed obtained from the real particle velocity $\vec{u}$ and the unit vector $\vec{n}$ of the direction of propagation. If we consider a forward travelling, plane wave the equation reduces to

$$p = \rho c = \sqrt{\frac{\rho}{K}}, \tag{2.6}$$

where ρ is the density and K the compressibility [13]. This is known as the characteristic acoustic impedance.

2.1.3 *Non-linear behaviour*

Until now, we have only considered the linear behaviour for both the wave propagation and the bubble scattering and oscillation. A brief review of non-linear wave propagation follows. This review is based on previous work by Duck [14] and Hoff [15].

When the amplitude of the acoustic wave exceeds ~1 MPa, non-linear propagation become noticeable [14]. Non-linear effects can be divided into local and cumulative. Local effects are displacement of vibrating sources and differences in the relationship between pressure and particle velocity. Local effects are regarded as negligible, except for oscillating microbubbles where there is a change in the pressure/bubble radius relationship [14].

Cumulative effects are caused by differences in the propagation speed at different locations in the wave. At the peak pressure, the tissue will be compressed, increasing the speed of sound. In the region of rarefaction, the propagation speed is decreased. This causes distortion of the waveform, which will develop with distance (Figure 2.1). The compression peak will move in the direction of propagation, while the rarefaction peak moves in the opposite direction. This will decrease the distance between the two peaks, until they are coincident and we get a discontinuity of the wave.

The distortion of the waveform generates high frequency components in the pulse frequency spectrum. These high frequency components appear at multiples of the fundamental frequency f_0, and are called harmonic frequencies (Figure 2.2). As the wave propagates further the high frequencies are more attenuated, and the wave will eventually regain its shape with a reduced amplitude.

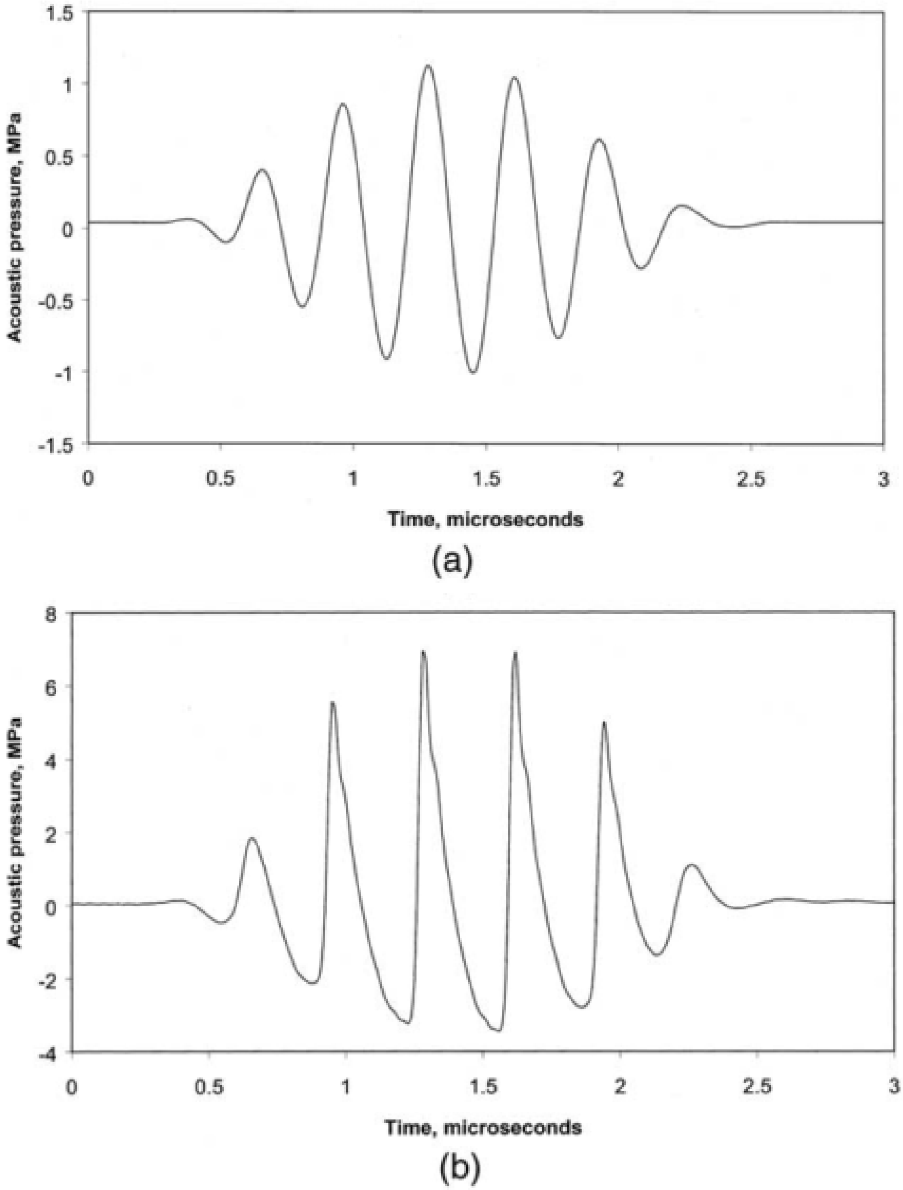

Figure 2.1: The measured focal waveform of a 3 MHz Doppler pulse in water for low acoustic pressure (a) and a pulse where the pressure is increased by 24 dB. The distortion of the waveform is easily seen in (b) [14].

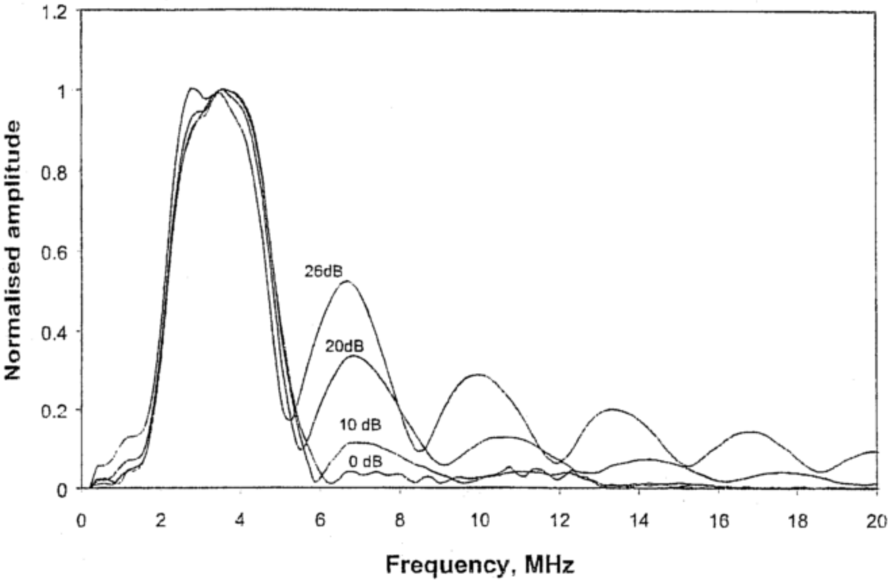

Figure 2.2: Development of harmonic frequencies as the amplitude of the source is increased by 10, 20 and 26 dB from a near-linear situation. Measured at the focus of a 3.5 MHz wave [14].

2.1.4 *Reflection*

The following three sections cover wave attenuation, i.e. reflection, absorption, and scattering. These sections follows the corresponding sections written by Healey [13].

Reflection provide the basis for ultrasound imaging, and occurs when the wave encounter a planar surface with a change in acoustic impedance. Across this surface, both the pressure and particle velocity have to be continuous. From these boundary conditions the intensity coefficients of the reflected wave, r_i, and transmitted wave, t_i, can be given as [16]

$$r_i = \left(\frac{z_2 \cos\theta_i - z_1 \cos\theta_t}{z_1 \cos\theta_t + z_2 \cos\theta_i} \right)^2 \tag{2.7}$$

$$t_i = \frac{4 z_2 z_1 \cos^2\theta_i}{(z_2 \cos\theta_i + z_1 \cos\theta_t)^2}. \tag{2.8}$$

Here z_1 and z_2 are the acoustic impedance in medium 1 and 2(Figure 2.3). The angle of reflection θ_r is equal the angle of incidence θ_i, while the angle of transmission θ_t is given by Snell's law [17], $c_2 \sin\theta_i = c_1 \sin\theta_t$.

2.1.5 *Absorption*

Loss of kinetic energy to heat from the propagating wave to the surrounding medium is known as absorption. Absorption occurs continuously and reduces the amplitude of the wave. For linear propagation of a pressure wave, this can be described as

$$p(x) = p(0) \exp^{-\alpha_A(\omega) x}, \tag{2.9}$$

where $p(0)$ is the initial pressure amplitude, α_A the absorption coefficient and ω the angular frequency.

For non-linear propagation, the absorption depends on the local amplitude. In the diagnostic intensity range, the non-linear interaction is proportional to the square of the intensity [18]. Non-linear propagation also affects the shape and frequency spectrum of the propagating wave, and can usually not be ignored for contrast agent applications [13].

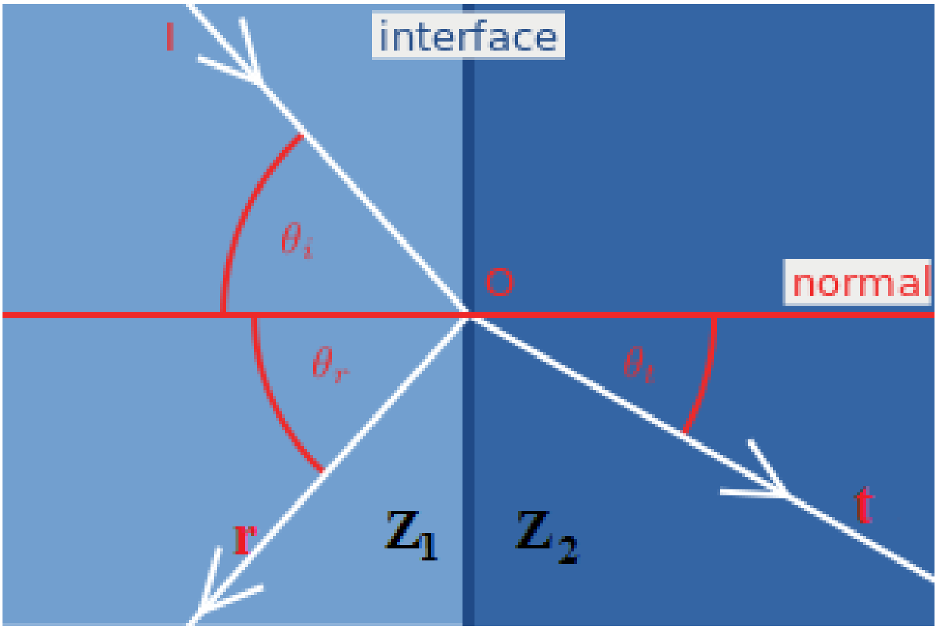

Figure 2.3: Reflection (r) and transmission (t) of an incoming pressure wave at an interface between two tissues with acoustic impedance z_1 and z_2.

2.1.6 *Scattering*

Scattering is reflection that occurs when the size d of the surface encountered is comparable to or smaller than the wavelength. Scattering can arise from inhomogeneity in compressibility, density or absorption. Scattering reflects the wave in a large range of directions, and the backscattered signal received at the transducer is therefore weak compared to reflected echoes. The magnitude and direction of the scattering depends on the size of the scatterer and increase strongly with the frequency.

If we consider an incoming plane wave propagating in the direction $\hat{i}$ (Figure 2.4), the incident pressure, p_i, at the scatterer located at $\mathbf{r}_0$ is then

$$p_i(\mathbf{r}_0, t) = p_0 \exp^{i(\mathbf{r}_0 \mathbf{k}_i - \omega t)} . \tag{2.10}$$

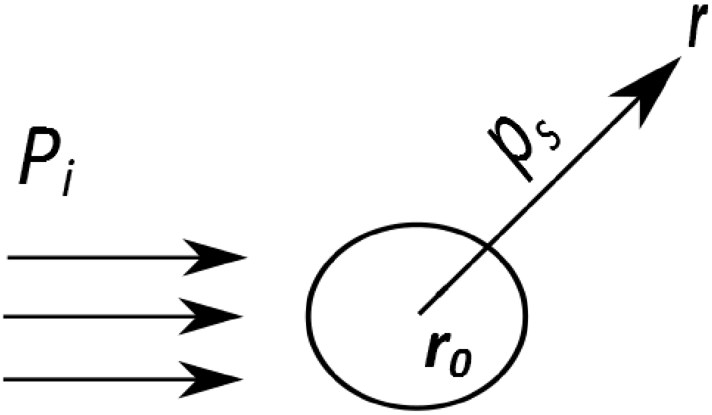

Figure 2.4: The scattered wave p_s due to incident pressure wave p_i and scatterer at $\mathbf{r}_0$.

If we only consider the far field, the scattered wave, p_s, at the observer at position $\mathbf{r}$ is given by [13]

$$p_s(\mathbf{r},t) = f(\hat{r},\hat{\imath})\frac{\exp^{ik_s(\mathbf{r}-\mathbf{r}_0}}{|\mathbf{r}-\mathbf{r}_0|}p_i(\mathbf{r}_0,t). \tag{2.11}$$

The $f(\hat{r},\hat{\imath})$ is the scattering amplitude function. The scattered intensity is

$$I_s = \frac{1}{2}\frac{|p_s|^2}{\rho c} = \frac{1}{2}\frac{|p_i|^2}{\rho c}\frac{\left|f(\hat{r},\hat{\imath})^2\right|}{|\mathbf{r}-\mathbf{r}_0|^2} = I_i\frac{\left|f(\hat{r},\hat{\imath})\right|^2}{|\mathbf{r}-\mathbf{r}_0|^2}, \tag{2.12}$$

where I_i is the incident intensity. The differential scattering cross-section is defined as $\sigma_d = |f(\hat{r},\hat{\imath})|^2$. The scattering cross section is the integral of the differential cross section over all solid angles, i.e.

$$\sigma_s = \int_{4\pi}\sigma_d \mathrm{d}\Omega. \tag{2.13}$$

The Rayleigh scattering model is the simplest model for scattering of small particles, i.e. particles with a diameter $d << \lambda$. This model does not consider damping or resonance effects. If we again consider the plane wave, the differential scattering cross section is given by [19]

$$\sigma_d = k^4 a^6 \left[\frac{G - G_0}{3G} - \frac{\rho - \rho_0}{2\rho + \rho_0} \cos\theta \right]^2 . \tag{2.14}$$

The total cross-section is obtained using Equation 2.13 and 2.14,

$$\sigma_s = 4\pi k^4 a^6 \left[\left(\frac{G - G_0}{3G} \right)^2 + \frac{1}{3} \left(\frac{\rho - \rho_0}{2\rho + \rho_0} \right)^2 \right] . \tag{2.15}$$

In these equations k is the wavenumber, a the radius of the scatterer, and the zero subscript refers to properties of the surrounding medium. The angle θ is the angle between the incident wave and the scattered wave, i.e. $\theta = 180°$ is the direction of backscattering. Although these equations represent a coarse approximation, it demonstrates why gas bubbles are excellent contrast agents. The density term in Equation (2.15) is limited to 1/3, while the bulk modulus term has no upper limit as G gets small compared to G_0. Thus, it is the compressibility and not the acoustic impedance that is the main cause of the scattering off a gas bubble. This is shown in Figure 2.5.

It is important to keep in mind that the compressibility term in Equation 2.14 is a monopole, so for gas based microbubbles monopole scattering will dominate. In a solid medium, such as steel, with low compressibility and high density, the scattering is dominated by the dipole term. Differential scattering cross sections for spheres of steel and air is plotted in Figure 2.6.

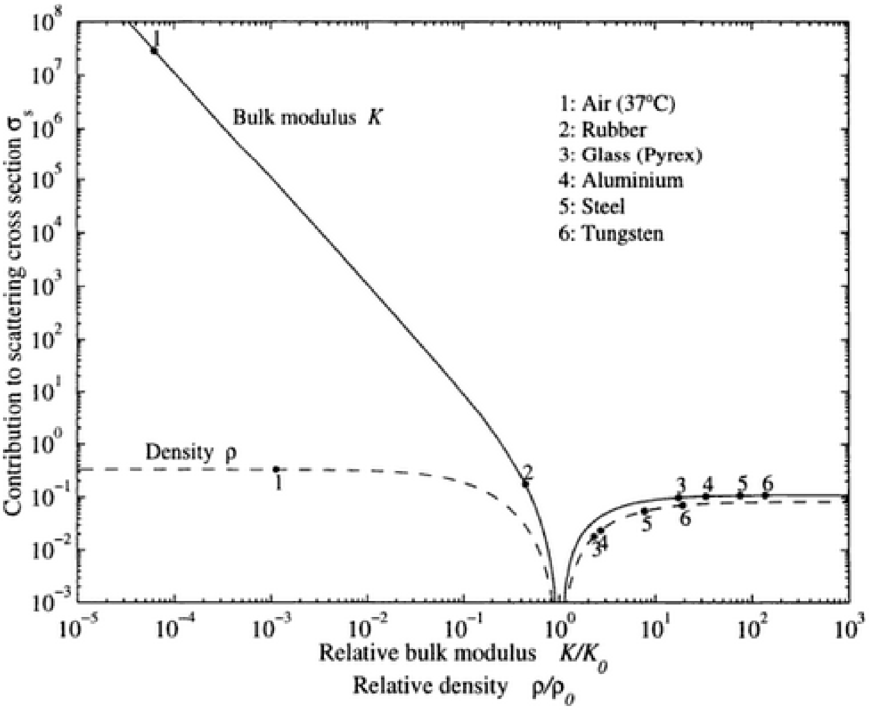

Figure 2.5: Contribution to Rayleigh scattering cross section from relative bulk modulus and density, corresponding to Equation 2.15 [15]. The solid and dashed line describe the bulk modulus and density, respectively. The numbers refer to the different materials. Note the logarithmic scaling on both axis.

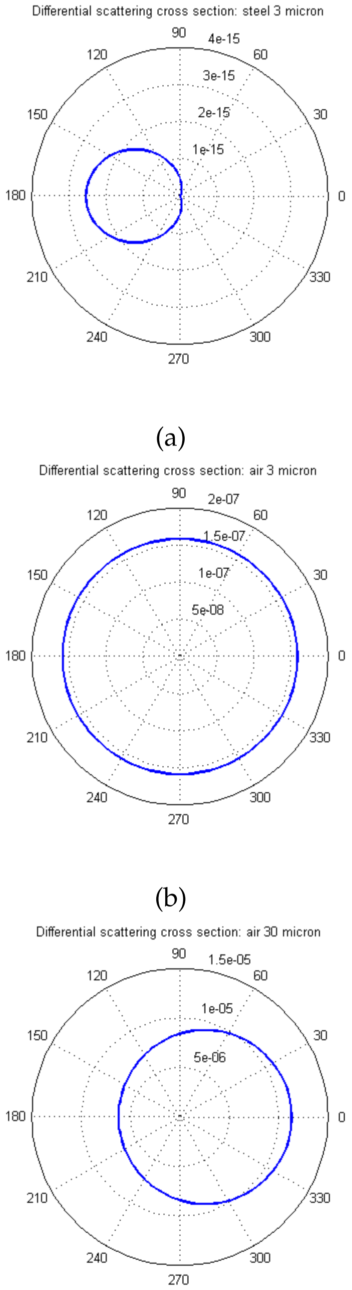

Differential scattering cross section: steel 3 micron

(a)

Differential scattering cross section: air 3 micron

(b)

Differential scattering cross section: air 30 micron

(c)

Figure 2.6: Differential cross section for a 3 µm sphere of steel (a) and air (b), and for a 30 µm sphere of air (c) [13]. The dipole term dominates in (a) while the monopole term dominates in (b). In (c) there is more of a balance between the monopole and dipole term.

2.1.7 *The bubble as a linear oscillator*

This section follows the derivation of the bubble as a linear oscillator by Hoff [15], which contains a full review of subject: acoustic properties of contrast agents. To include the effects of damping and resonance, the microbubble can be modelled as a harmonic oscillator. Comparing the bubble with a mass/spring system (Figure 2.7), the gas pressure, surrounding liquid and radiation resistance corresponds to the spring, mass and dash-pot, respectively. The limitation for linear oscillations is that the radial displacement of the bubble wall is small compared to the bubble radius.

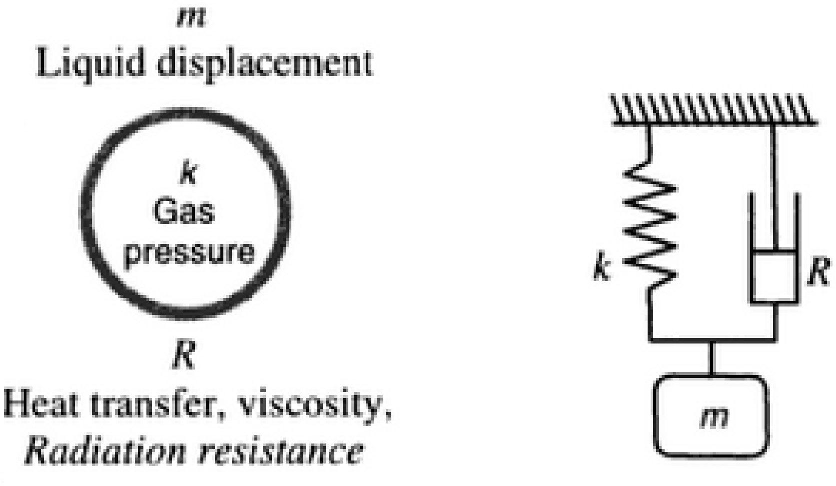

Figure 2.7: The bubble as a harmonic oscillator, in comparison to the mass/spring system [15].

As the bubble oscillates, both the gas inside, and the liquid outside the bubble, add inertia to the system. Due to the relative low density of the gas, this contribution can be neglected. The gas inside the bubble acts against any volume change of the bubble, thus acting as the spring in the system. The damping of the system is caused by heat transport to the surroundings, radiation of sound and by the viscosity of the liquid. If we consider a bubble with a shell, viscous forces in the shell contribute to the damping.

For this system, the resonance frequency f_0 is given as [15]

$$f_0 = \frac{\omega}{2\pi} = \frac{1}{2\pi a}\sqrt{\frac{3\kappa p_0}{\rho} + \frac{12 G_s d_s}{a}}. \tag{2.16}$$

Here a is the bubble radius, G_s and d_s the shear modulus and thickness of the shell, p_0 the atmospheric pressure and κ the polytropic exponent of the gas. The polytropic exponent is equal to the adiabatic constant γ when the oscillations are adiabatic, while it is the unity for isothermal conditions. This depends on the bubble radius and signal frequency [15]. The second term on the right-hand side of Equation (2.16) is the contribution from the shell to the bulk modulus of the system.

The scattering cross section is

$$\sigma_S = 4\pi a^2 \frac{\Omega^4}{(1-\Omega^2)^2 + (\Omega\delta)^2}, \tag{2.17}$$

where $\Omega = \omega/\omega_0$ and δ the damping constant of the system. The scattering cross section for air and Sonazoid™ (Section 2.1.9) microbubbles is plotted in Figure 2.8 and 2.9. We observe that the presence of a shell increase the resonance frequency and broadens the resonance peak [13]. There is also a difference in acoustic response for large and small bubbles at low frequencies. This allows imaging of the large ACT™ bubbles at lower frequencies and with fundamental B-mode. The resonance frequency is reduced for increased bubble size.

2.1.8 *The bubble as a non-linear oscillator*

In general, the non-linear response from a microbubble is not negligible. Actually, it is the property of interest, when used as contrast agents in diagnostic imaging (Section 2.1.10). A brief review of the non-linearity of bubble oscillations is given below. A full review is outside the scope of this thesis, and the interested reader is addressed to the dissertation written by Hoff [15].

Compared to tissue, the non-linear response from microbubbles is large, and further increased by the coincidence of the resonance frequency being in the range of frequencies used in diagnostic imaging. The response from the contrast agent Optison™ is shown in Figure 2.10, where presence of harmonic peaks proves the non-linear behaviour of the microbubble [20][21].

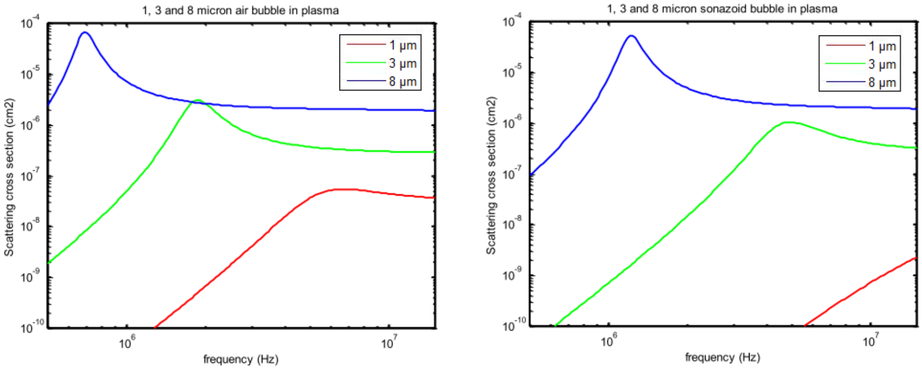

Figure 2.8: Left: Log-log plot of the scattering cross section σ_S for air bubbles with diameter 1, 3 and 8 µm. Right: Corresponding plot of Sonazoid™ bubbles [13].

The non-linear dynamics of a spherical bubble in an infinite, incompressible fluid can be described by the Rayleigh-Plesset equation,

$$\frac{p_{r_0}\left(\frac{r_0}{r_b}\right)^{3\gamma} - p_0 - p(t)}{\rho_l} = \frac{3\dot{r}_b^2}{2} + r_b\ddot{r}_b. \tag{2.18}$$

where $r_b = r_b(t)$ is the bubble radius as a function of time, and $\dot{r}_b$ and $\ddot{r}_b$ the velocity and acceleration of the bubble wall, respectively. This is an ordinary differential equation that can be solved with initial conditions $r(0) = r_0$, and $\dot{r}_b = 0$ [22]. A derivation of the Rayleigh-Plesset equation is presented in Appendix A.

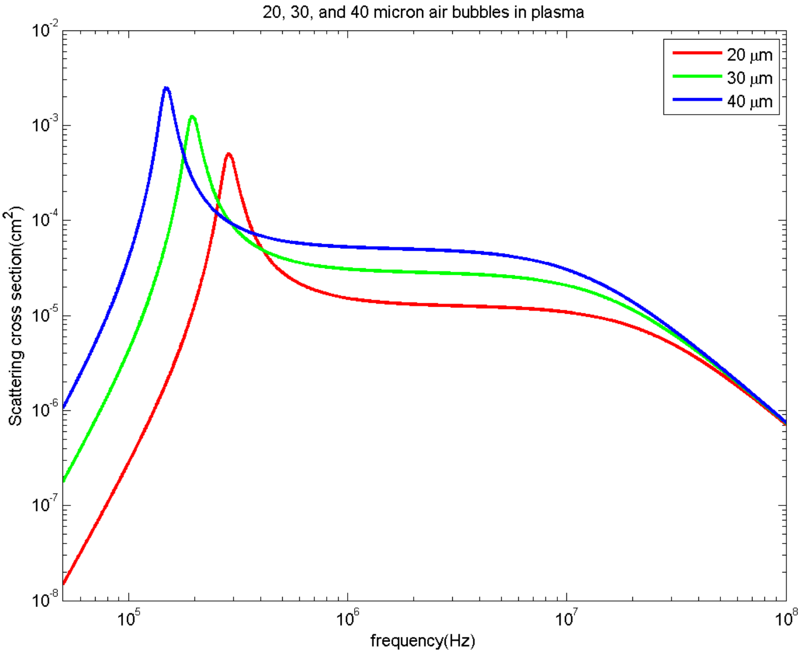

Figure 2.9: Log-log plot of the scattering cross section σ for air bubbles with diameter 20, 30 and 40 µm [13].

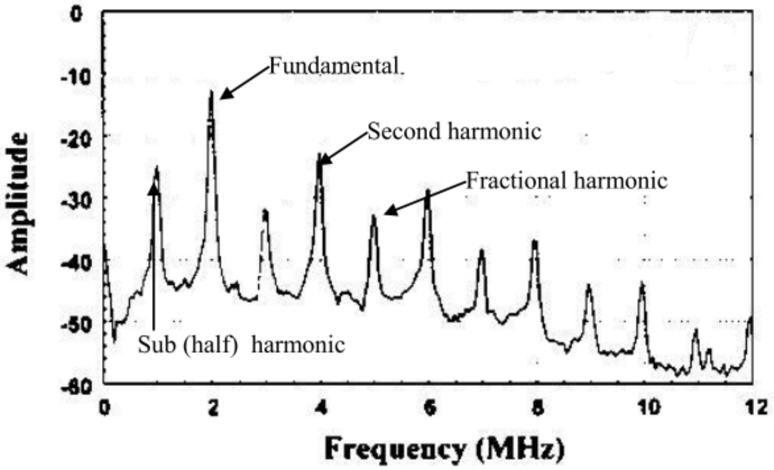

Figure 2.10: Spectrum of scattered signal from an Optison™ microbubble, exposed to a signal with a fundamental frequency of 2 MHz. The other peaks are due to the non-linear response of the bubble [21].

2.1.9 *Contrast agents*

Contrast agents are used to increase the image sensitivity and signal-to-noise ratio in medical imaging of blood. In ultrasound imaging, this is accomplished by intravenous injection of a solution containing gas-filled microbubbles [23]. Microdroplets are also under development [24], but not in pre-clinical trials, and therefore outside the scope of this thesis. Microbubbles are preferred because of the higher echogenicity [25].

The microbubbles have to fulfil several requirements to perform as a contrast agent. The contrast agent has to be delivered to the area of interest, and this set requirements to circulation time and size. The diameter has to be smaller than 8 µm to pass the pulmonary capillary that is the size limiting factor in the circulatory system [26]. Strong backscattering of ultrasound is important. Absorption is an unwanted effect as it attenuates the ultrasound wave without contributing to the received signal. It is also important that the contrast agent is well tolerated by the body and is able to leave the circulatory system either by dissolving or by being phagocytosed by the Kupfer cells in the liver [13].

In the 1960s, the cardiologists started using contrast agents that were made of saline [27]. The saline was shaken before injection to create microbubbles. Current available contrast agents have been able to fulfil the requirements stated, and consist of a gas enclosed in a shell. The shell has to be biocompatible ,and can be made of lipids, proteins or polymers. The advantage of a shell is increased circulation time and scattering of ultrasound. Increased circulation time is also promoted by the gas core. The gas should dissolve slowly in blood, and may be of Nitrogen or Perfluorocarbons [28]. The size of the microbubbles is approximately smaller or equal to red blood cells, i.e. 2 to 6 µm (Figure 2.12).

The gas-filled microbubbles used as contrast agents are comparable to air bubbles in terms of density and compressibility, and from Figure 2.5 we observe that the scattering cross section is completely dominated by the compressibility term. The ultrasound pressure fluctuations caused by the ultrasound, forces the microbubble to expand and contract in a non-linear fashion. The microbubble is in fact a chaotic oscillator, and the onset of the chaotic response is mainly determined by the thickness of the shell [29]. For a free gas bubble (no shell) the chaotic oscillation of the bubble wall is shown in Figure 2.11. For common contrast agents the non-linearity is present at diagnostic frequencies.

The use of contrast agents has been limited to diagnostics, but these microbubbles possess properties suited to therapeutic use [30]. The microbubbles can serve as drug carriers for ultrasound mediated drug delivery [31], see Section 2.2.5.

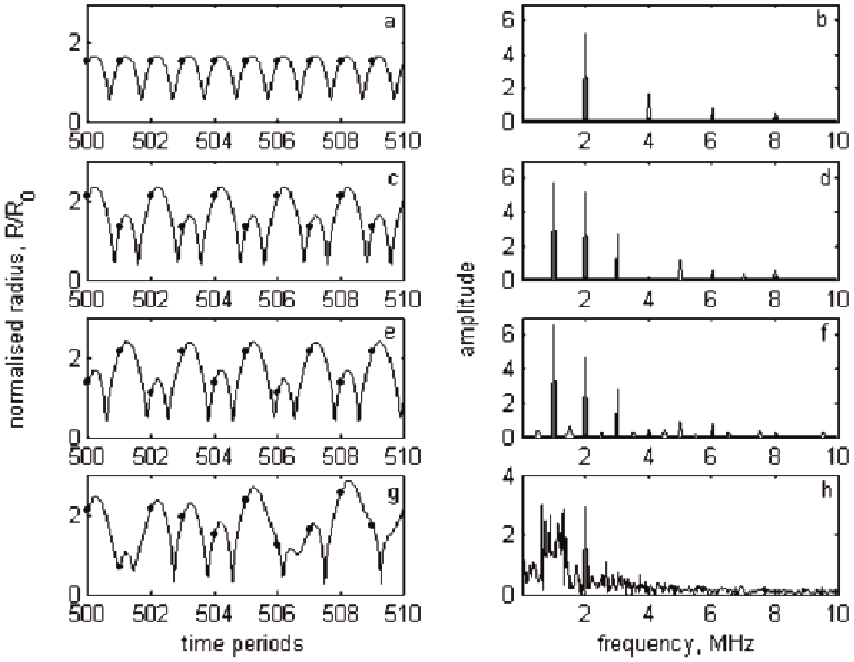

Figure 2.11: Left: The relative radial response($R(t)/R_0$) of a free gas bubble of 4 µm diameter, subject to a pressure wave of 2 MHz with driving pressure amplitude of 100, 250, 265, and 320 kPa, increasing from top to bottom. Right: The corresponding frequency spectrum [29].

Sonazoid™ is a contrast agent that has overcome all requirements stated above, with a well-characterized structure and size distribution (Figure 2.12). There is a core of perfluorobutane gas, with a 4 nm thick lipid monolayer shell with shear modulus and viscosity equal (50 ± 3) MPa and $(0.8 \pm 0.1)\,\mathrm{N\,s\,m^{-2}}$, respectively [15]. The density of the perfluorobutane gas core is $0.0098\,\mathrm{g\,cm^{-2}}$, while the thermal diffusivity is $0.07\,\mathrm{cm^2\,s^{-1}}$ [13]. The shell is a membrane of hydrogenated egg phosphatidyl serine (HEPS) [32].

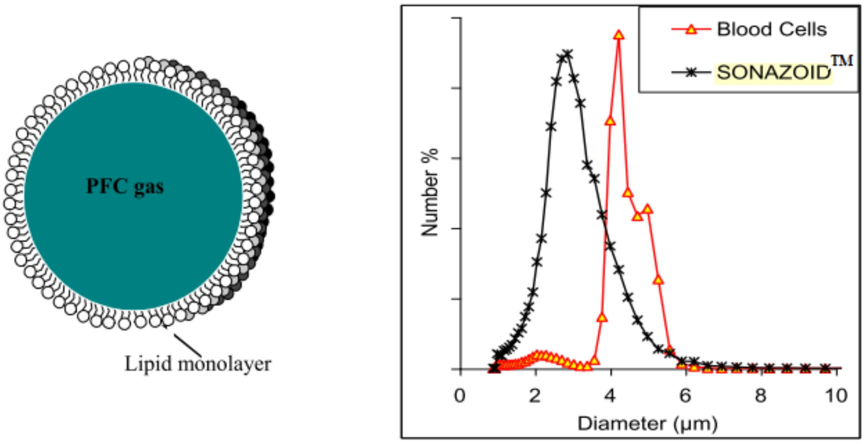

Figure 2.12: Left: The structure of Sonazoid™ , i.e. perfluorobutane gas encapsulated in a lipid monolayer. Right: Size distribution of Sonazoid™ and red blood cells [13].

2.1.10 *Contrast enhanced imaging*

This section follows the description of non-linear imaging written by Flower [10] and Hoskins et al. [9]. The non-linear behaviour is almost absent in normal tissue, while it is large in microbubbles. Therefore, non-linear techniques are often applied to enhance the contrast-to-tissue signal ratio. The main difference between the non-linear imaging techniques is the applied mechanical index. The mechanical index (MI) is defined as $\mathrm{MI} = {}^{P_-}/\sqrt{f_c}$, where P_- and f_c is the peak negative pressure, and the pulse centre frequency, respectively. The MI describes the potential for mechanical effects due to acoustically driven microbubbles. For high-MI images, the acoustic pressure is large enough to destroy most of the microbubbles in the imaging plane, and release free gas bubbles. This creates a short flash of high contrast. In low-MI images (MI 0.05 to 0.1) few of the bubbles are disrupted and the non-linear scattering properties are used to form images. Different low-MI techniques are described below.

Low-MI techniques can be divided into two fundamentally different methods. The first method utilizes frequency filtering in the frequency-domain. This is applied in second harmonic imaging, where the transducer bandwidth covers both the fundamental transmit frequency, and the second harmonic

(Figure 2.13). Even at moderate pressure (0.1 to 0.3 MPa) microbubbles generate harmonic frequencies, while the tissue response is mainly linear. The fundamental frequency is excluded from the recorded signal by a high-pass filter, and this increases the contrast-to-tissue ratio. The required bandwidth of the transducer gives limitations to the spatial resolution.

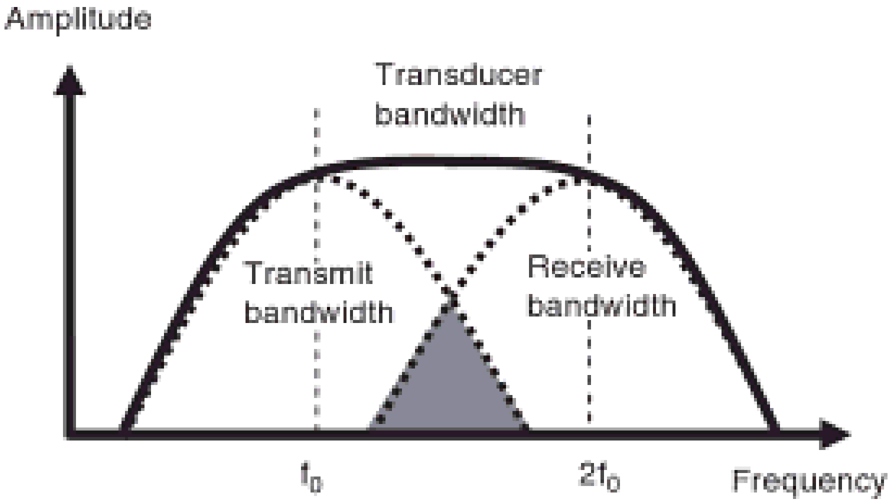

Figure 2.13: The transducer used in second harmonic imaging. The bandwidth cover both the fundamental frequency f_0 and the second harmonic $2f_0$ [9].

The second method enhance the non-linear response through scaling and subtraction of the received and transmitted pulses in the time-domain. Phase inversion is a technique using two pulses, where the second pulse is 180° out of phase with the first pulse (Figure 2.14). When the two received signals are added, the linear part sum to zero because of the linear response to the applied pressure. The microbubbles are the principal source of the non-linear part of the image, and they are therefore emphasized by this technique.

Amplitude modulation is a technique using two or three pulses with different amplitudes (Figure 2.15). The tissue will respond linearly to the amplitude, while the non-linear response from the microbubbles increase dramatically to the increased amplitude. The linear response can be removed by subtracting the received signals. A combination of the phase-inversion and the amplitude modulation is also possible.

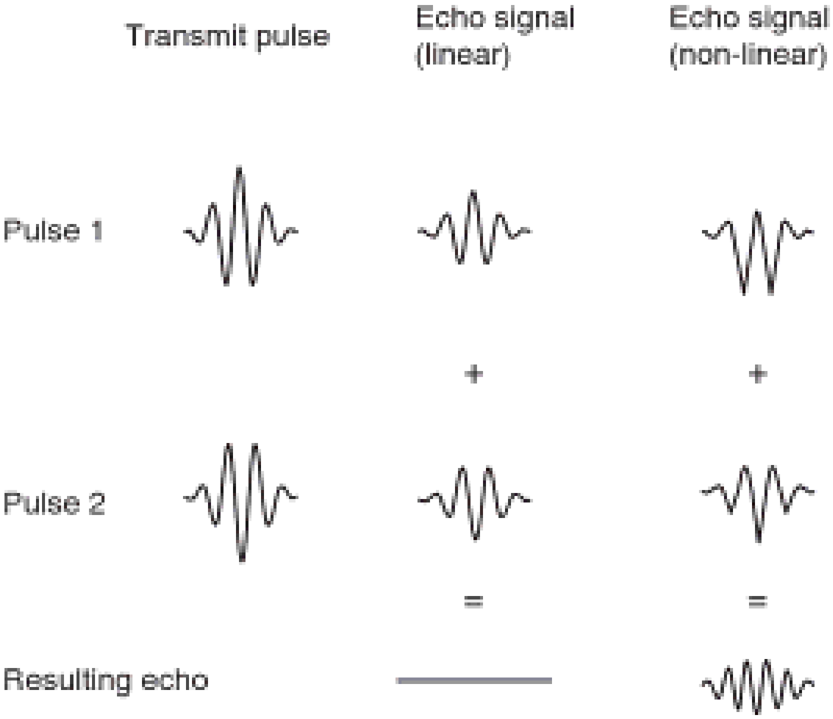

Figure 2.14: The two signal pulses used in phase-inversion are 180° out of phase. The non-linear signal is obtained from the sum of the two received signals [9].

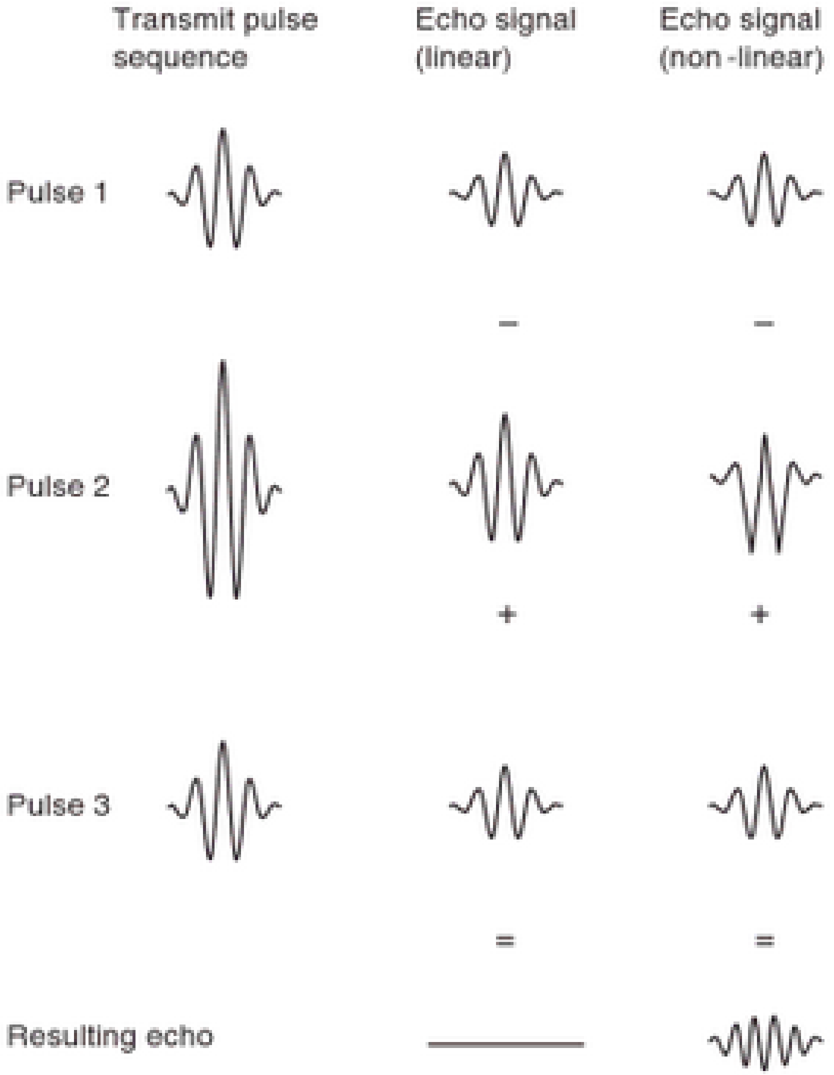

Figure 2.15: This amplitude modulation is based on three pulses where the first and last pulse have half the amplitude of the second pulse. The linear signal part of the signal is suppressed by subtracting the second pulse from the sum of the first and last pulse [9].

2.1.11 *Phase-shift bubbles*

This description of the phase-shift bubbles follows the review written by Healey [33]. The drug carrier used in this project is a two-component particle, composed of negatively charged gas microbubbles and positively charged emulsion droplets. This concept is called Acoustic Cluster Therapy (ACT™) and is illustrated in Figure 2.16. Both the gas microbubble and the droplet have an initial size about 2 to 3 µm. The gas microbubble consist of a low solubility perfluorocarbon gas encapsulated in a negatively charged phospholipid membrane, e.g. Sonazoid™. The emulsion droplet consist of perfluoro-methylcyclopentane (pf-MCP), stabilized by a positively charged phospholipid membrane. A chemotherapeutic drug can either be dissolved in the perfluorated oil phase or be co-administrated with a non-loaded cluster dispersion. When the bubbles and droplets are mixed, clusters of droplets and bubbles will form due to electrostatic, attractive forces.

When the clusters are exposed to ultrasound of standard medical frequency (1 to 5 MHz) and intensity [9], the microbubble will oscillate and transfer energy to the droplet through mechanical interactions at the boundary. This initiates a fusion into a gas and liquid mixture, encapsulated by a mixed surfactant membrane. The fluid will vaporize and expand to a gas bubble of approximately 30 µm. If drug is dissolved in the droplet, it is released upon vaporization. The enlarged gas bubble can block the capillary network and maintain the local concentration of the released drug.

If we assume rapid thermal conduction from surrounding blood, the partial pressure of the pf-MCP is close to the vapour pressure at body temperature. This vapour pressure is lower (∼14 to 22 kPa)[1] than the local hydrostatic pressure, and initially, the difference is equalized by the gas from the microbubble. An inward diffusion of the main gases dissolved in blood (i.e. O_2, N_2, CO_2, H_2O and Ar) will exist simultaneously. These gases will contribute to the equalization of the hydrostatic pressure. The inward diffusion is driven by partial pressure gradients of the respective gases.

The evaporation will not occur if the blood is under-saturated of the previously mentioned gases. Excessive hydrostatic pressure inside the bubble will reduce the pressure gradient and may halt the evaporation. This may occur because of excessive surface tension or high hydrostatic pressure in the surrounding blood. The initial evaporation occurs in less than a millisecond. The inward diffusion may continue after the evaporation, until a maximum size is reached

---

[1] Vapor pressure of pf-MCP at body temperature: 76 kPa. Blood gas partial pressure in arterial and venous blood, respectively: 98 kPa and 90 kPa [33].

after approximately 20-30 seconds [34]. After the bubble has reached its maximum size, it will dissolve within minutes (Figure 2.18).

Application of low MI and low frequency (0.1 to 2 MHz) ultrasound onto the phase-shift bubbles initiate oscillations and has shown to increase the drug accumulation in tissue [35]. We know that ultrasound can initiate microbubble oscillation and increase cell membrane permeability for macromolecules [7]. The oscillating phase-shift bubbles may activate the same mechanisms.

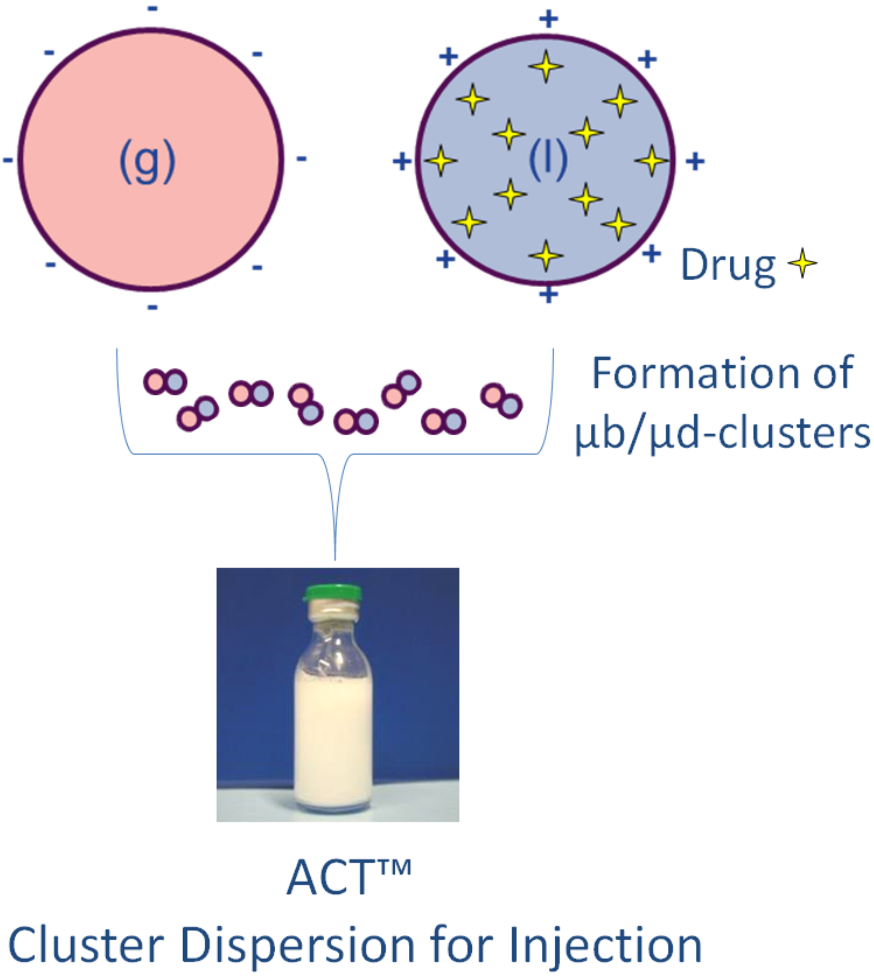

Figure 2.16: Illustration of phase-shift bubble, with the gas microbubble (left) and microdroplet (right). The drug (yellow) is dissolved in the microdroplet.

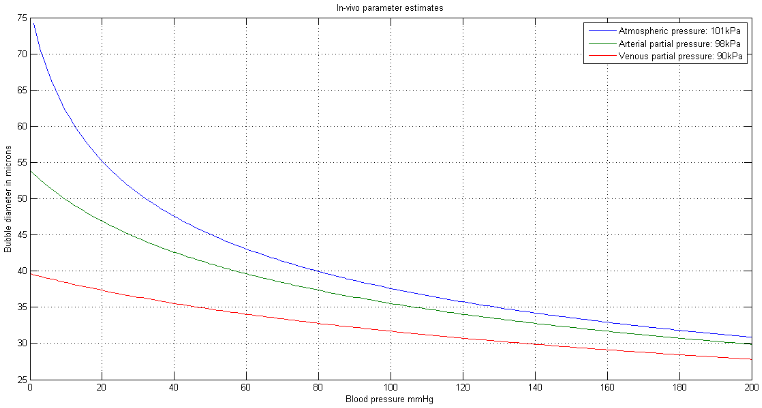

Figure 2.17: Estimated phase-shift bubble diameter *in vivo* for a oil droplet of initial size 4 µm. Arterial and venous partial gas pressure is plotted with atmospheric pressure for comparison. We see that the size of the phase-shift bubble is reduced by increased blood pressure.

A more mathematical description of the evaporation is given below and follows the derivation from Healey [33]. It is important to emphasize that this is a simplified description, and only used to make rough predictions about bubble size and lifetime.

We assume that we can use the simplification of ideal gases, i.e. we can use the ideal gas law

$$pV = nRT. \tag{2.19}$$

Here, p is the pressure of the gas, V is the volume of the gas, n the amount measured in moles, R is the gas constant and T the body temperature. Hence, the volume of the evaporated gas is a function of the initial volume and pressure in the oil droplet, i.e.

$$V_g(V_{pf}, p_{pf}) = \frac{n_{pf}RT}{p_{pf}} = \frac{V_{pf}\rho_{pf}RT}{M_{pf}p_{pf}}. \tag{2.20}$$

The subscripts g and pf denotes the gas bubble and oil droplet, respectively. Presumed that both the gas and liquid bubble are spherical, we have a simple relation between the diameter, d, and the volume, $V = \frac{\pi d}{6}$. Using this relationship, Equation (2.20), and assume no surface tension, we get an expression for the diameter of the gas bubble,

$$d_g(p_{pf}, d_{pf}) = d_{pf}\sqrt[3]{\frac{\rho_{pf}RT}{M_{pf}p_{pf}}}. \tag{2.21}$$

Here, ρ_{pf} and M_{pf} are the density and molecular mass of the oil droplet (pf-MCP). From this equation we can get the size of the gas bubble after the initial evaporation. From an initial diameter of 4 µm we get a maximum diameter of about 23.4 µm, knowing that the vapour pressure of pf-MCP at body temperature is 76 kPa [33].

To include surface tension, γ, we use the Young-Laplace equation for a sphere [36],

$$\Delta p = \gamma\frac{4}{d}. \tag{2.22}$$

The pressure in the surrounding fluid is then

$$p_w = p_{partial} + p_{pf} - \gamma\frac{4}{d_g(p_{pf}, d_{pf})}. \tag{2.23}$$

Here p_w and $p_{partial}$ are the total and partial pressure in the surrounding fluid, respectively. Combining the equations given above, we get a cubic expression of the gas bubble diameter,

$$(p_w - p_{partial})d_g^3 + 4\gamma d_g^2 - \frac{6v_{pf}\rho_{pf}RT}{\pi M_pf}. \tag{2.24}$$

This equation has a real solution, and can be used to calculate an upper limit of the phase-shift gas bubble diameter. For a droplet of 4 µm diameter we get a maximum bubbles diameter of ∼37.6 µm.

In addition to the static description above, we can derive an expression for the dynamic bubble growth. The following is a simplified model.

There exists a mechanical equilibrium (pressure) at the bubble boundary, and from the ideal gas law (Equation (2.19)) we have that

$$p_A + p_{pf} = \frac{2\gamma}{r} + p_{atm} + p_{blood}, \tag{2.25}$$

where

$$p_A + p_{pf} = (C_A + C_{pf})RT. \tag{2.26}$$

Here, r is the bubble radius, and C_A and C_{pf} the concentration of air and pf-MCP in vapour phase, respectively.

Using both Fick's first law of diffusion ($J = -D\nabla n$) and that a change in mass has to cause a flux through the boundary ($J = -\frac{\mathrm{d}n}{\mathrm{d}t}$), we have that

$$J_{pf} = -\frac{\mathrm{d}}{\mathrm{d}t}\left(\frac{4\pi C_{pf}r^3}{3}\right) = 4\pi r D_{pf}(c_{pf}(r) - c_{pf}(\infty)), \tag{2.27}$$

and a similar expression for J_A. Note that the diffusion flux J is given in moles per second, and that D is the diffusion coefficient. We can assume that the concentration of pf-MCP reduces to zero far from the bubble, i.e. $c_{pf}(\infty) = 0$. We get two differential equations,

$$-\frac{\mathrm{d}}{\mathrm{d}t}(C_{pf}r^3) = 3rD_{pf}L_{pf}C_{pf}, \quad \text{and} \tag{2.28}$$

$$-\frac{\mathrm{d}}{\mathrm{d}t}(C_A r^3) = 3rD_A L_A\left(C_A - \frac{p_{air}}{RT}\right). \tag{2.29}$$

Here L is the Concentration Ostwald coefficient describing the solubility of a gas, $L = \left(\frac{c}{C}\right)_{equilibrium}$ [37]. Lower-case c denotes the concentration in the liquid phase, while upper-case C is the concentration in the vapour phase. Under-saturation of air is incorporated in the term $\frac{p_{air}}{RT}$.

We rewrite these equations with dimensionless variables to get

$$F + A = \mu\rho^2 + (1+\vartheta)\rho^3, \tag{2.30}$$

$$\frac{dF}{d\Gamma} = -\frac{3L_{pf}}{\rho^2}F \quad \text{and} \tag{2.31}$$

$$\frac{dA}{d\Gamma} = -\frac{3\delta L_A}{\rho^2}(A - p_d\rho^3), \tag{2.32}$$

with the dimensionless variables

$$\mu = \frac{2\gamma}{p_{atm}r_0}, \qquad \vartheta = \frac{p_{blood}}{p_{atm}}, \qquad \kappa = \frac{r}{r_0}, \tag{2.33}$$

$$\chi_A = \frac{C_A RT}{p_{atm}}, \qquad \chi_{pf} = \frac{C_{pf}RT}{p_{atm}}, \qquad \Gamma = \frac{D_{pf}}{r_0^2}t, \tag{2.34}$$

$$A = \chi_A\kappa^3, \qquad F = \chi_{pf}\kappa^3, \qquad p_d = \frac{p_{air}}{p_{atm}}. \tag{2.35}$$

Here r_0 is the initial bubble radius, and t the time. Combining equations, we get a differential equation for κ,

$$\frac{d\kappa}{d\Gamma} = \frac{-3\delta L_A(A - p_d\kappa^3) - 3L_{pf}(\mu\kappa^2 + (1+\vartheta)\kappa^3 - A)}{\kappa^3(2\mu + 3(1+\vartheta)\kappa^2)}. \tag{2.36}$$

These three differential equations may be solved using appropriate initial conditions. Defining the variable X_{pf} to be the initial mole fraction of pf-MCP, we get the initial conditions

$$F(0) = X_{pf}(\mu + \vartheta + 1), \tag{2.37}$$

$$A(0) = (1 - X_{pf})(\mu + \vartheta + 1), \tag{2.38}$$

$$\kappa(0) = 1. \tag{2.39}$$

The growth of the bubble radius and volume is calculated from these differential equations (Figure 2.18), with parameter values given in Table 2.1 [33].

Table 2.1: Parameters used to calculate bubble diameter and volume of droplets with initial size 2 and 4 microns [33].

Parameter	Symbol	Value
Surface tension	γ	$0.04\,\mathrm{N\,m^{-1}}$
Droplet diameter	$2r$	$2\,\mu\mathrm{m}$ and $4\,\mu\mathrm{m}$
Atmospheric pressure	p_{atm}	$101\,\mathrm{kPa}$
Partial pressure of air	p_{air}	$92\,\mathrm{kPa}$
Systemic blood pressure	p_{blood}	$0\,\mathrm{kPa}$
Ostwald coefficient air	L_A	1.7×10^{-2}
Ostwald coefficient pf-MCP	L_{pf}	2.02×10^{-4}
Diffusion coefficient air	D_A	2.05×10^{-9}
Diffusion coefficient pf-MCP	D_{pf}	6.9×10^{-10}
Mole fraction of pf-MCP at $t = 0$	X_{pf}	1
Body temperature	T	$310\,\mathrm{K}$

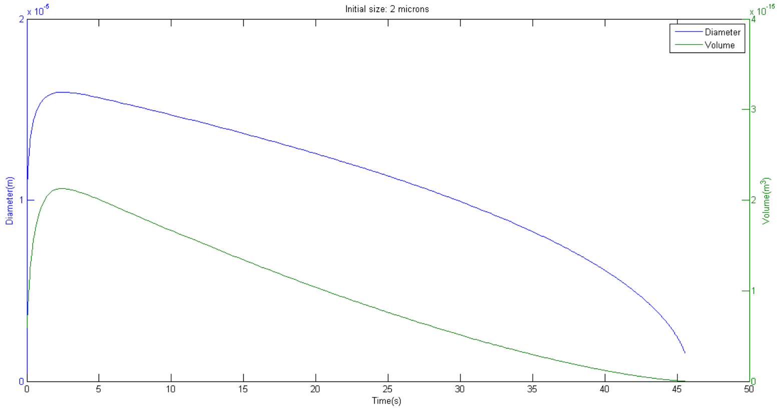

Figure 2.a:

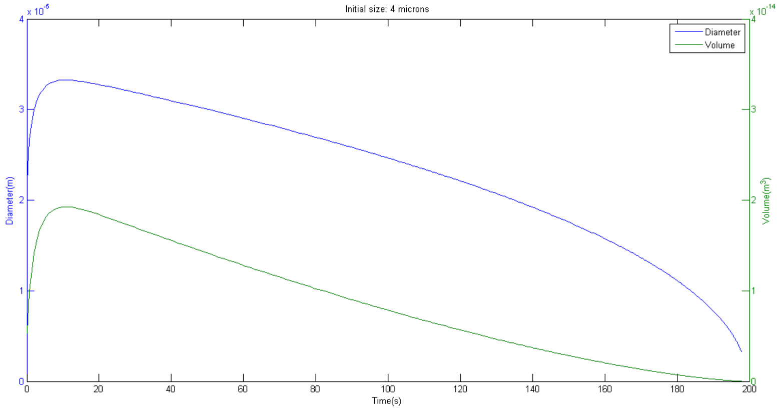

Figure 2.b:

Figure 2.18: Calculated growth of volume and diameter for an emulsion droplet using Equation (2.28), (2.30) and (2.36). The lifetime of the 2 micron droplet (a) is much shorter than the lifetime of the 4 micron droplet (b) [33].

2.1.12 *Resolution and depth of view*

This section follows the same references as Section 2.1.10, i.e the two books written by Flower [10] and Hoskins et al. [9]. The ultrasound waves used in medical imaging are emitted as short pulses, where the pulse length determines the longitudinal resolution. It is impossible to distinguish two points in the longitudinal direction separated by a distance shorter than half the pulse length. A short pulse is therefore desirable in order to produce good longitudinal resolution. The theoretical minimum pulse length is one wavelength, although this is difficult to achieve in practice. A few wavelengths is a more realistic minimum. The width of the signal frequency band increase with decreasing pulse length.

The required depth of view depends on how deep the tissue of interest is located, but there will always be a finite required depth penetration. Both the attenuation and the longitudinal resolution increase when the ultrasound frequency is increased. Hence, there will always be a trade-off between sufficient longitudinal resolution and the depth of view. The diagnostic frequency has to be adjusted according to the patient and application.

All ultrasound images used in this research are recorded at frequencies of 16 to 18 MHz with the Vevo 2100 (VisualSonics) ultrasound apparatus dedicated small animals. The longitudinal resolution is about $\sim$100 µm, significantly better than normal diagnostic tumor images. These imaging frequencies are above the fundamental resonance frequency for standard contrast agents. Scattering from blood and tissue increases with frequency (Equation (2.14)). The contrast-to-tissue ratio is therefore less.

Lateral resolution is the minimum distance perpendicular to the direction of propagation required to distinguish two objects. This is determined by the width of the beam, and may vary with the depth of view. It is common to focus the beam to obtain the best resolution at the depth of interest. Strong focusing will give very good resolution at a very limited depth range, while weak focusing give medium resolution through most of the image. Temporal resolution is determined by the frame rate, which is typically between 10 and 30 frames per second.

Both the phase-shift and the Sonazoid™ microbubbles used in this study are smaller than the image resolution. This limits the performance of a counting algorithm, as it is impossible to distinguish echoes from individual bubbles within an area smaller than the spatial resolution. It may increase the echo amplitude, but separate intensity peaks will not appear in the image.

2.1.13 *Speckle noise*

Speckle is random, deterministic noise, giving ultrasound images the characteristic, granular appearance. Speckle is present in all coherent imaging, and is caused by interference of echoes originating from scatterers within the same resolution cell. These echoes can not be distinguished by the transducer. The received signal is proportional to the sum of the waveforms, which is determined by their relative phase. The shape and size of the speckle pattern are determined by the dimensions of the imaging system and the structure of the imaged tissue [38].

Due to speckle, even smooth tissue look granular, and this reduce contrast resolution with an order of ~7 [34]. The contrast resolution is a measure of the level of contrast needed for an object to be visually identifiable within an image. The multiplicative nature of speckle, means that noise is proportional to the amplitude of the echo. This increases the difficulty of identifying single microbubbles, because similar intensity variations might be caused by the speckle pattern.

2.2 SOLID TUMOR AND ULTRASOUND

2.2.1 *Solid tumor structure*

A solid tumor is a mass of tissue with abnormal growth, made up of malignant and non-malignant cells, lymph and blood vessels, and the extracellular matrix. A tumor can usually be characterized as benign or malignant, where a benign tumor is localized with a well-defined boundary and do usually not pose any health threat. A malignant tumor is what we know as cancer, and can invade adjacent tissue, perform metastasis and be life threatening [39].

A cancer starts from one abnormal cell that proliferates through cell division resulting in uncontrolled growth. To maintain growth beyond a critical size of about 1 mm [39], new blood vessels are induced (angiogenesis) to meet the need of nutrients and oxygen.

The invasion of adjacent, normal tissue distinguish the malignant tumor from the benign, and this happens along the pathways of least resistance, i.e. along vessels or fascia. This invasion is enhanced by increased amount of proteases outside the tumor boundary. This increases the mobility of the cancerous cells. This also enhance the metastasis, where the cancer is spread along blood and lymphatic vessels and the peritoneal or pleural cavity to a new site [39].

An important feature that permits localized drug delivery is the structure of the cancer vasculature. This vasculature is developed through the angiogenesis, which is enhanced by vascular endothelial growth factors (VEGFs). The VEGFs are produced by the cancer cells, and are overexpressed in cancerous tissue. The VEGFs diffuse through the extracellular matrix (ECM) and connect to receptors on the inner surface of the vessel walls (Endothelial cells) [40]. These growth factors stimulates both the production of more endothelial cells, and the construction of new vessels through the extracellular matrix [41]. This results in a structure that differ from normal vasculature. The tumor vasculature has increased vessel density and vessel size, a large amount of dead-ends and a disordered branching pattern.

The abnormal amount of endothelial cells leads to vascular walls that lack in coverage of perivascular cells and tight adherens junctions, which usually stabilize the vessel. Hence, there will be large intercellular spaces in the vessel wall, and the vessels become leaky. This allow the cancer cells to enter the vasculature and enhance macromolecular transport through the vessel wall. Tumors also tend to have a reduced or impaired lymphatic system. This reduce the capability of draining extravasated fluid and macromolecules. This is called the *enhanced permeability and retention*(EPR) effect [42]. The EPR effect enhances local retention of cancer drugs.

2.2.2 *Tumor imaging*

Imaging of tumors is important in diagnosis and early detection of cancer as it allows for non-invasive differentiation of benign and malignant tissue. It is possible to use B-mode images to distinguish on behalf of shape and texture, but these properties varies between different types of cancer. For prostate cancer, about half of the tumors could be identified in a B-mode image due to reduced echotexture and a rectangular shape [43].

More advanced imaging such as Doppler or contrast enhanced imaging can image the tumor blood flow, and make it possible to distinguish benign and malignant tumor from the blood flow pattern. For thyroid cancer, benign tumors have a hilar flow pattern, while malignant tumors have a peripheral pattern with short branches [44]. Malignant tumors have also higher microvessel density.Previously, a clear correlation between microvessel density and metastasis has been shown [45]. Contrast agent microbubbles provide the possibility of visualizing microvessels with diameter less than the resolution of the imaging system. In Figure 2.19, prostate cancer is imaged using B-mode (A) and harmonic non-linear mode (B).

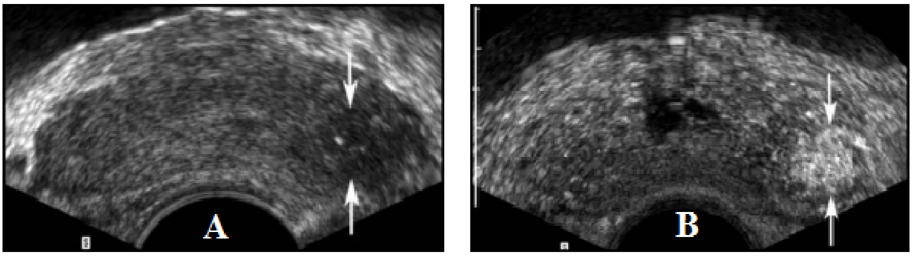

Figure 2.19: Image of malignant prostate cancer (arrows) [43]. A: The tumor is seen as a hypoechoic area in B-mode. B: Harmonic imaging of contrast agent enhance the visibility of the tumor.

The extracellular matrix found in tumors is unusually stiff, and the solid stress applied to the vasculature may squeeze blood vessels. This prevents drug delivery and can cause hypoxia within tumor regions. Hypoxia does not lead to cell death, but increases the production of proteins that prevents tumor-fighting immune cells [46]. By imaging the tumor vasculature using contrast agents, it is possible to visualize these oxygen-depleted areas. This might be useful predicting the outcome of cancer treatment.

2.2.3 *Cancer treatment*

Despite the massive amount of research, new drug development, genetic tumor characterization, improved radiotherapy and surgery, many young people die from cancer every year. Certain cancer types are strongly related to inherited predispositions, environmental factors, or lifestyle, such as smoking and exposure to sunlight. Prevention is therefore an important action in the battle against cancer. However, recent research by Tomasetti and Vogelstein [47] claims that most cancers (2/3) are due to "bad luck", i.e. caused by random mutations in normal, non-cancerous stem cells.

Screening is another action that involves examination of people without symptoms, and may reveal cancer in an early stage. Early detection is shown to be decisive for the effect of the cancer treatment and the outcome for the patient [39] [48]. In high-risk groups and in certain cancers, screening is applicable and useful, but the benefit of general mass screening is still debated.

The main available cancer treatments are surgery, radiotherapy and chemotherapy, and they are often combined to achieve the best result. Cancer treatment is not necessarily curative, but may be palliative; i.e. reduce symptoms and prolong lifetime. Regardless of method, a treatment is successful if all cancerous cell are corrupted. This should be accomplished with the least possible damage to healthy tissue. Recommended treatment depends upon type, location and the stage of the cancer. Surgery and radiotherapy are outside the scope of this thesis.

Chemotherapy includes both cytotoxic and cytostatic drugs to kill malignant cells or prevent further growth [49]. Chemotherapy is a systemic treatment as the drugs are distributed through the circulatory system. The benefit of systemic treatment is potential of targeting metastasis as well as the primary tumors. The drawback is that only a small fraction of the dose reaches the malignant cells. The rest of the dose causes dangerous side effects to healthy tissue [3]. These side effects limit the doses. This is described by a therapeutic index being close to one. The therapeutic index is the ratio of a lethal dose and the minimum dose required to achieve a therapeutic effect.

2.2.4 *Targeted drug delivery*

Increased targeting of the chemotherapeutic drugs enables the delivery of more drug to the malignant cells without an increase in the total dose. The increased leakiness of the tumor vasculature, the over-expression of specific receptors and impaired lymphatic system are three characteristic properties of tumor tissue that permits targeted delivery. Recent research has enabled drug carriers on nanoscale which utilize these possibilities [50]. The research in this field can be divided into passive, active and triggered targeting.

Passive targeting relies on the accumulation of drug in cancerous tissue due to the EPR effect. The drug is loaded into drug carriers that are only able to penetrate the endothelial layer if the EPR effect is present [51]. The carriers are designed to remain in the circulatory system for a long time to provide sufficient accumulation in the tumor. These carriers are of a size 10 to 500 nm, although the lower cut off size varies [52]. This targeting is limited by the vascularity and leakiness of the tumor. The increased hydrostatic pressure present in tumors can also reduce the accumulation [4].

Active targeting is conducted by drug carriers with a surface designed to stick to overexpressed receptors in the tumor vasculature or tissue. Triggered targeting utilize drug loaded particles that are activated inside the tumor to release the drug locally. Tumors may have different pH or enzymes than normal tissue, and these changes can trigger release. The drug release can also be activated by an external energy, such as heat, magnetic resonance, ultrasound or light [50]. Ultrasound mediated drug delivery is addressed below.

2.2.5 *Ultrasound mediated drug delivery*

Ultrasound is an attractive trigger for targeted drug delivery as it is non-invasive, generally safe and well characterized. It is proved that ultrasound increase the cell membrane permeability, in particular if microbubbles are present [7]. This is known as sonoporation and does mainly affect adjacent cells. Ultrasound can also increase the range of the drug after leaving the vasculature [53]. Note that ultrasound mediated drug delivery does not treat potential metastasis, but can be administrated simultaneously as normal chemotherapeutics to achieve a combined effect of systemic treatment and increased targeted delivery.

There are several mechanisms that can explain the increased drug transport, although their relative importance is unknown. One phenomenon is called micro-streaming and is caused by stable microbubble oscillation. This induces circulating eddies around the microbubble, which increases the fluid velocity and shear forces [54]. This may disrupt cell membranes [55]. A second mechanism is that the oscillations move the cell membrane and create hydrophilic pores (Figure 2.20) [7].

Ultrasound can also be utilized to collapse microbubbles. This can release drugs attached to the microbubbles surface, and the collapse can cause a shockwave capable of damaging surrounding tissue and increase drug transportation. If the microbubble is adjacent to a large cell membrane, this may induce an asymmetric collapse and a jet of fluid. This may rupture the cell membrane [56].

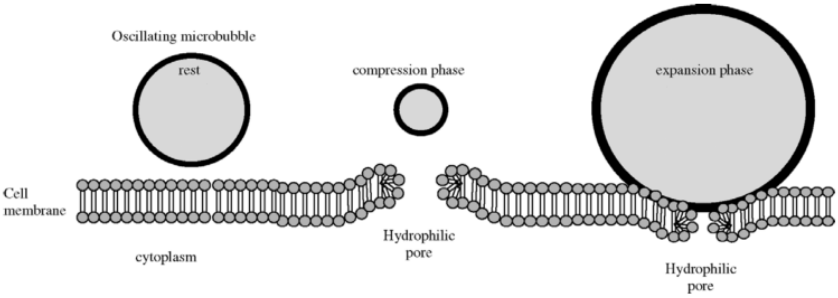

Figure 2.20: The oscillation moves the cell membrane and create hydrophilic pores that enables transport of fluid or macromulecules through the membrane [7].

The aforementioned mechanisms have been utilized *in vivo* to enhance drug delivery. Small amounts of hydrophilic drug can be attached to the surface of the microbubble, or hydrophobic drug can be incorporated into the shell of the microbubble. The drug is then released as the microbubbles are disrupted by an ultrasound pulse [57]. Drugs have also been loaded into liposomes and administered together with microbubbles, but the effect is then very dependent on the simultaneous localization of the liposome and microbubble in the tumor vasculature. To ensure the co-localization the microbubble and the drug can be encapsulated together within a liposome membrane shell [6].

The ACT™ phase-shift bubbles (Section 2.1.11) are different from other microbubbles used for ultrasound mediated drug delivery. The loading of the drug into, or onto, the shell severely limits the dose carried by each microbubble. The ACT™ phase-shift bubbles can carry ∼100 times this dose, because the drug is loaded into the volume of the emulsion droplet. The sonoporation effects mentioned above relies on cells being very close to the oscillating bubble. It follows from the phase-shift bubbles being stuck, that they guaranteed to be adjacent the vascular wall. The increased radius of the phase shift bubbles (∼10 times the radius of normal microbubbles) increase the amount of fluid moved by the oscillating bubble by an order of ∼1000. The resonance frequency of the phase-shift bubbles is on the other hand lower than normal microbubbles, causing slower oscillations. If we consider the produced shear forces, the theory predicts that the increased size and the decreased oscillation velocity equalizes each other. This support the assumption that the sonoporation mechanisms caused by normal microbubbles may also be initiated by the phase-shift bubbles [34].

The phase-shift bubbles are designed to be utilized in ultrasound mediated drug delivery. The amount of released drug will be proportional to the number of activated phase-shift bubbles. It is therefore important to measure the number of activated bubbles, and compare this to the observed treatment efficiency. The phase-shift bubbles can also be utilized to image the tumor vasculature.

2.3 EXISTING ALGORITHMS FOR IMAGE PROCESSING AND COUNTING

Identification and counting of stuck phase-shift bubbles is the core problem tackled in this work. The problem is divided in three main subjects. The first part is image registration, utilized to remove motion artefacts, which is of great importance for the robustness. It is difficult to identify stuck objects if their position in the image changes from frame to frame.

The second subject involves enhancing the contrast agent. Contrast agent provides positive contrast into the image. A simplified description is that the image is a sum of the background signal (i.e. signal from tissue without contrast agent present) and the signal provided by the contrast agent. To extract the contribution from the contrast agent, the obvious solution is to subtract the background. Another common solution is to apply a bubble specific imaging mode that suppress tissue and enhance microbubbles. This solution is more applicable to normal diagnostic imaging, where the tissue non-linear response is minimal. Frequencies from 16 to 18 MHz are applied in this research, and the tissue non-linear response is present. Sonazoid™ microbubbles can be imaged in non-linear contrast mode, but the tissue signal is visible (Figure 2.21). The response from Sonazoid™ microbubbles to 16 MHz is shown in Figure 2.22.

The phase-shift bubbles respond fundamentally different from the Sonazoid™ microbubbles, due too different size (Figure 2.23). Comparing the two simulations, we find that the non-linear response is much less for the ACT™ bubbles. The amplitude is ∼20 dB larger for the ACT™ bubbles. This makes them more suited for B-mode imaging, and background subtraction to segment the phase-shift bubble signal.

When imaging deposition and accumulation of ACT™ bubbles, the signal has two components - signal from free flowing (or possibly stuck) Sonazoid™ and deposited ACT™ bubbles. The problem is essentially to differentiate the stuck ACT™ from the free flowing Sonazoid™. This is accomplished by using the relatively greater signal in B-mode, and the stationary nature of the ACT™ bubbles. Image areas where phase-shift bubbles are present should have a consistency in image intensity. A consistency check can be applied using the fact that Sonazoid™ bubbles are destroyed by high power ultrasound, while ACT™ bubbles are not.

The last part of the image processing is identification and counting of the phase-shift bubbles. A few algorithms that handle quantification of stationary bubbles are published. In the work by Rychak et al. [58] the free bubbles were distinguished from the stuck bubbles by simply waiting for the circulating microbubbles to clear. The microbubbles are taken up in the liver or lungs, although this may take several minutes. The stuck microbubbles can then be segmented from the tissue signal by either using non-linear imaging, or by destroying the microbubbles with a high power ultrasound pulse. The signal left, can be subtracted from the prior signal to get the signal caused by microbubbles.

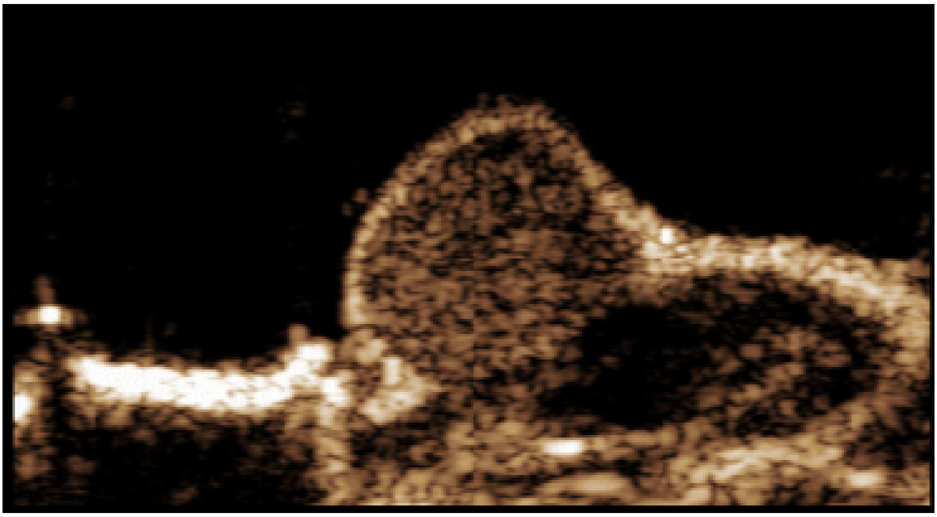

Figure 2.a:

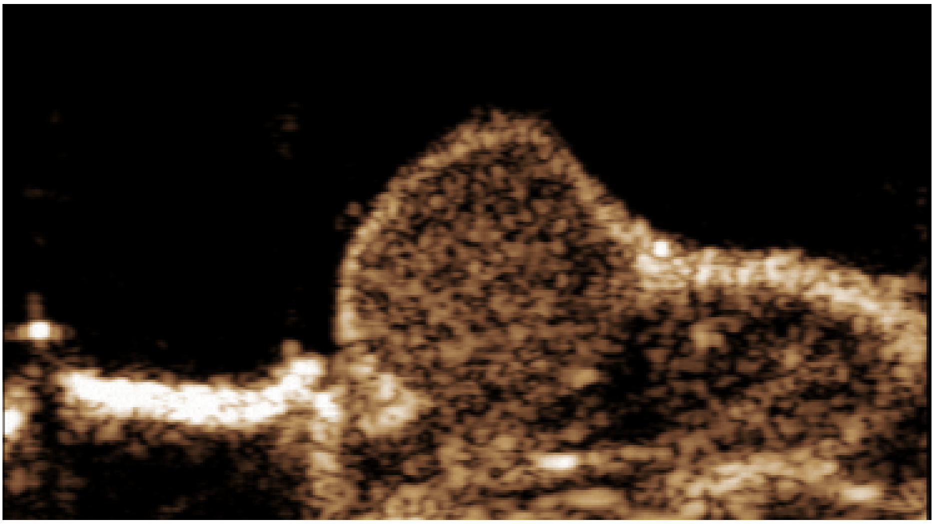

Figure 2.b:

Figure 2.21: Non-linear contrast mode image with Vevo 2100 of tumor tissue before (a) and after (b) introduction of Sonazoid™.

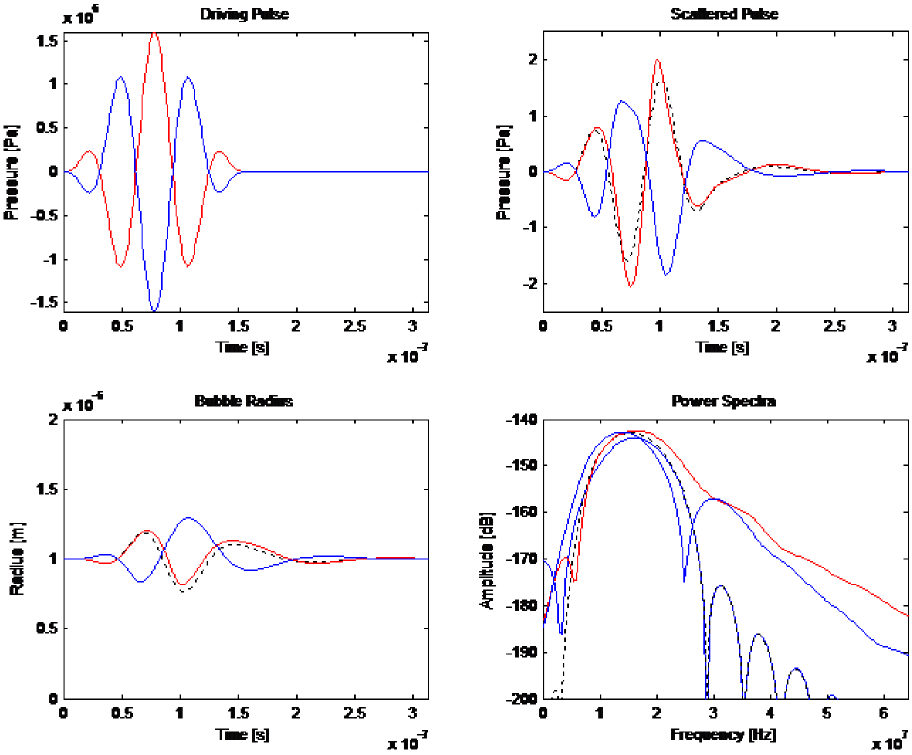

Figure 2.22: Simulation of 2 microns bubble with Sonazoid™ shell parameters response to two 2.5 wavelengths ultrasound pulse, 16 MHz, MI = 2.4. The two waves (blue and red) are 180° out of phase. The black stapled line illustrates the linear response. In the upper left image the transmitted waves are plotted, while the received waveforms are found in the upper right. In the lower left image the bubble radius is plotted. The lower right image shows the frequency spectra.

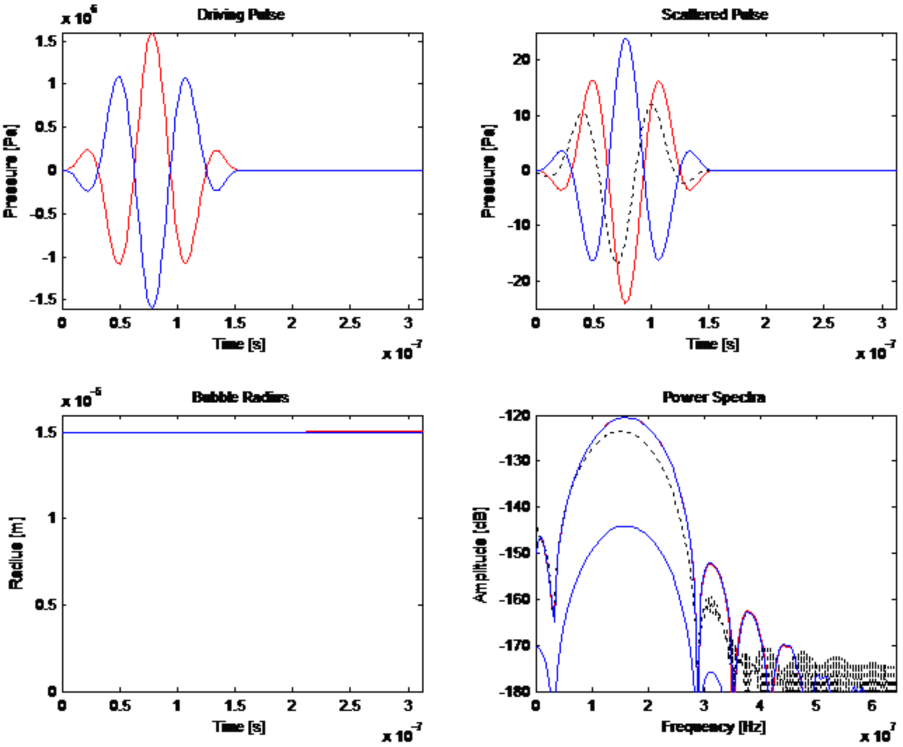

Figure 2.23: Simulation of 30 microns bubble with ACT™ parameters response to two 2.5 wavelengths ultrasound pulse, 16 MHz, MI = 2.4. The two waves (blue and red) are 180° out of phase. The black stapled line illustrates the linear response. In the upper left image the transmitted waves are plotted, while the received waveforms are found in the upper right. In the lower left image the bubble radius is plotted. The lower right image shows the frequency spectra.

Two other methods are described by Zhao et al. [59]. The first method utilizes a image-push-image sequence, where they first take one image before ultrasound radiation force is used to promote adhesion of the microbubbles. A second image is captured, and the first image is subtracted to segment the contrast agent. The second method utilizes harmonic imaging and a high-pass filter to differentiate tissue and contrast agent. For both methods the signal from free flowing microbubbles is removed by low-pass interframe filtering. A low-pass filtering is also applied by Needles et al. [8] to distinguish free and stuck microbubbles. Here, subharmonic imaging is used to segment microbubbles from the tissue. This method is successfully applied *in vitro*.

2.4 IMAGE PROCESSING

2.4.1 *Transducer*

Both this section, and the following (Section 2.4.2), follows the book written by Flower [10]. A transducer has the capability to transform applied electrical signals to pressure waves and vice versa. It is therefore responsible for both emitting ultrasound pulses and receiving echoes in an ultrasound apparatus. A good transducer performs this task with high conversion efficiency and without introduction of noise [10].

The key element of the transducer is the piezoelectric element, which is a shaped piece of either a piezoelectric ceramic (lead zirconate titanate, PZT) or plastic (polyvinylidine difluoride, PVDF) coated with silver electrodes on the front- and backside. A voltage across the electrodes corresponds to a proportional change of the thickness of the piezoelectric element.

The speed of sound, c, in a piezoelectric element is approximately $4000\,\mathrm{m\,s^{-1}}$. The fundamental resonance is at $\lambda/2$, so the thickness, T, is given by the choice of the frequency f, i.e.

$$T = \frac{\lambda}{2} = \frac{c}{2f} = \frac{2}{f(\mathrm{Mhz})}. \tag{2.40}$$

Hence, the frequency range of a transducer is limited to a band around the fundamental resonance, and is determined by the thickness of the piezoelectric element [10].

The front of the piezoelectric element is covered by a matching layer that increases the efficiency by reducing the difference in acoustic impedance between the element and the tissue. The back is covered by a backing medium that gives mechanical support and provides mechanical damping.

Modern transducers usually have an array of piezoelectric elements. The advantage is the possibility of beam steering, translation and focusing, and enables parallel processing that can reduce acquisition time, speckle and signal-to-noise ratio (SNR) [10].

2.4.2 *Digitalization, amplification and time-gain compensation*

After the echoes have reached the transducer a signal is produced by making an image with the brightness at each pixel determined by the strength of the echo from the corresponding distance and direction. The first step in the image processing is to convert from analogue to digital signal. The digital signal is less vulnerable to noise and distortion, and it enables further digital image processing. Then a linear amplifier applies the same amount of gain to the entire signal, to make the signal strong enough for further processing. Time-gain compensation is then applied to equalize echoes from similar interfaces, regardless of the depth of their origin. This is performed by increasing the gain with increasing depth of echo. The depth of the echo is identified by the arrival time at the transducer. The rate of attenuation of ultrasound with depth is determined by the frequency and tissue.

After amplification and time-gain compensation the dynamic range of the signal is about 60 dB. The dynamic range of a signal is defined as the ratio between the largest amplitude that can be recorded without causing distortion and the lowest amplitude that can be distinguished from noise. The dynamic range of a common screen is about 20 dB. The signal must therefore be compressed before it can be displayed. To compress the dynamic range from 60 to 20 dB, an amplifier with non-linear gain is applied. Low amplitudes are amplified more than high, and the dynamic range is therefore decreased. Compression allows weak echoes from scattering within tissue to be displayed together with strong echoes from tissue interfaces.

2.4.3 *Radiofrequency and In Quadrature data*

Radiofrequency (RF) is a term used in ultrasound to describe unprocessed data. In Quadrature (IQ) refers to a demodulation of the RF signal, utilized to reduce the amount of storage space without loss of information. IQ modulation converts the signal from the real to the imaginary space. The IQ signal is obtained using a IQ-demodulator to down-mix, low-pass filter and decimate the RF signal. The IQ signal can be computed through a Hilbert transform [60].

2.4.4 *Hilbert transform*

The Hilbert transform is a linear operator that acts on a signal $u(t)$ to derive an analytic signal. The Hilbert transform converts the signal from real to complex space by adding or subtracting 90 degrees. It is used to obtain an analytic signal, that has by definition only positive frequencies in the Fourier transform. The analytic signal $\tilde{x}(t)$ can be written as

$$\tilde{x}(t) = x(t) + x_h(t), \tag{2.41}$$

where $x(t)$ is the signal and $x_h(t)$ its Hilbert transform [61]. The Hilbert transform can be written as a convolution,

$$x_h(t) = \frac{1}{\pi} p.v. \int_{-\infty}^{\infty} \frac{x(\tau)}{t-\tau} \, \mathrm{d}\tau = x(t) * \frac{1}{\pi t}, \tag{2.42}$$

where p.v. is the Cauchy principle value of the integral required to accommodate for the divergence at $t = \tau$ [62]. The associated analytic signal may be defined for any signal for which a Fourier Transform exists. It follows that $x_h(t)$ is the output of a system with impulse response $h(t) = 1/\pi t$, with $H(\omega) = -i \, \mathrm{sgn}(\omega)$ and input function $x(t)$. The system changes the phase of the positive Fourier components by $-90°$, and negative Fourier components by $90°$ and is known as the quadrature filter.

2.4.5 *Downsampling*

The envelope is used to create the B-mode images, therefore further reduction in data size can be achieved by downsampling of the RF signal. The RF signal is downsampled by a decimation factor M, by only recording every Mth sample.

The RF signal is strictly bandlimited by the bandwidth of the transducer. The envelope is thus also a bandlimited signal, with a finite maximum frequency. According to the Nyquist-Shannon sampling theorem, this signal can be sampled without aliasing or loss of information by a sampling rate twice the maximum frequency. Hence, the decimation factor, M, is determined so that

$$\frac{Fs_{RF}}{M} > 2 f_{envelope}^{max}, \tag{2.43}$$

where Fs_{RF} is the sampling frequency of the RF signal, and $f^{max}_{envelope}$ is the maximum frequency of the envelope. A thorough explanation is given by Crochiere and Rabiner [63].

2.4.6 *Image registration*

This section follows the thorough review written by Maintz and Viergever [64]. Image registration is the process where one image is spatially aligned to a reference image. The image to be aligned is called the moving image, while the reference image is called the fixed image. Image registration is an important part of image processing and can both be used to remove motion artefacts and to fuse images of the same object, captured with different image modalities or from different directions.

Image registration is initially divided into extrinsic and intrinsic methods. Extrinsic methods are based on foreign objects placed into the scene before the image is captured. This has the advantage of simple, feature-based registration, but the preplacement and removal of these objects may not be trivial.

Intrinsic methods can be divided into feature and intensity based registration. Features can either be easily recognizable points identified by the user, or structures that can be extracted from the image by image segmentation. These methods are mostly used in rigid transformations, and have the advantage of being simple computations once the features are determined. One drawback is that the registration often is limited by the reliability of the segmentation or identification of the features. Although these methods are applicable to both multi- and monomodal registration, and to different body parts, in general their use has been limited to neuroimaging and orthopedic imaging [64].

Intensity based registration differs from the other methods by using the intensity pixel values directly to compare the fixed and moving image. To compare the images a suited similarity measure is used (Section 2.4.8). Using different similarity measures, this method is suitable for both multi- and monomodal registration. The image registration is then performed using an optimization scheme to find the spatial translation of the moving image that minimizes the chosen similarity measure. Choosing the right similarity measure and optimization scheme is essential to get a satisfying result.

2.4.7 *Image transformation*

Transformation of an image is the basis for image registration, and can be described as a mapping of a coordinate vector $\vec{x}$ from the space X to a new coordinate vector $\vec{y}$ in the space Y. The transformation is performed by a transformation matrix A, i.e. $\vec{y} = A\vec{x}$.

In 2D a rigid transformation can be written as

$$\begin{pmatrix} y_1 \\ y_2 \\ 1 \end{pmatrix} = \begin{pmatrix} R_{11} & R_{12} & T_1 \\ R_{21} & R_{22} & T_2 \\ 0 & 0 & 1 \end{pmatrix} \begin{pmatrix} x_1 \\ x_2 \\ 1 \end{pmatrix}, \tag{2.44}$$

where R_{ij} are elements in the rotation matrix

$$R = \begin{pmatrix} \cos\theta & -\sin\theta \\ \sin\theta & \cos\theta \end{pmatrix}. \tag{2.45}$$

The rotation matrix rotates the coordinates an angle θ around the origo. The matrix elements T_{ij} determines the translation of the coordinates. A general affine translation is described by the matrix

$$\begin{pmatrix} a_{11} & a_{12} & a_{13} \\ a_{21} & a_{22} & a_{23} \\ 0 & 0 & 1 \end{pmatrix} \tag{2.46}$$

This enables shear and scaling of the image.

If we apply a transformation matrix to an image, we get the new pixel coordinates of the transformed image, but these points will not be on the grid coordinates of the image. For that reason, an interpolation scheme is applied to the transformed image coordinates to get the new pixel values at the grid coordinates. A suitable interpolation scheme must be chosen to meet the needs of the given problem (Section 2.4.10).

Image transformation can be divided into linear and non-linear transformation. For a linear transformation the same transformation matrix is applied to the whole image, whereas this is not the case for a non-linear transformation. Linear transformation is computationally faster and simpler, and less affected by noise. On the other hand, non-linear transformations can correct for local deformations outside the reach of a linear transformation.

The difficult part of image registration is not to apply the transformation, but to obtain the right transformation matrix. The simplest case is the point or feature based method, where easily recognized features are localized in both the fixed and moving image. The is accomplished either by interaction from the user, or by using a feature detection algorithm. In the case of an affine transformation, six pair of corresponding coordinates are needed to solve the set of linear equations to obtain the six unknown elements in the transformation matrix. Usually, more points are obtained, and the transformation matrix is calculated using a least-squares approach.

2.4.8 *Similarity measures*

There are several ways of measuring the similarity between two images. Different approaches enhance different image properties, and are suit different problems. The choice of similarity measure will determine the minimum and the rate of convergence for the optimization scheme.

When the images to be compared are in the same modality, they are in the same intensity range. They only differ because of noise, geometric transformation and changes in the imaged object. Common similarity measures are the sum of squared differences (SSD), the sum of absolute differences or the cross correlation. If the changes in the imaged object is sufficiently small, and we assume the noise to be Gaussian, it is shown that SSD give the optimal result [65]. For two images A and B the SSD is given as

$$\mathrm{SSD} = \sum_{i}^{N} |A_i - B_i|^2, \forall i \in A \cap B, \tag{2.47}$$

where i is an image pixel. A closely related similarity measure is the Mean square error, $MSE = \mathrm{SSD}/N$.

In multimodal image registration, the images have neither similar intensities or even a linear relationship between the intensities. For this type of problems, mutual information is the most common similarity measure. Mutual information is a measure of the statistical dependence of the two images. The alignment is optimal if the moving image contains the maximal amount of information about the fixed image. A detailed review of mutual information in medical multimodal imaging is conducted by Maes et al. [66].

2.4.9 *Regular step gradient descent*

An optimization scheme determines the optimal alignment by optimizing the chosen similarity measure. The optimization scheme is usually chosen through an empirical approach, where computational demand, reliability and stability are important factors.

The gradient descent method is a first-order algorithm that finds the local minimum of a multivariable, differentiable function $F(x)$ [67]. From a given initial state x_k, the optimizer moves a distance γ in the direction opposite to the gradient, i.e.

$$x_{k+1} = x_k - \gamma \Delta F(x_k). \tag{2.48}$$

This method suffers from the reliability of the step distance γ. A step, too long or too short, result in slow, or no convergence. The *regular step gradient descent* is a variation where the step length is halved every time there is a significant change in the direction of the gradient. The optimization terminates after reaching a minimum, at a minimum step length, or after a maximum number of iterations.

To speed up the image registration, a pyramidal method can be applied together with the gradient descent. A smoothing filter is applied to the images, before they are decimated by a factor of two. This is performed for a given number of pyramid levels, resulting in a set of images with decreasing size. This scheme starts by optimizing the translation of the smallest image, and this optimal translation is used as an initially in the next pyramid level. In addition to increased speed, there is less chance of getting stuck in a local minimum due to the smoothing applied before each decimation.

2.4.10 *Interpolation*

Interpolation is a mathematical method for resampling of data points [63]. Several different methods are common, all with a trade-off between performance and computational effort. For image interpolation, nearest neighbour, bilinear and bicubic approaches are the most common methods. Nearest neighbour assign a value to the new data point equal the value of the nearest existing data point. The assigned value in bilinear interpolation is a linearly weighted sum of the nearest existing data points with respect to the distance to the new data point.

For bicubic interpolation, a piecewise, cubic polynomial is calculated from the existing data to estimate the value at the new data point. A smooth fit is achieved by requiring the function, and its 1. and 2. derivatives to be continuous at every boundary. This scheme is slower than nearest neighbour and bilinear, but the result is usually improved.

2.4.11 *Background subtraction*

Background subtraction is a method for visualizing the contrast agent in the ultrasound images. A background image is created from a set of images recorded before the presence of the contrast agent. The background is constructed by taking the maximum value of the chosen set at each pixel. The contrast agent can be segmented from the image by subtracting the background image.

To ensure sufficient subtraction, the background can be filtered before subtraction with a maximum filter. A maximum filter is a morphological, non-linear filter that considers the neighbourhood around the given pixel. The assigned value is equal to the maximum value of the neighbours, and the size of the neighbourhood is given by the size of the filter. In other words

$$B_{ij} = max(A_{kl}) \quad \forall A_{kl} \in N, \tag{2.49}$$

where N is the neighbourhood of A_{ij}, where A and B is the original and filtered image, respectively.

This filter is applied to achieve a more robust background. By applying this filter we create a background of increased intensities, that can compensate for some of the natural variations and noise in the tissue signal. The microbubbles add positive signal. By subtracting the filtered background we make a conservative estimate of the contrast signal.

3

MATERIALS AND METHODS

3.1 IMAGE RECORDING

All ultrasound images have been recorded by Annemieke van Wamel and Andrew Healey prior to this study. However, their imaging setup and procedure is provided in the following sections, and provides necessary information of the data.

3.1.1 *The ACT™ clusters*

The ACT™ clusters are composed of $8\,\mu l\,ml^{-1}$ ($1.2 \times 10^9\,ml^{-1}$) microbubbles (HEPS-Na stabilized perfluorobutane microbubbles [Sonazoid™]) and $3\,\mu L\,mL^{-1}$ microdroplets (pf-MCP). If we assume the droplets to have the same size as the microbubbles, we get a microdroplet concentration of $\sim 4.5 \times 10^8\,ml^{-1}$[1]. Two different doses were used:

1. Low dose: 50 µl of the mixture, diluted 1:4. Concentrations are $0.75\,\mu L\,mL^{-1}$ oil droplets and $2\,\mu L\,mL^{-1}$ microbubbles.
2. High dose: 50 µl of the mixture, neat. Concentrations are $3\,\mu L\,mL^{-1}$ oil droplets and $8\,\mu L\,mL^{-1}$ microbubbles.

The Sonazoid™ microbubbles are stored lyophilized, and reconstituted with sterile water to create a liquid solution. They are used both as a contrast agent, and as microbubbles together with microdroplets to compose the ACT™ clusters (Section 2.1.11).

---

[1] We were not able to get hold of the accurate microdroplet concentration, in bubbles per microlitre, by the time this thesis was submitted.

3.1.2 *Imaging setup*

All ultrasound images evaluated during this work are imaged with the Vevo™ 2100 imaging system from Visual Sonics [68]. Two different imaging modes have been used, linear and non-linear contrast mode. Linear contrast mode was used to emphasize the ACT™ bubbles, while non-linear mode enhances the contrast from the Sonazoid™ microbubbles. The imaging settings are presented in Table 3.1.

For activation of the ACT™ clusters a transducer was placed in a water bath a fixed distance from the tumor. This transducer was either a V-scan or a Vivid MS5. The settings used are given in Table 3.2. The important difference between these transducers is the applied MI. It is also worthwhile to mention the size difference. The V-scan transducer is a part of a small, hand held device, while the Vivid MS5 is requires a large, stationary machine.

The mice received anesthesia before injection of ACT™ or Sonazoid™. The mice were placed on a rat handling table, with the left leg (location of tumor) lifted horizontally and fixed. Ultrasound gel and a water-bath bag was put on top of the tumor. The imaging and activation transducers were fixed inside the water-bath-bag (Figure 3.1).

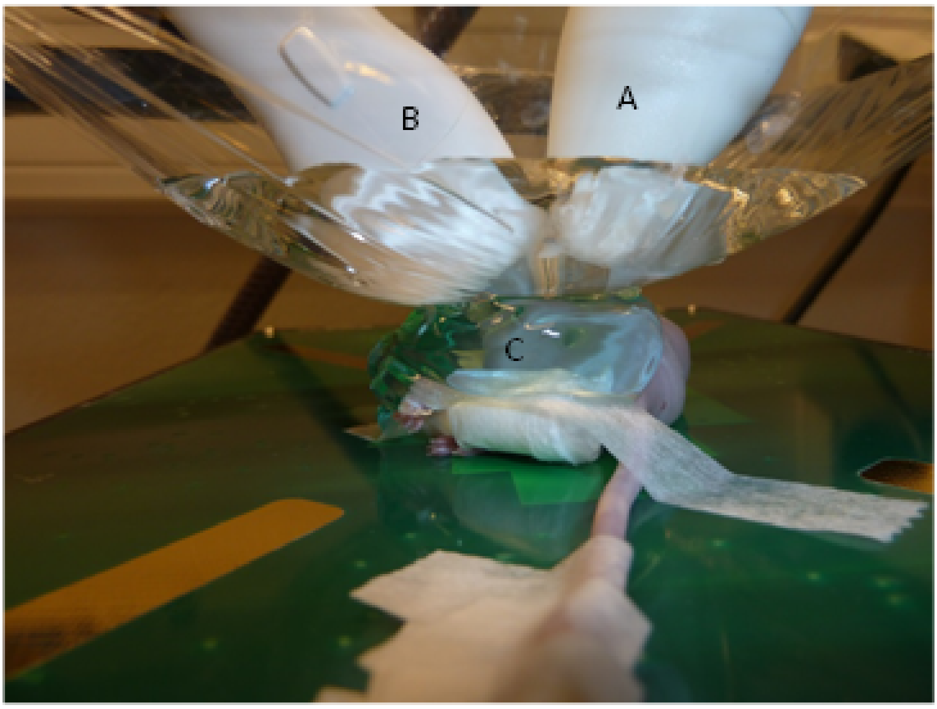

Figure 3.1: Experimental setup for activation and imaging. The Vevo MS250 transducer (A) and the V-scan transducer (B) is placed within the water-bath. The tumor side (C) of the mouse faces the camera.

Table 3.1: Settings used in the Vevo 2100 ultrasound apparatus.

	Value	
Parameter	Linear contrast mode	Non-linear contrast mode
Application	Cardiac	Cardiac
Preset	Contrast	Cardiac
Transmit:		
Frequency	16 MHz	18 MHz
Power	3%	10%
Gate		6
Beamwidth		Standard Acquisition:
Gain	10 dB	10 dB
2D Gain		10 dB
Frame rate	10 fps	10 fps
Depth	21.00 mm	21.00 mm
Width	23.04 mm	23.04 mm
Sensitivity		1
Line density	Standard	High
Persistence	None	Off
Display:		
Dynamic range	45 dB	40 dB
Display Map	MB1	MB2
Brightness	50	50
Contrast	50	50

Table 3.2: The settings used for the V-scan and the Vivid MS5 to activate the phase-shift bubbles.

	Value	
Parameter	V-scan	Vivid E9
Preset	Cardiac	
Frequency		2 MHz
Image distance	8 cm	2 cm
Focus depth	5 cm	1.5 cm
Frames per second		Maximum
Angle		45°
Mechanical index (MI)	0.5	0.28

3.1.3 *High ultrasound bursts*

In some of the ultrasound recordings, high power ultrasound were applied by the Vevo 2100 transducer. This was utilized because the high power ultrasound disrupts the Sonazoid™ microbubbles, while the large phase-shift bubbles are unaffected. This difference is utilized to distinguish the phase-shift bubbles from the Sonazid™microbubbles. The high power ultrasound were set to the maximum duration in linear contrast and non-linear mode. That is <0.1 s and 2 s, respectively [68].

3.1.4 *Experimental protocol*

Four different combinations of ACT™ dose and transducer were used in this study:

1. Animal 1 to 4. Vivid transducer and low dose.
2. Animal 5 to 8. V-scan transducer and low dose.
3. Animal 9 to 12. Vivid transducer and high dose.
4. Animal 13 to 16. V-scan transducer and high dose.

Sonazoid™ microbubbles were also injected alone as 1:4 dilution, 50 µl, for assessment of vascularity. All injections were administrated as bolus. The general protocol applied is given below [69]. A detailed list, including all exceptions, is found in Appendix D.

1. Imaging vasculature using Sonazoid™.
    a) Pre-injection images. Non-linear contrast mode.
    b) Sonazoid™ administration. Non-linear contrast mode.
    c) Post-administration images. In general 5 minutes after the injection. Non-linear contrast mode.
2. Imaging and activation of ACT™.
    a) Pre-injection images. Non-linear contrast mode.
    b) Pre-injection images. Linear contrast mode.
    c) ACT™ administration. Linear contrast mode.
    d) Post-administration images. Linear contrast mode.

   e) Post-administration images. Non-linear contrast mode.
   f) Post-administration images. Linear contrast mode.
   g) Two bursts of high power ultrasound. Non-linear contrast mode.
   h) Two bursts of high power ultrasound. Linear contrast mode.

3. Repeated imaging of vasculature using Sonazoid™.
   a) Pre-injection images. Non-linear contrast mode.
   b) Sonazoid™ administration. Non-linear contrast mode.
   c) Post-administration images. In general 5 minutes after the injection. Non-linear contrast mode.

3.1.5 *The animals*

Prostate adenocarcinoma cells (PC-3) were used in this research. The tumor cells were implanted in 16 female Balb/c mice at the age of 9-11 weeks. The tumor was implanted on the left hind limb, on the lateral side between the knee and the hip. The tumor cells were injected subcutaneously as a 100 µm suspension containing 3×10^6 PC-3 cells. The tumors were allowed to grow for 3 to 6 weeks until the diameter of the tumor was between 5 and 10 mm. The size distribution of the tumors (area) at the time of imaging is found in Figure 4.17.

3.2 IMAGE PROCESSING

Image processing is performed on the acquired RF-data to enable image registration, background subtraction and counting of ACT™ microbubbles. The envelope of the RF-data is obtained from the absolute value of the IQ-modulated data. The RF-data are IQ-modulated through a Hilbert transform. A logarithmic compression is performed to reduce the dynamic range before image registration. The images are resized from 13568×256 to 512×512 through decimation and bicubic interpolation.

3.2.1 *Image registration*

Motion correction is performed on all videos. All frames are aligned to a reference frame through an affine transformation. A regular step gradient descent optimization scheme has been utilized to determine the transformation matrix. The maximum number of iterations in the optimization scheme was set to 2000, using only one pyramid level. The reference frame was constructed from an average of the three first frames of the video used for background subtraction.

3.2.2 *Background subtraction*

Before background subtraction the data is linearized. For each processed video a background is computed from a set of frames. The set of frames is chosen individually to minimize motion artefacts through a heuristic approach. The background is filtered with a maximum filter of size 3×3. Then the background is subtracted from all frames to segment the signal caused by ACT™ or Sonazoid™ bubbles. Negative values after subtraction are set to zero.

3.2.3 *Counting*

A region-of-interest (ROI) is defined prior to counting. The ROI is drawn to include most of the tumor, while avoiding skin and other healthy tissue. Only phase-shift bubbles within the ROI are counted. The counting of stuck phase-shift bubbles is based upon a temporal coherence filter to distinguish between stuck and free-flowing bubbles. A correlation matrix is constructed from the 40 previous frames, to form the base for this temporal coherence filter. A correlation matrix d of two consecutive images, A and B, is defined as

$$d_{ij} = 1 - \frac{\left|(A_{ij} - B_{ij})\right|}{A_{ij} + B_{ij}} \quad \forall\, i, j. \tag{3.1}$$

A running average of the correlation matrix is performed, and pixel indexes where the running average exceeds a temporal coherence threshold, d_{min} are considered as stuck bubbles. The temporal coherence threshold is set to 0.85. This value is determined through a heuristic approach where the temporal coherence of manually identified bubbles is considered. A minimum intensity threshold is set to avoid counting of low-intensity noise. The minimum intensity threshold is set to 1000. It is important to emphasize that this algorithm counts the number of stuck phase-shift bubbles present, and not the total number of activated phase-shift bubbles.

3.3 COUNTING NUMBER OF PHASE-SHIFT BUBBLES IN TUMOR

For 16 animals, 125 data sets are processed in total, i.e. motion correction, background subtraction and automatic counting are performed. For each animal, one of the data sets images administration of ACT™ dilution. In these 16 videos, stuck phase-shift bubbles have been counted manually by Andrew Healey [69]. The manual counting is performed visually by careful identification of the phase-shift bubbles in the ultrasound videos. The results from manual and automatic counting are compared.

3.3.1 *Choosing representative number*

For each data set, the maximal counted number density is the representative value when the automatically and manually results are compared. The first 20 frames are excluded because they may be considerably affected by the previous data set (Figure 3.2). The reason for this is that the correlation matrix is continuously computed across consecutive data sets. The maximum value is chosen because it is closest to the total number of phase-shift bubbles activated throughout the video. This follows from the counting algorithm, which count the number of present phase-shift bubbles. The number of bubbles present has to be lower or equal to the total number of bubbles activated throughout the sequence.

3.4 QUALITATIVE VALIDATION

A qualitative validation of the counting algorithm was performed using the following approach. The counted video sequences were evaluated with the following prejudices. In video sequences with only Sonazoid™ bubbles, no phase-shift bubbles should be counted. After the administration of the ACT™ dilution, the phase-shift bubbles should stick and stay up to five minutes before decaying and disappearing. After the burst of high frequency ultrasound, all Sonazoid™ bubbles should be destroyed, but none of the phase-shift bubbles, i.e. the bubble count should not be affected by the high frequency ultrasound. The qualitative prejudices used to distinguish Sonazoid™ and phase-shift bubbles are stated in Table 3.3.

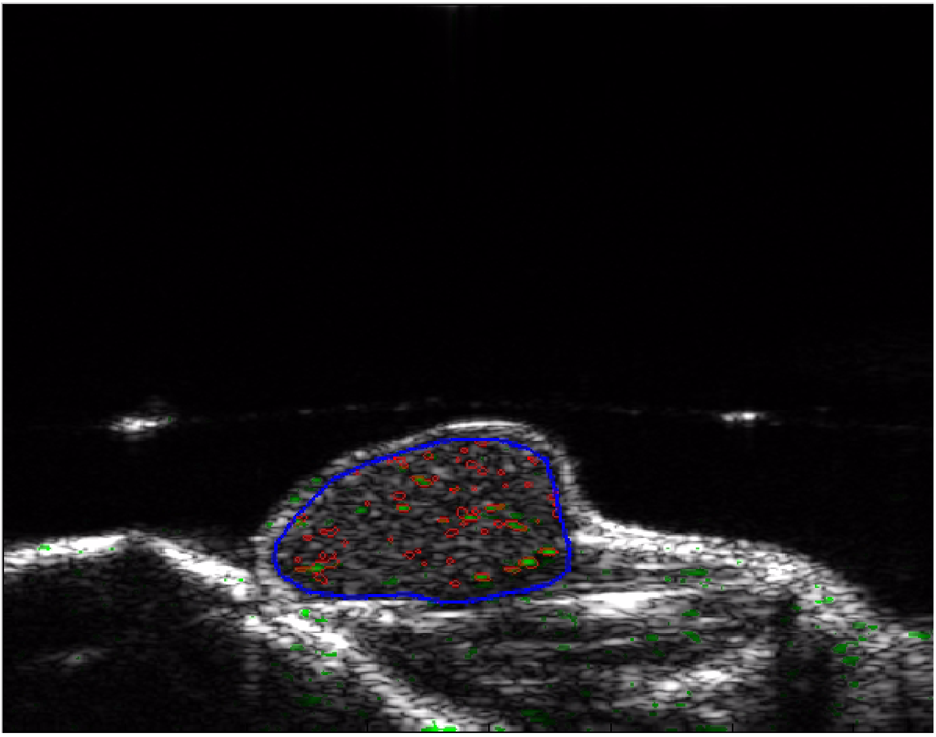

Figure 3.2: In the corresponding video we observe how the first 10-20 frames are affected by the correlation matrix from the previous video. The number of identified bubbles decreases quickly. The video is found at `E:\avi\2014-05-03-09-56-48_count_and_color_1_to_100dilate_1_intensity_1000ct_0.85running_avg.avi`

Table 3.3: Prejudices used to distinguish Sonazoid™ and phase-shift bubbles.

Property	Sonazoid™	Phase-shift bubbles
Non-linear imaging	Strong signal	Weak signal
Linear imaging	Weak signal	Strong signal
Kinetics	Free flowing	Stuck
High power ultrasound	Destroyed	Unchanged

3.5 QUANTITATIVE VALIDATION

3.5.1 *Synthesized data set*

A quantitative validation of the algorithm was carried out by counting a synthesized data set with a known number of activated phase-shift bubbles. Three different videos were used as background for the synthesized data set. It was important to use different backgrounds for the synthesized data set to evaluate the robustness and performance of the program. These background videos were recorded during intravenous injection of Sonazoid™, and were acquired using linear contrast mode. Different amount of free flowing Sonazoid™ is the main difference between the three data sets.

In each background, different numbers of artificial phase-shift bubbles were added, to create data sets with a known number density of phase-shift bubbles. The number density ranged from 0 to 15 bubbles/mm^2. For each background, 27 data sets with increasing number density were constructed.

The algorithm adding the synthesized phase-shift bubbles to a background is described in the following paragraph. First, N random positions within the ROI were drawn from a uniform distribution. Then N intensities were drawn from a Gamma distribution (see Section 3.5.2), and N frame numbers were drawn from a Poisson distribution to determine when the bubbles enter the tumor. Then, N bubbles were generated by applying the point spread function (PSF) to the drawn intensities. For each bubble, the maximum intensity follows the slope of the bubble growth, shown in Figure 3.3. These N bubbles are then log compressed and inserted into the video data.

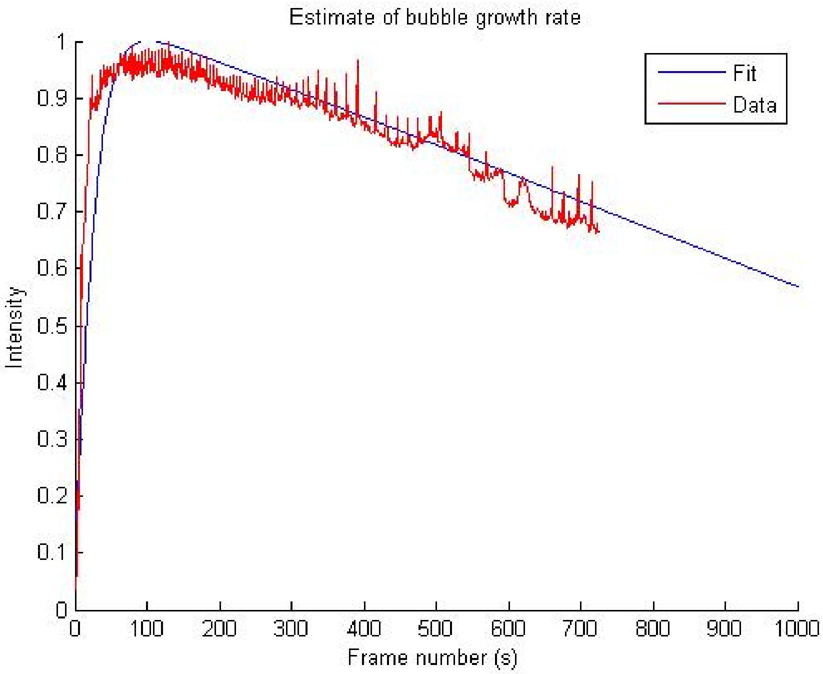

Figure 3.3: A growth slope is fit to data from an identified bubble in a true dataset.

3.5.2 *Phase-shift bubbles intensity distribution*

A heuristic approach was used to estimate the intensity distribution for the activated phase-shift bubbles. In a set containing 63 identified phase-shift bubbles, the maximum intensity was plotted for each frame (Figure 3.4). For each bubble the overall maximum value was used in a set, from which a gamma distribution was estimated (Figure 3.5).

The intensity distribution could probably been estimated through a more theoretical approach. However, the size distribution of activated emulsion droplets is not known accurately. The large phase-shift bubbles will also be deformed by the surroundings, and accurate backscattering and received signal from these bubbles are difficult to predict. A theoretical approach would therefore be based assumptions with unknown legitimacy. Therefore, the heuristic approach was considered to provide better results, and was chosen in favour.

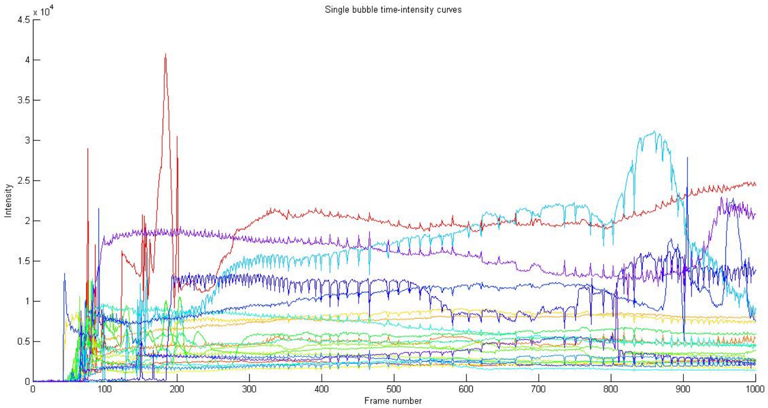

Figure 3.4: Time-intensity curves for a set of phase-shift bubbles.

3.5.3 *Measuring the point spread function*

The point spread function was measured from two different images. One image of a low solution of Sonazoid™ microbubbles in water, and another image of contamination in tap water. The size of the imaged microbubbles are smaller than the image system resolution. Thus, the bubbles visible in the image is effectively the PSF. A two dimensional, normalized Gaussian function was fit to a single, strong and easily identifiable bubble.

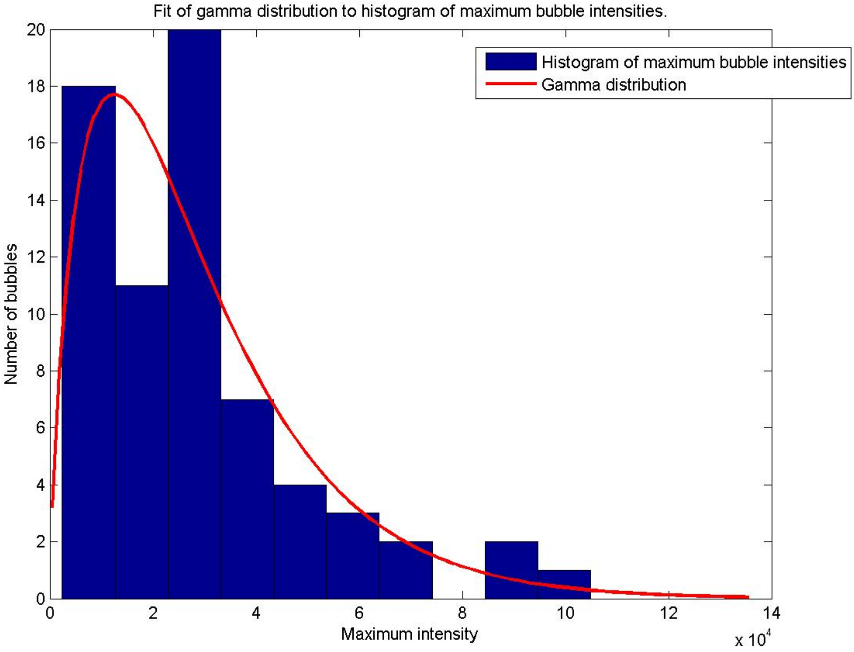

Figure 3.5: The fit of a Gamma distribution to the distribution of maximum phase-shift bubble intensities.

4

RESULTS

This chapter is divided in three parts. The first part deals with the qualitative results. This includes response to high power ultrasound, intensity growth curves, and phase-shift bubble behaviour. The second part provides a quantitative validation of the counting algorithm. This validation is based upon the randomly synthesized data set. The last part presents the results from the processing and counting of the real data set.

4.1 QUALITATIVE RESULTS

This section provides qualitative results, following the prejudices stated in Section 3.4.

4.1.1 *Effect of high power ultrasound*

The counted number of bubbles before and after two high ultrasound bursts in non-linear and linear imaging mode were available for 8 and 13 animals, respectively. Relative change after two bursts is shown in Figure 4.1 and 4.2. We consider 10% to be the threshold between a small and a large change. We observe that a large increase is the general (7 of 11) response in non-linear mode. The remaining four tumors show no, or little, response. In linear mode there is a larger spread. In two of the tumors, there is a large increase, while there is a large decrease in one tumor. The remaining five tumors experience no, or little, change. Note that 0% indicates no change.

Single bubble intensity curves, subject to two short bursts in linear imaging mode, are shown in Figure 4.3. The first and second pulse is marked by two arrows. We observe an increased intensity in three of the intensity curves at the first ultrasound burst. From the shape of the increased curves, we assume that these are activated phase-shift bubbles. At both bursts, we observe a small increase in several curves.

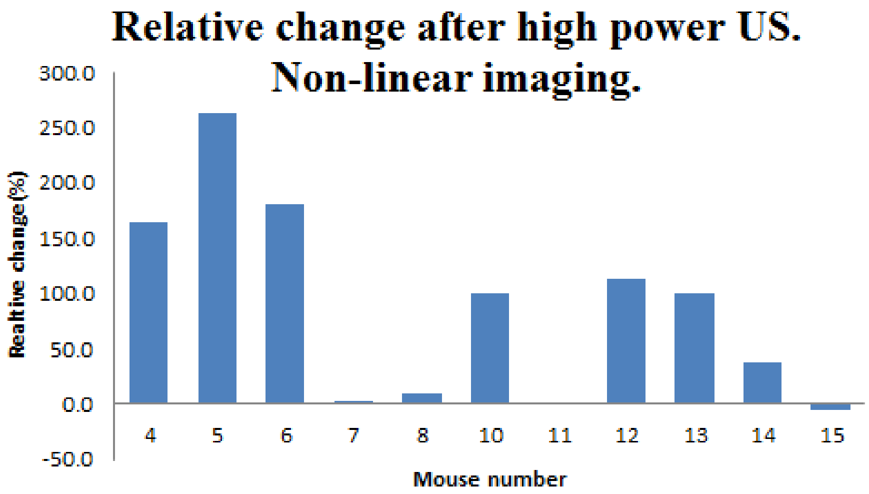

Figure 4.1: Relative change in the counted density before and after two high power ultrasound bursts in non-linear imaging mode. We observe that a large increase is the general (7 of 11) response in non-linear mode. The remaining four tumors show no, or little, response. Note that 0% indicates no change.

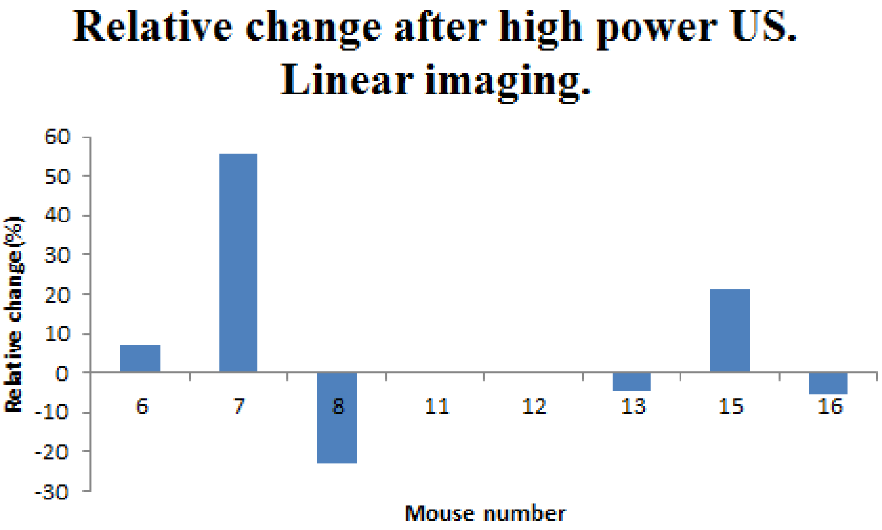

Figure 4.2: Relative change in counted density before and after two high power ultrasound bursts in linear imaging mode. In two of the tumors, there is a large increase, while there is a large decrease in one tumor. The remaining five tumors experience no, or little, change. Note that 0% indicates no change.

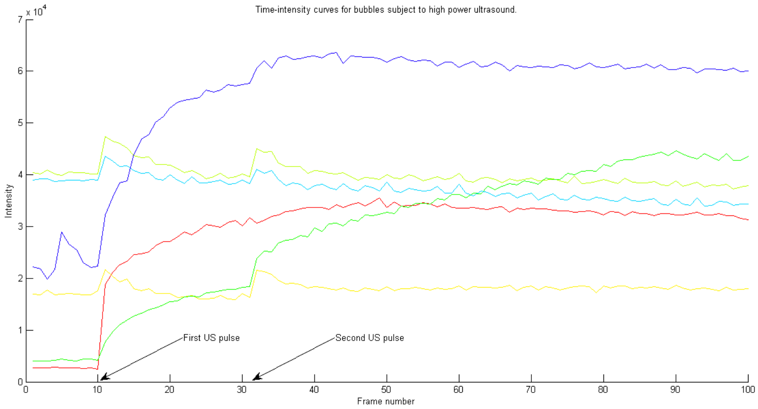

Figure 4.3: Time intensity curves for a few bubbles subject to a short high power ultrasound burs in linear imaging mode. The two bursts are marked by arrows. We observe an increased intensity in three of the intensity curves at the first ultrasound burst. From the shape of the increased curves, we assume that these are activated phase-shift bubbles. At both bursts, we observe a small increase in several curves.

4.1.2 *Phase-shift bubble kinetics*

Bubble kinetics are shown in Figure 4.4. A specific event occur in the location marked by the yellow circle 36 seconds into the corresponding video. A stuck phase-shift bubble is released from its current location and relocated at another position.

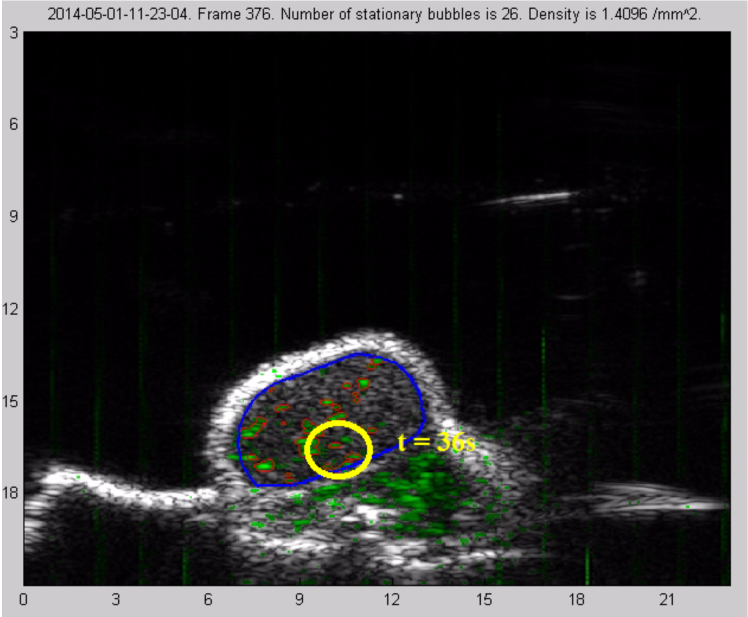

Figure 4.4: The corresponding video shows a stuck phase-shift bubble release from current location, travel a short distance and fasten in another location. The area is marked with yellow and the specific event occur at 36 seconds. Corresponding video is located at `E:\avi\2014-05-01-11-23-04_count_and_color_1_to_1000dilate_1_intensity_1000ct_0.85running_avg.avi`

The phase-shift bubble dynamics are also visible in Figure 4.5a and 4.5b, where we observe inflow and activation of a single phase-shift bubble. The increase in the intensity curve corresponds to the activation of the phase-shift bubble. We then observe how the bubble dissolves and decrease in intensity.

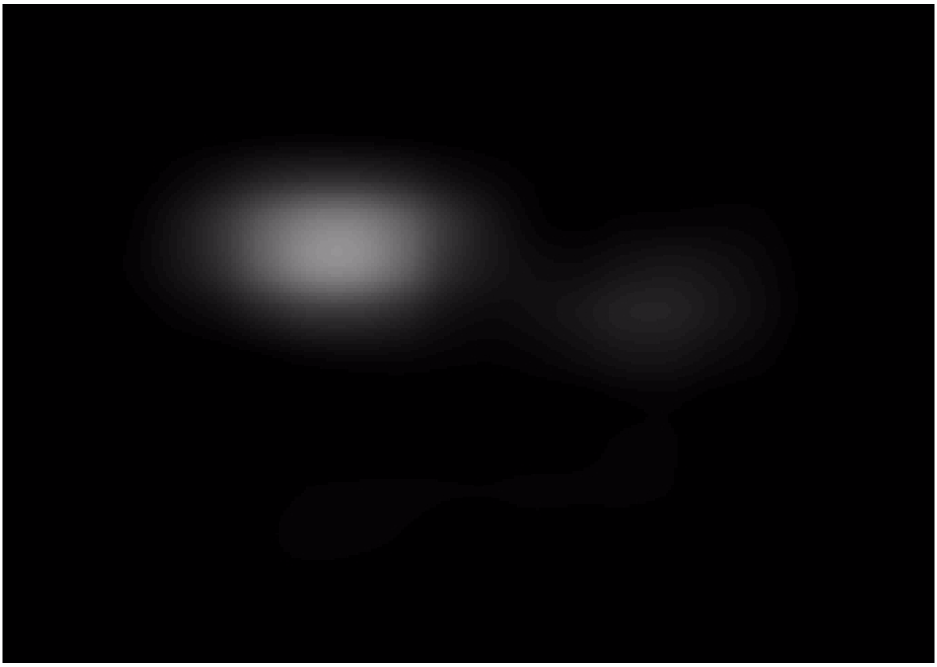

Figure 4.a: Inflow and activation of a single phase-shift bubble is visible in the corresponding movie `E:\avi \bubble _zoom_b4_10_28_44.avi`.

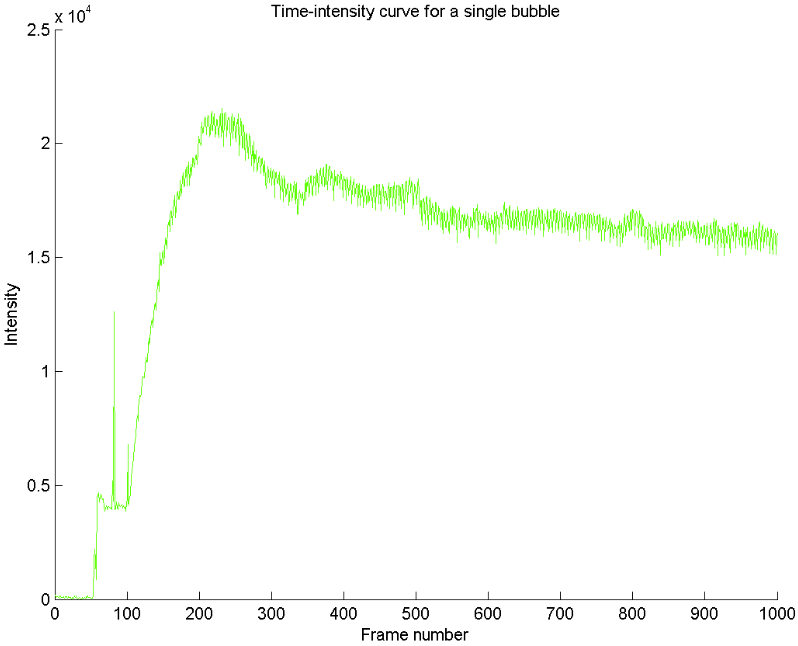

Figure 4.b: The corresponding time intensity curve for the phase-shift bubble observed in Figure 4.5a. The increase in intensity corresponds to the activation of the phase-shift bubble. We then observe how the bubble dissolves and decrease in intensity.

4.2 COUNTING OF SYNTHESIZED DATA

A total of 81 videos were synthesized and processed. The result is found for a low (7) and high (258) number of phase shift bubbles in Figure 4.5 and 4.6, respectively. We see that the program is counting too few bubbles (17) in the high number video (Figure 4.6) while the result is almost correct (5 of 7) in the low number video (4.5). The saturation in the high number video is seen as large clusters of phase-shift bubbles being counted as one bubble.

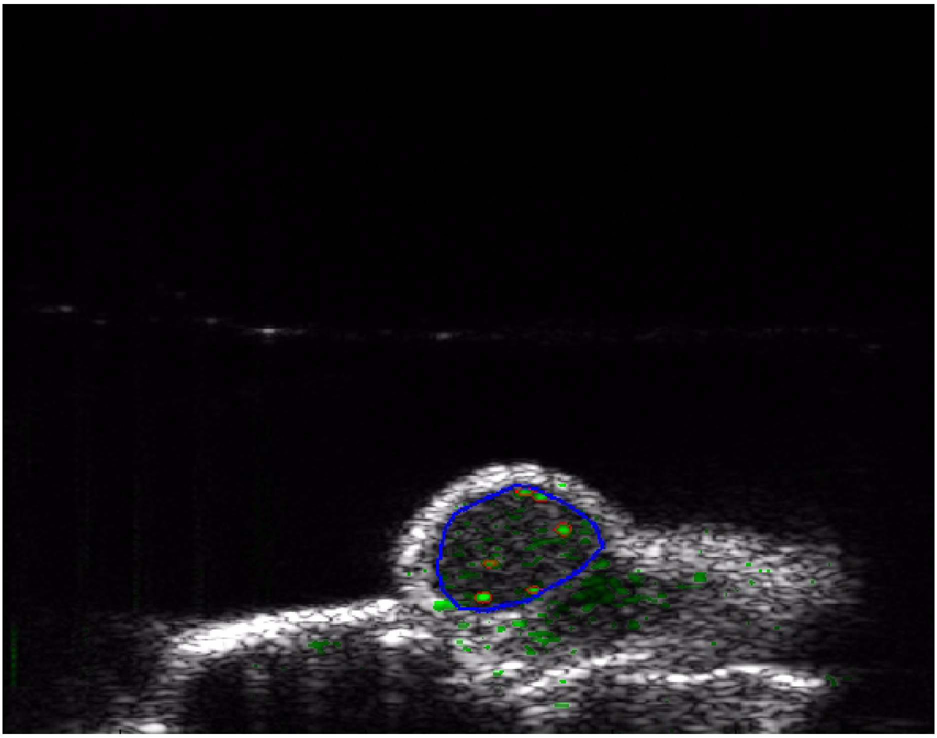

Figure 4.5: Counting of a synthesized data set The corresponding movie is found at `E:\avi\2014-05-02-09-51-16_PS_counted_7.avi`. The program counts almost the correct number of bubbles (5 of 7).

The synthesized data is based on three different background videos. The three data sets and the respective non-linear best fit are found in Figure 4.7. We find that the program is counting too few bubbles above $\sim 2\,\text{bubbles/mm}^2$, for all three backgrounds. We also observe a difference between the three

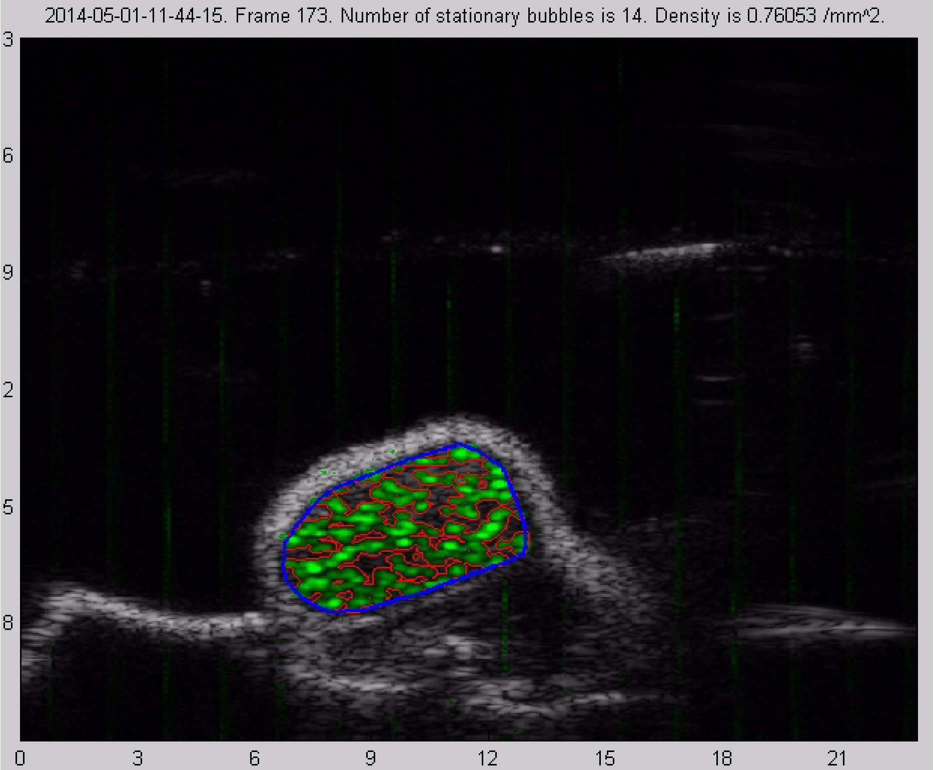

Figure 4.6: Saturation is clearly seen in as large clusters of bubbles recognized as one bubble, and we observe that the program counts too few bubbles (17 of 258). The corresponding movie is found at `E:\avi\2014-05-01-11-44-15_PS_counted_258.avi`.

backgrounds, especially for large number densities. The result from the second background is very different from the first and third background at high number densities.

The entire set, composed of all data from the three backgrounds, is presented in Figure 4.8 and 4.9. We observe the same saturation, and a increase in the width of the 95% confidence band above ∼2 bubbles/mm^2.

The data is log-transformed and fitted to a third degree polynomial. The curve fitting is performed on the log-transformed data because of the multiplicative nature of speckle noise. A logarithmic transformation converts multiplication to addition, and makes the noise almost normally distributed (Figure 4.10).

If the noise were perfectly normal distributed, all the data points would be situated on the linear (red) line. We observe some deviation for the smallest and largest values.

The spread of the counted number density has been evaluated (Figure 4.11). The average relative standard deviation is 0.016, and we observe it is roughly constant.

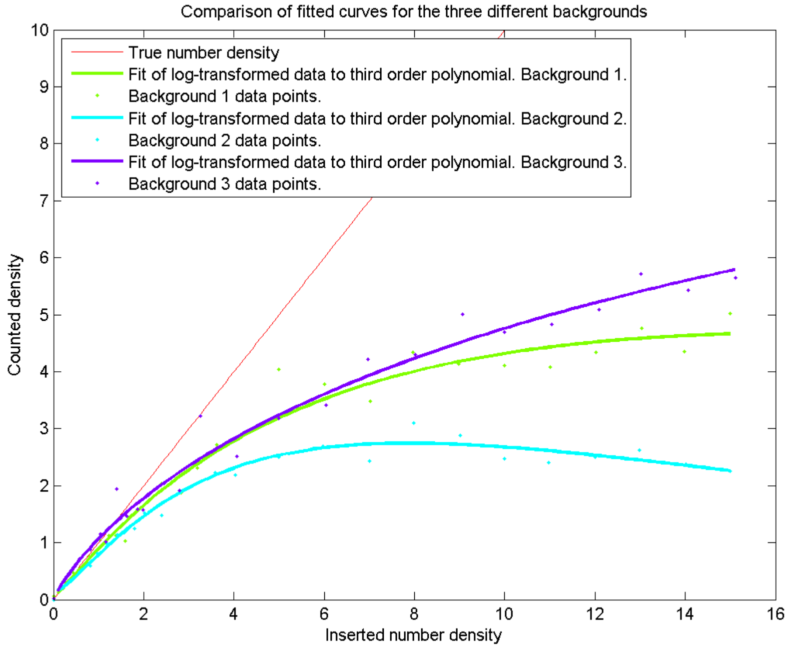

Figure 4.7: The three different data sets. The log-transformed data is fitted to a third degree polynomial. The corresponding background videos are found in the following directories. Background 1: `E:\avi\2014-05-01-10-00-05_PS_counted_0.avi`. Background 2: `E:\avi\2014-05-01-11-44-15_PS_counted_0.avi`. Background 3: `E:\avi\2014-05-02-09-51-16_PS_counted_0.avi`.

If we swap the axes, we can plot the real number density as a function of the counted number density. If we only consider the near-linear range, we can fit a linear curve to the log-transformed data (Figure 4.12). We then get a curve presenting the counted number of bubbles expected for a given real

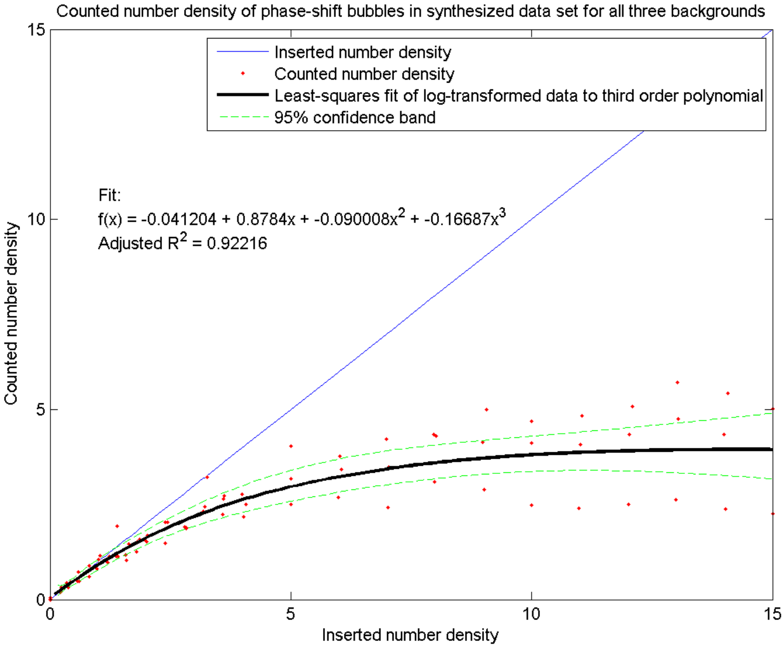

Figure 4.8: Plot and non-linear fit of the counted number density as a function of inserted density. We observe a saturation and an increased width of the 95% uncertainty band above ∼2 bubbles/mm². Note that the fit is performed on the log-transformed data. This make the residuals of the fit almost normally distributed (4.10).

number density. We observe how both the accuracy and precision decreases with increasing counted number density.

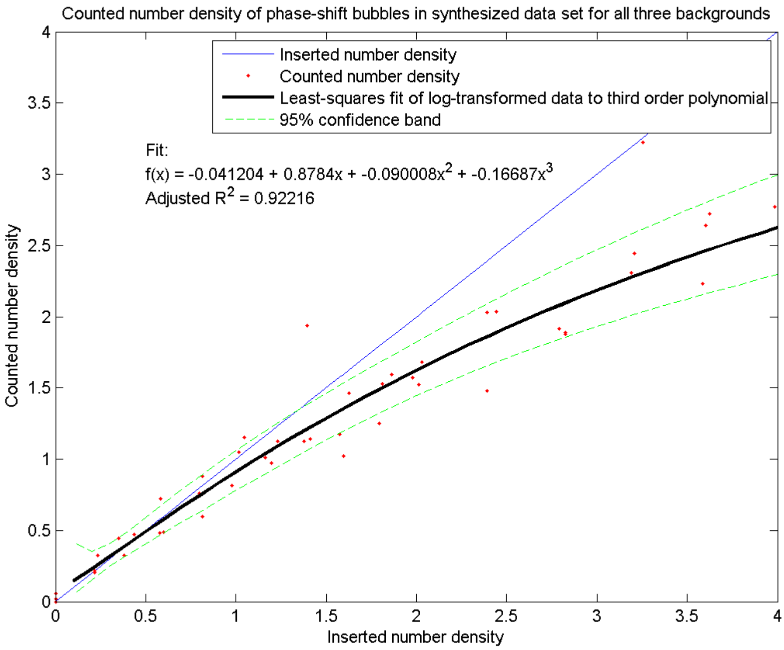

Figure 4.9: Plot and non-linear fit of the counted number density as a function of inserted density. Same plot as in Figure 4.8, but zoomed onto the range from 0 to 4 bubbles per square millimetre.

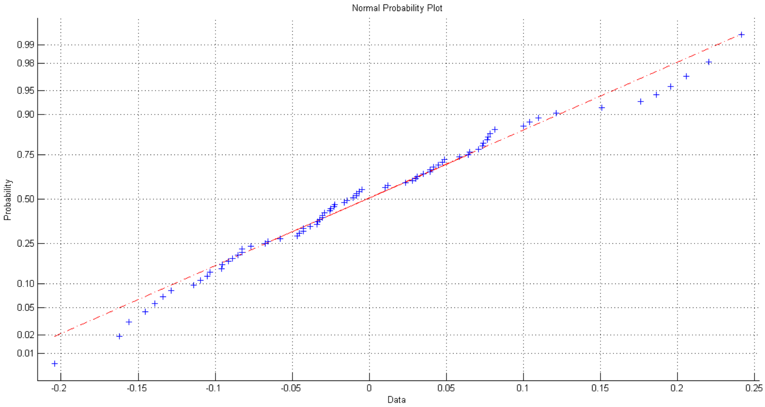

Figure 4.10: The Normal probability plot for the residuals of the counted data and the fit in Figure 4.8. We see that the residuals are almost normally distributed. Remember that the fit is performed on log-transformed data.

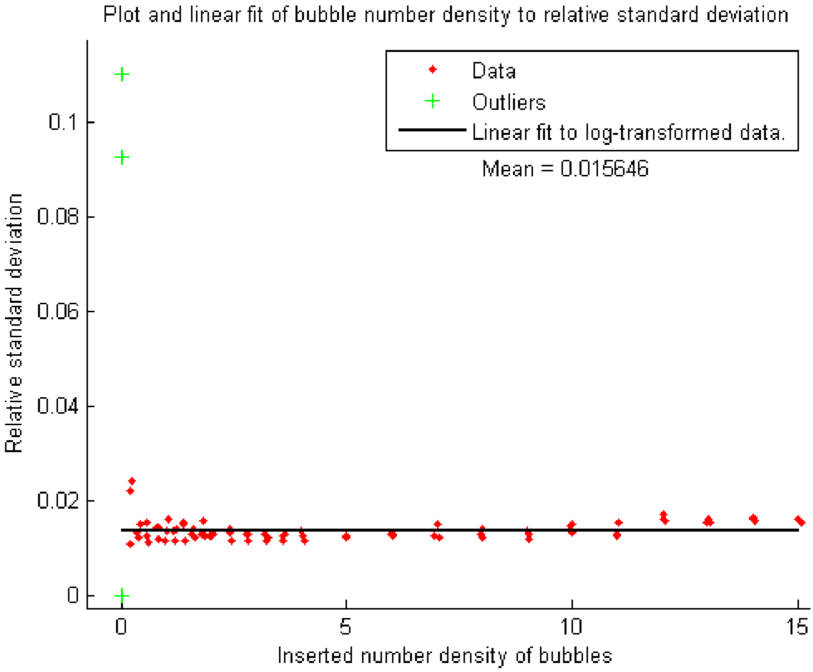

Figure 4.11: Relative standard deviation as a function of inserted number density of phase-shift bubbles. Linear fit to log-transformed data. The relative standard deviation is roughly constant. The mean relative standard deviation is 0.016.

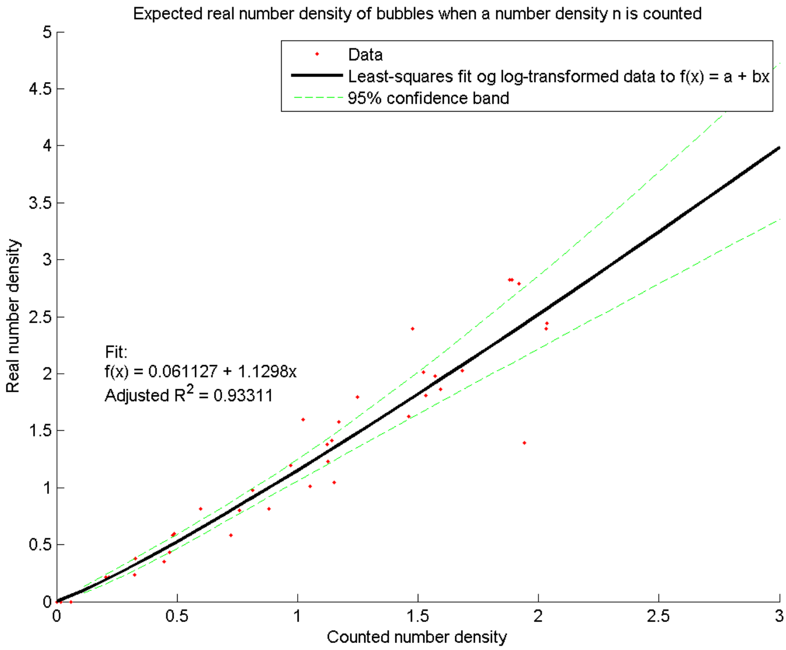

Figure 4.12: Plot and linear fit of real number density as a function of counted density. We observe how both the accuracy and precision decreases with increasing counted number density.

4.3 COUNTING OF PHASE-SHIFT BUBBLES IN TUMOR

An example of phase-shift bubble counting during ACT™ administration is shown in Figure 4.13. All contrast agent, both Sonazoid™, free-flowing ACT™ clusters, and stuck phase-shift bubbles, are coloured in green. The blue boundary defines the region of interest, and counting is performed only within this area. Areas identified as stuck phase-shift bubbles are circumscribed with red. To visualize the improved background subtraction and motion correction, a video is processed with both our program and the software developed by Visual Sonics (Figure 4.14). This is one of the recordings that is the most affected by motion. We observe a reduction in motion, and increased visualization of the contrast agent.

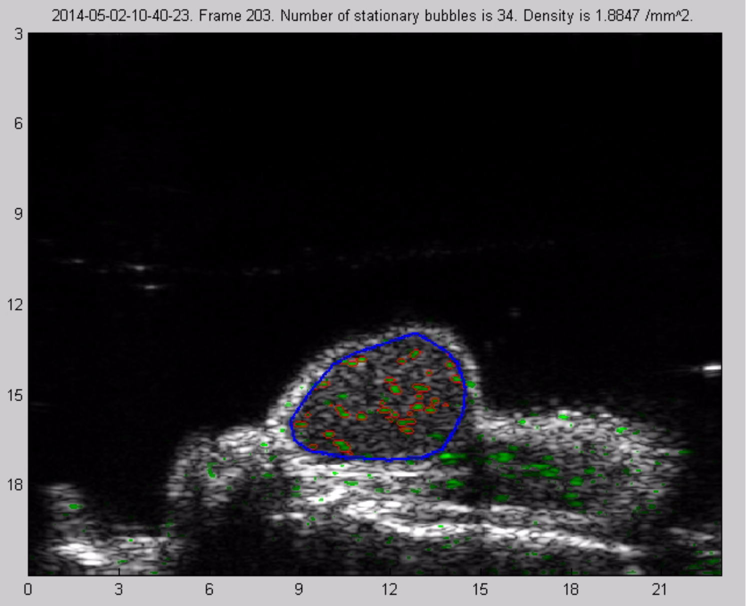

Figure 4.13: Counting during administration of ACT™. The corresponding video is found at `E:\avi\2014-05-02-10-40-23_count_and_color_1_to_1000dilate_1_intensity_1000ct_0.85running_avg.avi`. All contrast agent is coloured in green. The blue boundary defines the region of interest, and counting is only performed within this area. Areas identified as stuck phase-shift bubbles are circumscribed with red.

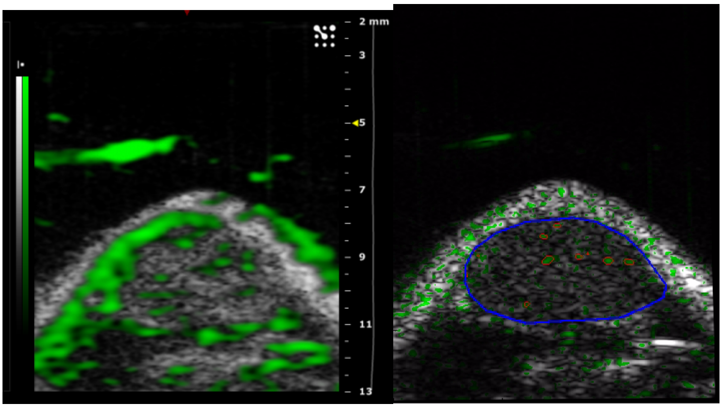

(a) (b)

Figure 4.14: The same video sequence processed with the Visual Sonics (a) and our program (b). The improved background subtraction increases the visibility of the individual bubbles, and there is a reduction in motion artefacts. The corresponding movies are found at `E:\avi\#01 2014-04-28-10-40-53.avi` and `E:\avi\2014-04-28-10-40-53_count_and_color_11_to_1000dilate_1_intensity_1000ct_0.85running_avg.avi`. Note that this is one of the recordings that is the most affected by motion.

Counted number density for the 16 animals are presented together with the manually counted results (Figure 4.15 and 4.16). We observe high correlation between the manually and automatically counted results. There may be small differences between the ROI used for the automatic and manually counted data. This affects the number of counted bubbles, but not the number density. The bubble count representing each animal is the maximum count during the video of ACT™ injection. Results for all 125 video sequences are found in Appendix (D).

Note the four different treatment groups (Section 3.1.4) displayed in Figure 4.15 and 4.16. We observe large variations within each group, and no obvious difference between each of the groups. However, from a two-way ANOVA analysis we find that there is a significant difference between the two doses given ($p = 0.023$), but no significant difference between the two transducers ($p = 0.146$). The average and standard deviation of the four different treatment groups (Section 3.1.4) is presented in Figure 4.18. The large spread within the treatment groups is observed as large standard deviations.

The relationship between size (area) and number of stuck phase-shift bubbles is found in Figure 4.17. Although the largest tumor holds the most phase-shift bubbles, there is no visible correlation between the tumor area and the number of phase-shift bubbles. The threshold for accurate counting is $\sim$2 bubbles/mm^2. From the distribution of the counted number densities in the 16 tumors (Figure 4.19), we find that the counted number density of phase-shift bubbles exceeds this threshold in only $\sim$14 % of the tumors.

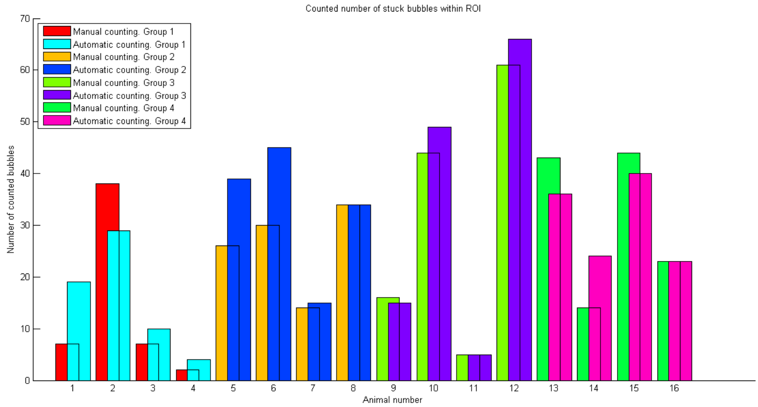

Figure 4.15: The number of counted bubbles in the 16 tumors. We observe large variations within the four treatment groups, but a high correlation between the automatically and manually obtained results. Note that there may be differences in the ROI used for the manual and automatic counting.

For all 16 animals, time-intensity curves showing the integrated intensity within the ROI as a function of time is plotted. The count number density is also plotted with respect to time. For one animal, this is presented in Figure 4.20 and 4.21. Similar results for all animals are found in Appendix C and B. We observe that the number density and intensity have only decreased about 50% during the five minutes. The high peaks observed after 200 seconds are caused by high power ultrasound bursts. Note that the red and black data points represent non-linear and linear data, respectively. In Figure 4.20 we see that the contrast intensity is lower in non-linear imaging mode.

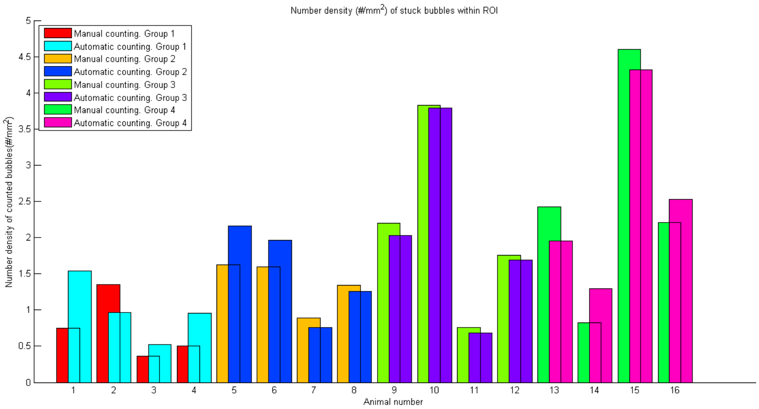

Figure 4.16: Number density of counted, stuck phase-shift bubbles in the 16 tumors. We observe large variations within the four treatment groups, but a high correlation between the automatically and manually obtained results.

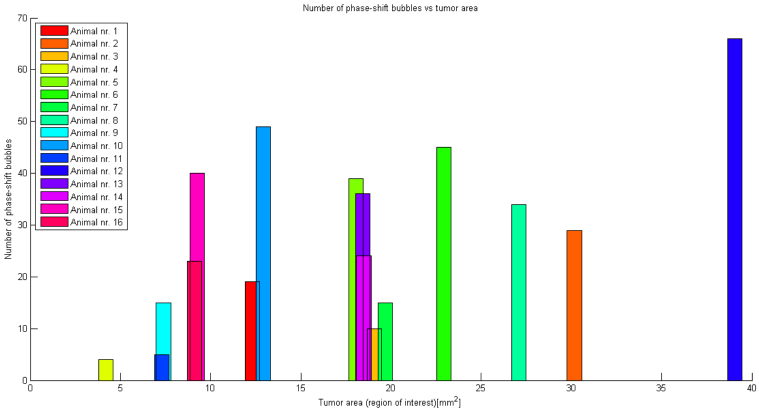

Figure 4.17: Plot of number of counted phase-shift bubbles versus total tumor area. The tumor area is the area inside the defined region of interest. There is no visible relationship between the tumor size and the counted number of bubbles.

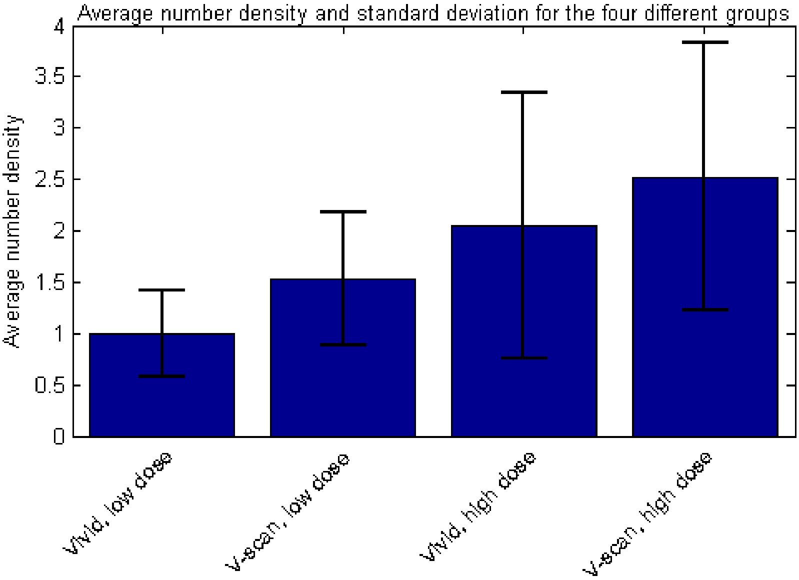

Figure 4.18: Average and standard deviation of number of counted phase-shift bubbles for the four different combinations of dose and transducer. We observe large standard deviations.

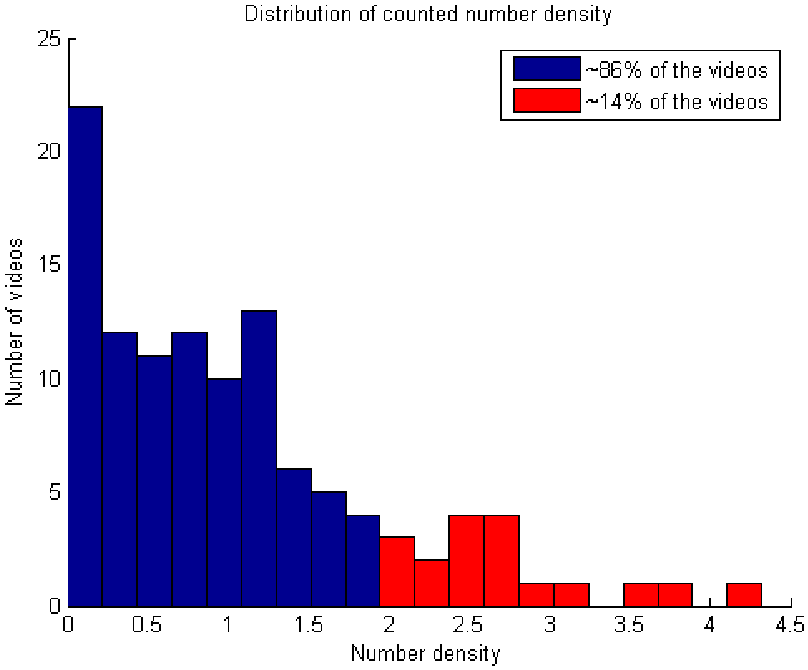

Figure 4.19: The number density distribution of phase-shift bubbles in the real data set. We observe that $\sim 86\%$ of the counted densities is below $2\,\text{bubbles/mm}^2$.

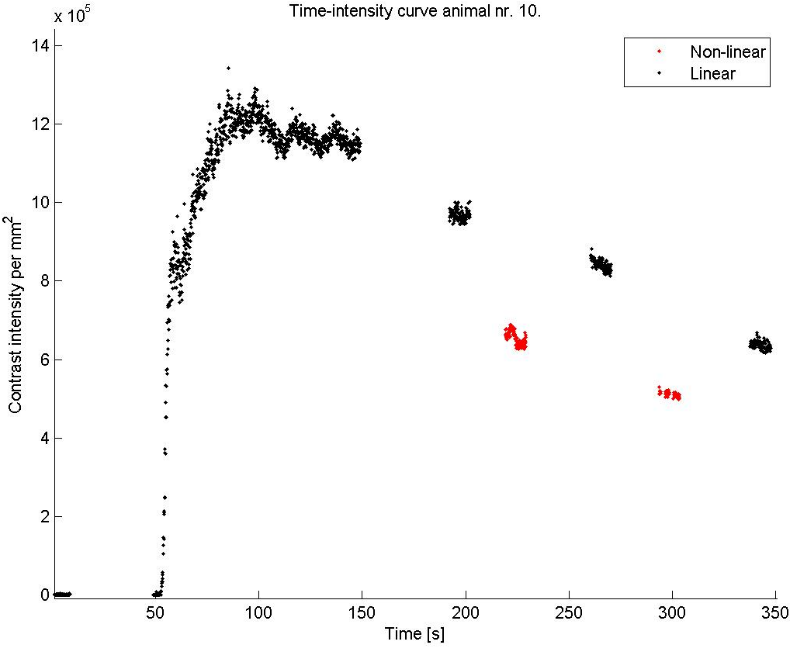

Figure 4.20: Time-intensity curve in animal nr. 10. We observe that the intensity has only decreased about 50% during the five minutes. These numbers represent both non-linear (red) and linear (black) contrast imaging.

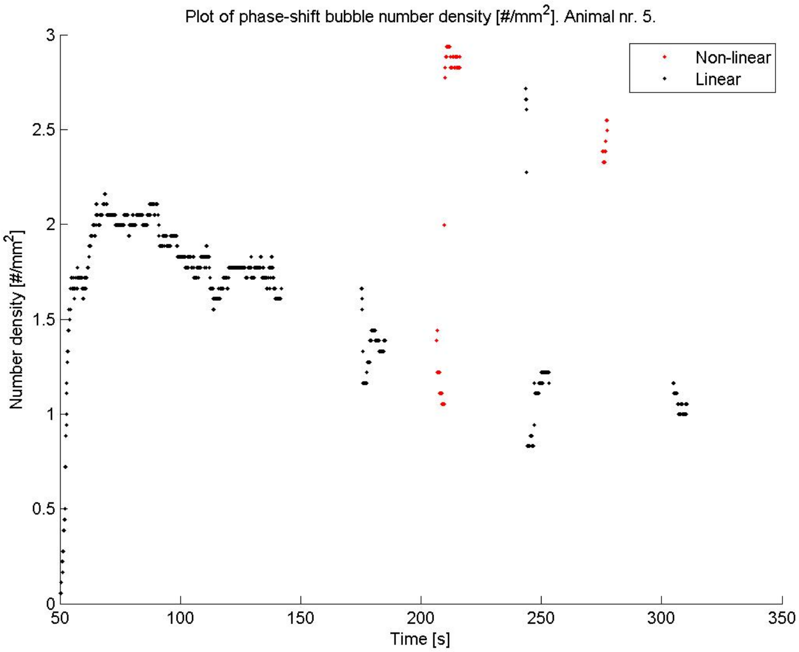

Figure 4.21: Number density as a function of time in animal nr. 5. We observe that the number density has only decreased about 50% during the five minutes. The high peaks are caused by high power ultrasound. These numbers represent both non-linear (red) and linear (black) contrast imaging.

5

DISCUSSION

5.1 QUALITATIVE VALIDATION

In Section 3.4, several results support the claim that the counted bubbles are phase-shift bubbles. In Figure 4.4 and the corresponding video, the phase-shift bubble dynamics are visible. A phase-shift bubble being stuck, releases, and attaches to another location. The adhesion and activation is also clearly visible in Figure 4.5a. The activation and dynamics imply that the identified bubble is a phase-shift bubble. The number density curves as a function of time (Figure 4.21) display how the phase-shift bubbles stay for several minutes. This may increase the drug retention time by complete, or partial, blocking of the tumor vasculature.

5.1.1 *Effect of high power ultrasound*

For most of the videos, the high power ultrasound had an effect on the counted number of bubbles (Figure 4.1 and 4.2). One tumor had a large decrease (more than 10% decrease) in counted number bubbles, while a large increase (more than 10% increase) where observed in nine tumors. Small, or no change were observed in the rest of the videos. This implies that most of the identified bubbles are not Sonazoid™. If the counted bubbles were Sonazoid™, we would have expected to see a large decrease in the counted number of bubbles. As mentioned earlier (Section 3.1.3), they are disrupted by high power ultrasound.

In linear imaging mode (Figure 4.2) there is a large spread in the relative change. Some bubbles are obviously activated (4.3). The decrease observed in three of the data sets may come from destroyed Sonazoid™, which may have been stuck in vascular dead ends or inflammation areas [34]. A large increase is observed in two thirds of the non-linear videos (Figure 4.1). The increase observed in both linear and non-linear imaging mode is not fully understood, but there are some possibilities.

We believe that the large increase comes from activated phase-shift bubbles. However, a high intensity burst directly after administration does not activate any phase-shift bubbles ([70], data not shown). We know that the Sonazoid™ microbubbles, circulating freely in blood, dissolve and decrease with time. It is therefore reasonable to believe that this also happen to microbubbles attached to the oil microdroplets. Smaller bubbles respond better to high frequency ultrasound. Thus, the reduced size explains why the longer circulating ACT™ clusters are activated by high power ultrasound, while the recently injected are not. Also, clusters might get stuck in dead-ends in the tumor vasculature or trapped by already activated phase-shift bubbles, and therefore accumulate in tumor over time. The high power bursts might be able to activate these phase-shift bubbles or move them into image plane. The radiation force may also be able to push phase-shift bubbles out of the image plane, causing the reduction in the number of bubbles observed in a few of the videos. The difference between the results in linear and non-linear mode may come from the difference in the high power ultrasound duration. The longer duration applied in non-linear mode allow more circulating, 'old' phase-shift clusters to be activated.

5.2 THE SYNTHESIZED DATA SET FOR VALIDATION

As there exist no 'Gold standard' for counting of phase-shift bubbles, a synthesized data set was needed to get a quantitative evaluation of the performance of the counting algorithm. By knowing the number of synthesized phase-shift bubbles we could determine the accuracy and precision for different number densities.

The synthesized data set was constructed to imitate an administration of ACT™ and Sonazoid™ microbubbles. To replicate the inflow, time of appearance, maximum intensity and position were chosen randomly from distributions generated from real data. In the real data some phase-shift bubbles get stuck after activation, or are released from the their location before the size is reduced. This is not accounted for in the synthesized data.

The synthesized data set was based upon three different background videos, and there is clearly difference in terms of counting performance (Figure 4.7). We observe a lower number density of counted bubbles in Background 2, compared to Background 1 and 3. In the corresponding videos, we find that this background has less visible flow of contrast agent. The increased flow of contrast agent in Background 1 and 3 create variations in the signal intensity. This may help in differentiating adjacent stuck bubbles from each other. Three different backgrounds are hardly enough to make a proper validation. The number of backgrounds were limited by the available data and the long processing time.

5.3 PERFORMANCE OF MOTION CORRECTION

The motion correction applied in this work, uses a linear affine transformation to correct for motion in image. This can not correct for local deformations in the tissue or movements out of the image plane. Hence, some videos are not free of motion. A tumor is in general quite rigid, and there is thus rarely local deformations within the tumor region. Non-linear (local) image registration is therefore unnecessary. Linear transformation has the benefit of being faster and more robust than non-linear transformations. The current motion correction program is slow (one to eight hours per video sequence). The number of pyramidal steps and iterations can be more closely evaluated to increase the speed, but this was not prioritized in this work.

5.4 PERFORMANCE OF THE COUNTING ALGORITHM

We observe a good correlation between the automatically and manually counted number density of phase-shift bubbles (Figure 4.16). This supports the credibility of the developed algorithm.

The performance of the counting algorithm for the entire synthesized data set was shown in Figure 4.8. The counting algorithm experiences a saturation when the inserted density passes $\sim$2 bubbles/mm^2 (Figure 4.12). This is an expected behaviour. When the density of bubbles increases, the chance of two or more bubbles being adjacent increases as well, and they may be counted as one large bubble (Figure 4.6). Although this is a drawback, it is important to note that most ($\sim$ 86%) of the counted number densities in the real data set is below 2 bubbles/mm (Figure 4.19). Hence, the error from saturation in the real data is limited.

If we only consider the lower end of the inserted density (Figure 4.9), there is almost a linear relationship between the counted and inserted number of bubbles. By swapping the axes and fitting a linear curve to the log-transformed data, we obtain an estimate of the accuracy and precision of the counting algorithm (Figure4.12). This figure displays the expected real number of bubbles for a given number of counted bubbles, and may be utilized to adjust the result. The relative standard deviation of the counting algorithm is almost constant, with a mean of 0.016 (Figure 4.11). This is an expected result, and support the speckle noise theory. The multiplicative nature of speckle noise implies a constant relative standard deviation.

5.5 COUNTING OF PHASE-SHIFT BUBBLES

The developed and validated algorithm is a tool that might increase the understanding of the activation, administration and behaviour of the ACT™ bubbles. Compared to manual counting, this program give increased efficiency, and a result with a known accuracy and precision. Another important improvement is that the automatic counting algorithm provides unbiased and reproducible results.

From Figure 4.18, and the corresponding statistical analysis, we found the significant difference between the low and high dose of phase-shift clusters. This make it possible to increase the therapeutic effect by increasing the dose, and it is an important result. The low dose is a 1:4 dilution of the high dose. The observed ratio between the mean of the high and low dose is ~2. This indicate that the increase in number of phase-shift bubbles is roughly half of the increased dose. However, the standard deviations are large.

There is a not a significant difference between the two transducers (different MI), but Figure 4.18 does favour the V-scan transducer (high MI). More research is necessary to determine the importance of the MI. The small size does also favour the V-scan, because of the increased usability.

Within all treatments the number of phase-shift bubbles is variable, and we found no relationship between tumor size and the number of phase-shift bubbles. This implies that there are other properties, such as the tumor vasculature, that affect the distribution of phase-shift bubbles. As mentioned in Section 2.2.1, the tumor vasculature differ from normal vasculature. Furthermore, the vasculature also vary between tumors, and it may even be heterogeneous within a tumor. These variations make it difficult to predict the number of deposited phase-shift bubbles within the tumor, solely based on the tumor size, injected dose, and applied MI. However, a more thorough examination of the tumor vasculature may help predicting the treatment outcome.

From the number density curves we observe the lifetime of the phase-shift bubbles (Appendix B). The theory (Section 2.1.11) predicted a lifetime of $\sim$ 3 minutes. This correlates well with the counted number density curves (Appendix B), However our results (Appendix B) indicate that there are bubbles present after $\sim$ 4 minutes. The first four tumors are counted over a time period exceeding ten minutes, and these data show bubbles present more than ten minutes after administration. This extended lifetime may be caused by activation of 'old' ACT™clusters. Note that the theory only provides a rough estimate of the bubble growth. The effect of blood flow and compression from surrounding tissue is not taken into account.

5.6 COMPARISON TO EXISTING PROGRAM (VISUAL SONICS)

In Figure 4.14 we present a comparison of the Visual Sonics and our program's performance in terms of motion correction and background subtraction. The improved background subtraction makes the single phase-shift bubbles more visible, and the noise and motion artefacts are strongly reduced. We still observe some motion in the video produced by our developed program. However, this motion is mainly outside the tumor region, and does not affect the counted number of bubbles.

5.7 NON-LINEAR IMAGING

The counting algorithm was tailored to linear contrast images. This imaging mode is suppose to enhance the phase-shift bubbles compared to Sonazoid™ microbubbles and tissue. From the time-intensity curves (Appendix C) we find that the total contrast is slightly larger in linear contrast mode, compared to non-linear contrast mode. On the other hand, the number density curves (Appendix B) display no difference between the two imaging modes, in terms of the counting performance. Hence, it is not possible to make a statement regarding choice of imaging mode based on our results.

We suspect that the raw ultrasound data from the non-linear mode contains some pulse encoding. Information about the encoding is not publicly available. We are therefore not able to fully reproduce the non-linear images produced by the Visual Sonics software. This complicates the use of the non-linear data.

6

CONCLUSION

A program for motion correction, background subtraction and counting of phase-shift bubbles is successfully developed, validated and applied to a data set containing 125 ultrasound image sequences of 16 different prostate tumor xenografts. The program has been validated qualitatively against prejudices regarding the phase-shift bubble behaviour. Our results have been compared to the results from manual counting, performed by Andrew Healey [69]. There is a very good correlation between the results obtained from automatic and manual counting. This support the credibility of the program. An estimate of the counting accuracy and precision is given.

We have shown that there is a significant increase ($p = 0.023$) in the number of phase-shift bubbles in tumors treated with a high dose. This implies that it is possible to increase the amount of locally delivered drug by increasing the total dose. We found no significant difference between the applied mechanical index used to activate the phase-shift bubbles. There was neither a relationship between the tumor size and the number of stuck phase-shift bubbles. This implies that other factors, such as the tumor vasculature, play an important role in the tumor treatment.

A synthesized data set of in total 81 videos, based on three different backgrounds, was created. For each video, a chosen number of synthesized phase-shift bubbles was inserted at a random time and position, and with a random intensity. The random values were drawn from appropriate distributions based on the real data set. This provided a quantitative validation of the program performance. For number densities below $\sim 2\,\text{bubbles/mm}^2$, the relation between the inserted and the counted number density is close to linear (Figure 4.12). Above $\sim 2\,\text{bubbles/mm}^2$ the program experience a saturation, and the accuracy decreases as the number density increases.

The output of the developed program fulfil the project requirements, and include a video (.avi-file) displaying the counted phase-shift bubbles and a data file (.mat-file) containing number and number density of counted phase-shift bubbles. The quality of the video is better than existing software, in terms of motion correction and visualization of phase-shift bubbles. Although this program is tailored to the ACT™ bubbles, the developed method may apply to similar problems.

The developed program will increase the counting efficiency. This enables further research and optimization of drug dose and ultrasound settings. We have shown that it there is a large variation in the number of stuck phase-shift bubbles for equal ACT™ cluster doses. However, the number of stuck phase-shift bubbles is directly related to the amount of locally deposited drug. Thus, we expect that the outcome of the ongoing chemotherapy treatment study, is more correlated to the number of stuck bubbles than the total injected dose. Therefore, imaging and counting during phase-shift bubble administration, using the developed program, is recommended for future and ongoing treatment studies. The improved correlation between treatment and effect, will decrease the number of animals needed to acquire a significant outcome difference between treatment protocols.

6.1 FURTHER WORK

The relationship between the tumor vasculature and the number of stuck phase-shift bubbles has not been investigated. The vasculature was imaged using only Sonazoid™microbubbles, but the data has not been processed. The total contrast signal in these videos can indicate the amount of functioning tumor vasculature. If these values are plotted versus the number of stuck phase-bubbles, it is possible determine the importance of the tumor vasculature. This may shed light on the difference in the number of phase-shift bubbles, observed within all treatment groups.

We have revealed that 'old' phase-shift bubbles are activated by high power ultrasound. The use of 'old' clusters, or clusters with smaller microbubbles, should be exploited. Possible applications are treatment of arteriosclerotic plaques with intravenous ultrasound, or treatment of superficial melanomas with high frequency ultrasound. The ACT™ treatment may also be improved by high power ultrasound bursts, 5-10 minutes after administration, as this can activate more phase-shift bubbles.

If this program is to be applied on data with number density of phase-shift bubbles above 2 bubbles/mm^2, effort should be put into reducing the experienced saturation. This saturation occurs because single bubbles are situated too close to each other, and therefore recognized as one large bubble. It should be possible to distinguish these separate bubbles by counting the number of local maxima within each bubble. This was tested without satisfying result, due to the inherent variations and noise present in ultrasound images. A more robust method may be achieved by smoothing the shape of the identified bubbles, before the number of local maxima is counted. Another option is to increasing the imaging frequency, and thereby the spatial resolution. Another obvious improvement of the program is to speed up the motion correction.

The lifetime of the stuck phase-shift bubbles were not properly evaluated. Our results indicate that some bubbles are still present after 4 minutes. To determine the *in vivo* lifetime, time intensity curves of single, stuck bubbles should be examined for an extended period of time. This may provide valuable information about the available time for the released drug to extravasate into the tumor tissue.

This program is based on linear contrast images. Some non-linear data were processed, but the model validation is based solely on linear contrast images. Based on our results, the algorithm seems to work equally well on non-linear and linear contrast images. But, in order to accurately determine the performance on non-linear images, a validation based on this imaging mode is necessary.

BIBLIOGRAPHY

[1] Cancer Reasearch UK. Cancer statitics key facts, all cancers combined., 2014. URL http://publications.cancerresearchuk.org/downloads/Product/CS_KF_ALLCANCERS.pdf.

[2] Rebecca Siegel, Jiemin Ma, Zhaohui Zou, and Ahmedin Jemal. Cancer statistics, 2014. *CA: a cancer journal for clinicians*, 64(1):9–29, 2014. ISSN 1542-4863. doi: 10.3322/caac.21208. URL http://www.ncbi.nlm.nih.gov/pubmed/24399786.

[3] Charles L Shapiro and Abram Recht. Side Effects of Adjuvant Treatment of Breast Cancer. *New England Journal of Medicine*, 344(26):1997–2008, 2001. doi: 10.1056/NEJM200106283442607. URL http://www.nejm.org/doi/full/10.1056/NEJM200106283442607.

[4] You Han Bae. Drug targeting and tumor heterogeneity. *Journal of controlled release : official journal of the Controlled Release Society*, 133(1):2–3, January 2009. ISSN 1873-4995. doi: 10.1016/j.jconrel.2008.09.074. URL http://www.pubmedcentral.nih.gov/articlerender.fcgi?artid=2627764&tool=pmcentrez&rendertype=abstract.

[5] Christian R Mayer, Nicolas A Geis, Hugo A Katus, and Raffi Bekeredjian. Ultrasound targeted microbubble destruction for drug and gene delivery. *Expert opinion on drug delivery*, 5(10):1121–38, October 2008. ISSN 1742-5247. doi: 10.1517/17425247.5.10.1121. URL http://www.ncbi.nlm.nih.gov/pubmed/18817517.

[6] Stuart Ibsen, Michael Benchimol, Dmitri Simberg, and Sadik Esener. Ultrasound mediated localized drug delivery. *Advances in experimental medicine and biology*, 733:145–53, January 2012. ISSN 0065-2598. doi: 10.1007/978-94-007-2555-3_14. URL http://www.ncbi.nlm.nih.gov/pubmed/22101720.

[7] Annemieke van Wamel, Klazina Kooiman, Miranda Harteveld, Marcia Emmer, Folkert J. ten Cate, Michel Versluis, and Nico de Jong. Vibrating microbubbles poking individual cells: drug transfer into cells via sonoporation. *Journal of controlled release : official journal*

of the Controlled Release Society, 112(2):149–55, May 2006. ISSN 0168-3659. doi: 10.1016/j.jconrel.2006.02.007. URL `http://www.sciencedirect.com/science/article/pii/S0168365906000733/pdf?md5=9f7c251bdf05bcab12f7491264e98a1c&pid=1-s2.0-S0168365906000733-main.pdf` `http://www.ncbi.nlm.nih.gov/pubmed/16556469`.

[8] Andrew Needles, O Couture, and F S Foster. A method for differentiating targeted microbubbles in real time using subharmonic micro-ultrasound and interframe filtering. *Ultrasound in medicine & biology*, 35(9):1564–73, September 2009. ISSN 1879-291X. doi: 10.1016/j.ultrasmedbio.2009.04.006. URL `http://www.ncbi.nlm.nih.gov/pubmed/19632763`.

[9] Peter R Hoskins, Kevin Martin, and Abigail Thrush. *Diagnostic ultrasound: physics and equipment*. Cambridge University Press, 2010. ISBN 1139488902.

[10] Maggie A Flower. *Webb's physics of medical imaging*. CRC Press, 2012. ISBN 0750305738.

[11] K K Shung and G A Thieme. *Ultrasonic Scattering in Biological Tissues*. Taylor & Francis, 1992. ISBN 9780849365683. URL `https://books.google.no/books?id=SSxI8Jx6fS8C`.

[12] Introduction Ultrasound, Didier Vray, Elisabeth Brusseau, Valérie Detti, François Varray, Adrian Basarab, Olivier Beuf, Olivier Basset, Christian Cachard, Hervé Liebgott, and Philippe Delachartre. *Ultrasound Medical Imaging*. Wiley Online Library, 2014.

[13] Andrew Healey. Basic physical principles of medical ultrasound contrast agents. (August), 2012.

[14] F Rancis A D Duck. NONLINEAR ACOUSTICS IN DIAGNOSTIC ULTRASOUND. 28(1):1–18, 2002.

[15] Lars Hoff. Acoustic characterization of contrast agents for medical ultrasound imaging, 2000.

[16] P N T Wells. *Physical principles of ultrasonic diagnosis*. Medical physics series. Academic Press, 1969. URL `http://books.google.no/books?id=WFlRAAAAMAAJ`.

[17] David T Blackstock. *Fundamentals of physical acoustics*. John Wiley & Sons, 2000.

[18] Charles C Church. The effects of an elastic solid surface layer on the radial pulsations of gas bubbles. *The Journal of the Acoustical Society of America*, 97 (3), 1995.

[19] Philip M Morse and K Ingard. Uno: Theoretical Acoustics, 1968.

[20] GE Healtcare. Optison. URL http://www3.gehealthcare.com/en/products/categories/contrast_media/optison.

[21] W. T. Shi, F. Forsberg, A. L. Hall, R. Y. Chiao, J.-B. Liu, S. Miller, K. E. Thomenius, M. A. Wheatley, and B. B. Goldberg. Subharmonic Imaging with Microbubble Contrast Agents: Initial Results. *Ultrasonic Imaging*, 21(2): 79–94, April 1999. ISSN 0161-7346. doi: 10.1177/016173469902100201. URL http://uix.sagepub.com/lookup/doi/10.1177/016173469902100201.

[22] William C Moss. Rayleigh - Plesset equation. 101(February 1997): 1187–1190, 2014.

[23] G Paradossi, P Pellegretti, and A Trucco. *Ultrasound contrast agents: Targeting and processing methods for theranostics*. Springer Milan, 2010. ISBN 9788847014947. URL https://books.google.no/books?id=8f62yNpwCE0C.

[24] N.R. Soman, J.N. Marsh, M.S. Hughes, G.M. Lanza, and S.A. Wickline. Acoustic Activation of Targeted Liquid Perfluorocarbon Nanoparticles Does Not Compromise Endothelial Integrity. *IEEE Transactions on Nanobioscience*, 5(2):69–75, June 2006. ISSN 1536-1241. doi: 10.1109/TNB.2006.875052. URL http://ieeexplore.ieee.org/lpdocs/epic03/wrapper.htm?arnumber=1637446.

[25] Esra Talu, Kanaka Hettiarachchi, Shukui Zhao, Robert L Powell, Abraham P Lee, L Longo, and Paul A Dayton. Possible Method for Improving Sensitivity in Molecular Imaging. 6(6):384–392, 2008.

[26] E Glen Tickner and Cardiology Division. WHY DO THE LUNGS CLEAR ULTRASONIC CONTRAST? 6, 1980.

[27] Nanda Navin C. History of Echocardiographic Contrast Agents. 20, 1997.

[28] Jonathan R Lindner. Microbubbles in medical imaging : current applications and future directions. 3(June):1–6, 2004.

[29] C A Macdonald and J Gomatam. Chaotic dynamics of microbubbles in ultrasonic fields. *Proceedings of the Institution of Mechanical Engineers, Part C: Journal of Mechanical Engineering Science*, 220(3):333–343, January 2006. ISSN 0954-4062. doi: 10.1243/095440606X79596. URL `http://pic.sagepub.com/lookup/doi/10.1243/095440606X79596`.

[30] Spiros Kotopoulis, Georg Dimcevski, Odd Helge Gilja, Dag Hoem, and Michiel Postema. Treatment of human pancreatic cancer using combined ultrasound, microbubbles, and gemcitabine: a clinical case study. *Medical physics*, 40(7):072902, July 2013. ISSN 0094-2405. doi: 10.1118/1.4808149. URL `http://www.ncbi.nlm.nih.gov/pubmed/23822453`.

[31] P A Dijkmans, L J M Juffermans, R J P Musters, A van Wamel, F J ten Cate, W van Gilst, C A Visser, N de Jong, and O Kamp. Microbubbles and ultrasound: from diagnosis to therapy. *European journal of echocardiography : the journal of the Working Group on Echocardiography of the European Society of Cardiology*, 5:245–256, 2004. ISSN 1525-2167. doi: 10.1016/j.euje.2004.02.001.

[32] Per Christian Sontum. Physicochemical characteristics of Sonazoid, a new contrast agent for ultrasound imaging. *Ultrasound in medicine & biology*, 34(5):824–33, May 2008. ISSN 0301-5629. doi: 10.1016/j.ultrasmedbio.2007.11.006. URL `http://www.ncbi.nlm.nih.gov/pubmed/18255220`.

[33] Andrew Healey. Batch PS0113 : Activated gas bubble size distribution dynamics via Sonometry system. 2013.

[34] Andrew Healey. Personal communication 21.12.2014, 2014.

[35] Annemieke Van Wamel, Andrew Healey, Per Christian Sontum, Svein Kv\aa{}le, Nigel Bush, Jeff Bamber, and Catharina De Lange Davies. Acoustic Cluster Therapy (ACT): a novel concept for targeted drug delivery - In vivo Characteristics and Proof of Principle. Technical report, 2014.

[36] L L Schramm. *Emulsions, Foams, and Suspensions: Fundamentals and Applications*. Wiley, 2006. ISBN 9783527606887. URL `https://books.google.no/books?id=qFi61f1NqNIC`.

[37] Rubin Battino. The ostwald coefficient of gas solubility. 15:231–240, 1984.

[38] T L Szabo. *Diagnostic Ultrasound Imaging: Inside Out*. Biomedical Engineering. Elsevier Science, 2013. ISBN 9780123965424. URL `https://books.google.no/books?id=wTYTAAAAQBAJ`.

[39] Roger John Benjamin King and Mike W Robins. *Cancer biology*. Pearson Education, 2006.

[40] Petros Koumoutsakos, Igor Pivkin, and Florian Milde. The Fluid Mechanics of Cancer and Its Therapy. *Annual Review of Fluid Mechanics*, 45(1):325–355, January 2013. ISSN 0066-4189. doi: 10.1146/annurev-fluid-120710-101102. URL `http://www.annualreviews.org/doi/abs/10.1146/annurev-fluid-120710-101102`.

[41] Naoyo Nishida, Hirohisa Yano, Takashi Nishida, Toshiharu Kamura, and Masamichi Kojiro. Angiogenesis in cancer. *Vascular Health and Risk Management*, 2(3):213–219, August 2006. ISSN 1176-6344. doi: 10.2147/vhrm.2006.2.3.213. URL `http://www.atypon-link.com/DMP/doi/abs/10.2147/vhrm.2006.2.3.213`.

[42] Yasuhiro Matsumura and Hiroshi Maeda. A New Concept for Macromolecular Therapeutics in Cancer Chemotherapy: Mechanism of Tumoritropic Accumulation of Proteins and the Antitumor Agent Smancs. *Cancer Research*, 46(12 Part 1):6387–6392, December 1986. URL `http://cancerres.aacrjournals.org/content/46/12_Part_1/6387.abstract`.

[43] Ethan J Halpern. Contrast-Enhanced Ultrasound Imaging of Prostate Cancer. 8:29–37, 2006.

[44] Rainer Go. Diagnostic v alue of high-resolution B-mode and power-mode sonography in the follow-up of thyroid cancer. *European Journal of Ultrasound*, 16, 2003.

[45] M D Rifkin, W Dähnert, and A B Kurtz. State of the art: endorectal sonography of the prostate gland. *AJR. American journal of roentgenology*, 154(4):691–700, 1990. ISSN 0361-803X.

[46] Rakesh K Jain. An Indirect Way to Tame Cancer. *Scientific American*, 310(2): 46–53, 2014. ISSN 0036-8733.

[47] Cristian Tomasetti and Bert Vogelstein. Variation in cancer risk among tissues can be explained by the number of stem cell divisions. *Science*, 2014. doi: 10.1126/science.1260825.

[48] Virgil Craig Jordan. *Estrogen/antiestrogen action and breast cancer therapy*. Univ of Wisconsin Press, 1986. ISBN 029910480X.

[49] R T Skeel and S N Khleif. *Handbook of Cancer Chemotherapy*. A Lippincott Williams & Wilkins Handbook. Lippincott Williams & Wilkins, 2011. ISBN 9781608317820. URL https://books.google.no/books?id=6Nz_87OLrtcC.

[50] Mousa Jafari, Bahram Zargar, and M Soltani. 15 Intelligent Drug Delivery Systems for Cancer Therapy. In *Biomedical Materials and Diagnostic Devices*, pages 477–515. Scrivener Publishing LLC, 2012.

[51] Thomas L Andresen, David H Thompson, and Thomas Kaasgaard. Enzyme-triggered nanomedicine: drug release strategies in cancer therapy. *Molecular membrane biology*, 27(7):353–63, October 2010. ISSN 1464-5203. doi: 10.3109/09687688.2010.515950. URL http://www.ncbi.nlm.nih.gov/pubmed/20939771.

[52] F B Hofmann, Editorial Board, J A Beavo, A Busch, D Ganten, M C Michel, C P Page, and W Rosenthal. *Handbook of Experimental Pharmacology*, volume 197. Springer, 2012. ISBN 9783642004766.

[53] Siv Eggen, Mercy Afadzi, Esben A Nilssen, Solveig Bj\{}rum Haugstad, Bj\o{}ern Angelsen, and Catharina De Lange Davies. Ultrasound improves the uptake and distribution of liposomal Doxorubicin in prostate cancer xenografts. *Ultrasound in medicine & biology*, 39(7):1255–66, July 2013. ISSN 1879-291X. doi: 10.1016/j.ultrasmedbio.2013.02.010. URL http://www.ncbi.nlm.nih.gov/pubmed/23643054.

[54] W L Nyborg. ULTRASONIC MICROSTREAMING AND RELATED PHENOMENA. pages 156–160, 1982.

[55] Philippe Marmottant and Sascha Hilgenfeldt. Controlled vesicle deformation and lysis by single oscillating bubbles. *Nature*, 423(6936): 153–156, May 2003. ISSN 0028-0836. URL http://www.nature.com/nature/journal/v423/n6936/suppinfo/nature01613_S1.html.

[56] W L Nyborg, William G Pitt, Ghaleb A Husseini, and Bryant J Staples. Ultrasonic drug delivery-a general review. *Expert opinion on drug delivery*, 1(1):37–56, 2004. ISSN 1742-5247.

[57] Yiyao Liu, Hirokazu Miyoshi, and Michihiro Nakamura. Encapsulated ultrasound microbubbles: therapeutic application in drug/gene delivery. *Journal of controlled release : official journal of the Controlled Release Society*, 114(1):89–99, August 2006. ISSN 0168-3659. doi: 10.1016/j.jconrel.2006.05.018. URL http://www.ncbi.nlm.nih.gov/pubmed/16824637.

[58] Joshua J Rychak, James Graba, A M Cheung, Bina S Mystry, Jonathan R Lindner, Robert S Kerbel, and F Stuart Foster. Microultrasound molecular imaging of vascular endothelial growth factor receptor 2 in a mouse model of tumor angiogenesis. *Molecular imaging*, 6(5):289–296, 2006. ISSN 1535-3508.

[59] S Zhao, D E Kruse, K W Ferrara, and P a Dayton. Selective imaging of adherent targeted ultrasound contrast agents. *Physics in Medicine and Biology*, 52(8):2055–2072, April 2007. ISSN 0031-9155. doi: 10.1088/0031-9155/52/8/002. URL http://stacks.iop.org/0031-9155/52/i=8/a=002?key=crossref.78c587daa7d1926dce5131beb07a7496.

[60] Johan Kirkhorn. *Introduction to IQ-demodulation of RF-data*. IFBT, NTNU, 1999. URL http://folk.ntnu.no/htorp/Undervisning/TTK10/IQdemodulation.pdf.

[61] Julius Smith. Analytic Signals and Hilbert Transform Filters. URL http://www.dsprelated.com/dspbooks/mdft/Analytic_Signals_Hilbert_Transform.html.

[62] Wolfram Mathworld. The Hilbert transform. URL http://mathworld.wolfram.com/HilbertTransform.html.

[63] Ronald E Crochiere and Lawrence R Rabiner. Interpolation and Decimation of Digital Signals- A tutorial review. *Proceedings of the IEEE*, 69(3):300–331, 1981.

[64] J B Antoine Maintz and Max A Viergever. A survey of medical image registration methods. In *Medical Image Analysis*, volume 2, pages 1–36. Oxford University Press, 1998.

[65] Paul Viola and William M Wells III. Alignment by Maximization of Mutual Information. 24(2):137–154, 1997.

[66] F Maes, A Collignon, D Vandermeulen, G Marchal, and P Suetens. Multimodality image registration by maximization of mutual information. *Medical Imaging, IEEE Transactions on*, 16(2):187–198, April 1997. ISSN 0278-0062. doi: 10.1109/42.563664.

[67] A Gosavi. *Simulation-Based Optimization: Parametric Optimization Techniques and Reinforcement Learning*. Operations Research/Computer Science Interfaces Series. Springer, 2003. ISBN 9781402074547. URL https://books.google.no/books?id=XqKyW9U3PWAC.

[68] Tonya Coulthard. VisualSonics White Paper : Nonlinear Contrast Agent Imaging with a High Frequency Linear. 2009. URL `http://www.visualsonics.com/sites/default/files/WP_2100_NA_Nonlinear_Contrast_Agent.pdf`.

[69] Andrew Healey. *Processing notes: First cohort NTNU imaging pilot study #2*. 2014.

[70] Annemieke van Wamel and Andrew Healey. Personal communication with Annemieke van Wamel and Andrew Healey 13.01.2015., 2015.

[71] T G Leighton. Derivation of the Rayleigh-Plesset equation in terms of volume. Technical Report 308, University of Southampton, 2007.

A

DERIVATION OF THE RAYLEIGH-PLESSET EQUATION

The Rayleigh-Plesset equation is an ordinary differential equation which describe the non-linear oscillation of a gas bubble suspended in an infinite liquid, subject to an external sound wave. This equation is in the following derived using the energy balance between the liquid and the gas bubble [22]. The equation can also be derived from the Navier-Stokes equations [71].

A few assumptions are required for the following derivation to be valid. We assume the wavelength of the pressure field to be way larger then the size of the gas bubble, i.e. $d \ll \lambda$. The bubble is spherical and spatially uniform conditions within the bubble exist at all times. We can neglect gravity and bulk viscosity. There is no flow of either matter of heat through the boundary of the bubble. The density of the gas is significantly smaller then the liquid density, and the gas within the bubble can be considered an ideal gas. Using these assumptions the oscillation will be an adiabatic process. Newton's notation for the time-derivative is used.

Consider an oscillating bubble suspended in incompressible fluid. Because of the incompressibility of the fluid, the fluid velocity $u(r,t)$ has to follow the inverse square law, i.e.

$$u(r,t) = \frac{R(t)^2}{r(t)^2}\dot{R}(t). \tag{A.1}$$

Here $r_b(t)$ is the bubble radius, $\dot{r}_b(t)$ the velocity of the boundary and r any radius larger or equal r_b.

The kinetic energy E_k of the fluid caused by the oscillating bubble is then

$$E_k = \frac{\rho_l}{2}\int_{r_b}^{\infty} u(r,t)4\pi r^2 \,\mathrm{d}r = 2\pi\rho_l r_b^3 \dot{r}_b^2, \tag{A.2}$$

where ρ_l is the liquid density.

Far from the bubble the liquid pressure is given by $p_\infty(t) = p_0 + p(t)$, where $p(t) = p_a e^{i\omega t}$ is the time varying pressure caused by the sound wave and p_0 the hydrostatic pressure. For an adiabatic process we have that $pV^\gamma =$ constant. Here V is the volume, p the pressure and γ the adiabatic index. The pressure is then only a function the bubble radius r_b,

$$p(r_b) = p_{r_0}\left(\frac{V_{r_0}}{V(r_b)}\right)^\gamma = p_{r_0}\left(\frac{r_0}{r_b}\right)^{3\gamma}, \tag{A.3}$$

where r_0 and p_{r_0} are the equilibrium radius and pressure.

The work done to expand the bubble is only carried out by the net pressure, $\Delta p = P(r_b) - P_\infty(t)$, and the total work W is

$$W = \int \Delta p dV = \int_{r_0}^{r_b} (p(r_b) - p_{\infty(t)}) 4\pi r_b^2 \, \mathrm{d}r_b. \tag{A.4}$$

The kinetic energy of the liquid must equal the work, and the Rayleigh-Plesset equation is obtained by equating and differentiating Equation (A.2) and (A.4) with respect to r_b,

$$\frac{p_{r_0}\left(\frac{r_0}{r_b}\right)^{3\gamma} - p_0 - p(t)}{\rho_l} = \frac{3\dot{r}_b^2}{2} + r_b\ddot{r}_b. \tag{A.5}$$

Note that $\frac{d\dot{r}_b^2}{dr-b} = 2\ddot{r}_b$.

B

NUMBER DENSITY CURVES

Number density curves as a function of time for all 16 animals are given below. Black and red data points represent data from linear contrast and non-linear imaging modes, respectively.

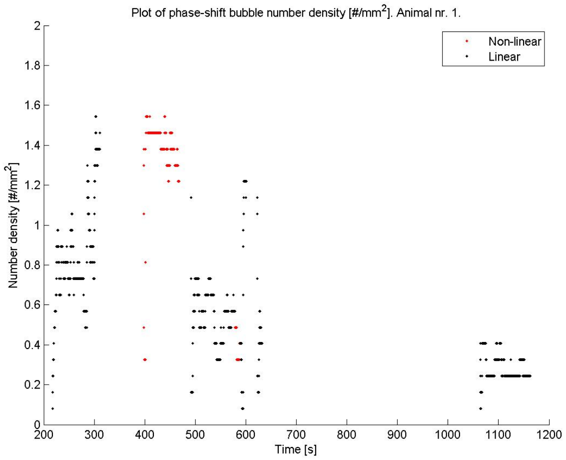

Figure B.1: Number density curve for animal number 1. Black and red data points represent data from linear contrast and non-linear imaging modes, respectively.

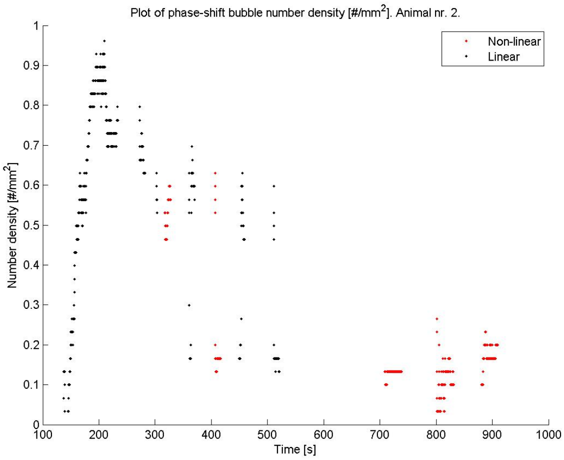

Figure B.2: Number density curve for animal number 2. Black and red data points represent data from linear contrast and non-linear imaging modes, respectively.

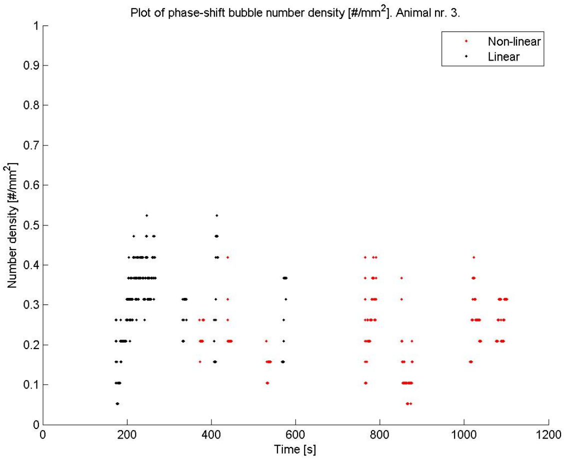

Figure B.3: Number density curve for animal number 3. Black and red data points represent data from linear contrast and non-linear imaging modes, respectively.

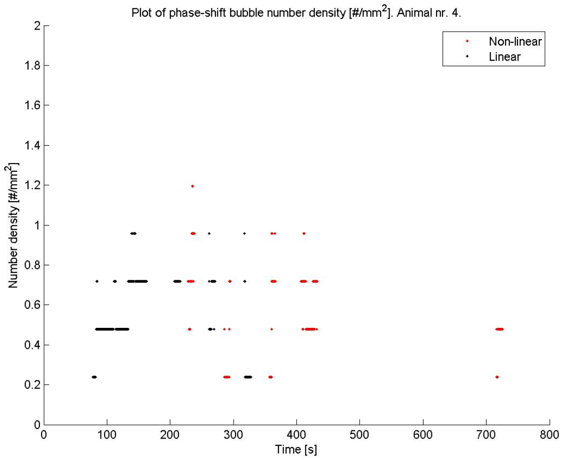

Figure B.4: Number density curve for animal number 4. Black and red data points represent data from linear contrast and non-linear imaging modes, respectively.

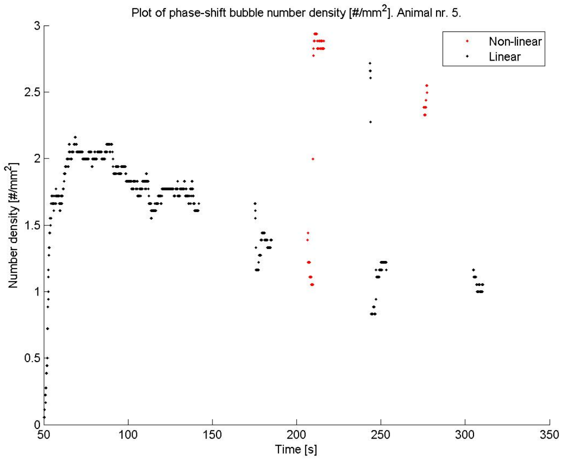

Figure B.5: Number density curve for animal number 5. Black and red data points represent data from linear contrast and non-linear imaging modes, respectively.

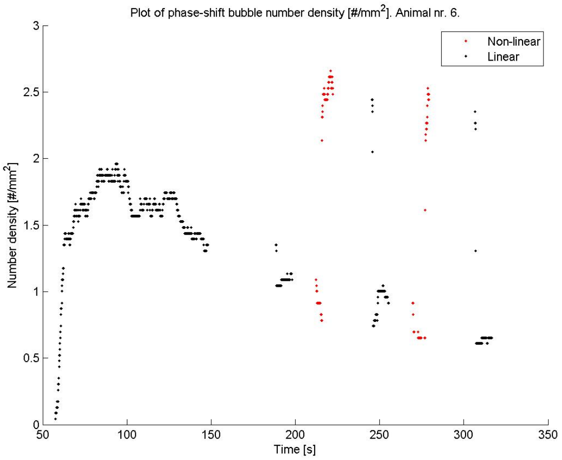

Figure B.6: Number density curve for animal number 6. Black and red data points represent data from linear contrast and non-linear imaging modes, respectively.

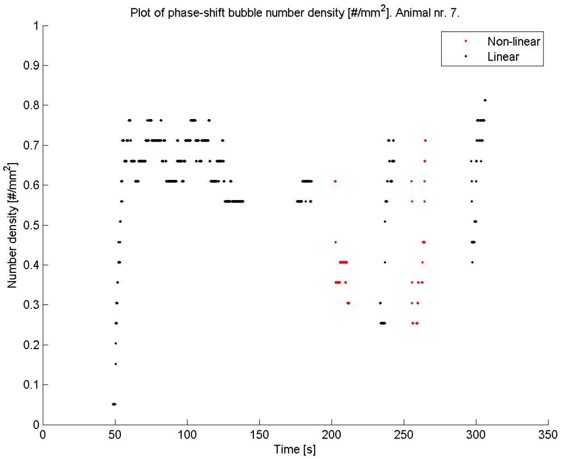

Figure B.7: Number density curve for animal number 7. Black and red data points represent data from linear contrast and non-linear imaging modes, respectively.

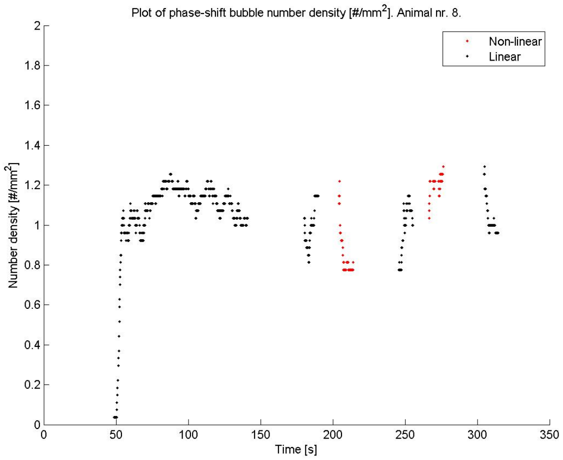

Figure B.8: Number density curve for animal number 8. Black and red data points represent data from linear contrast and non-linear imaging modes, respectively.

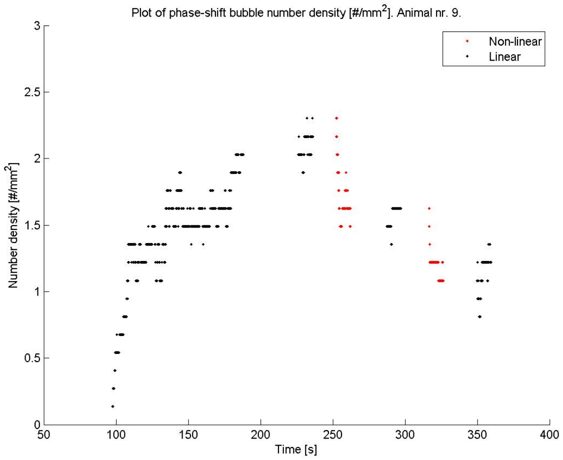

Figure B.9: Number density curve for animal number 9. Black and red data points represent data from linear contrast and non-linear imaging modes, respectively.

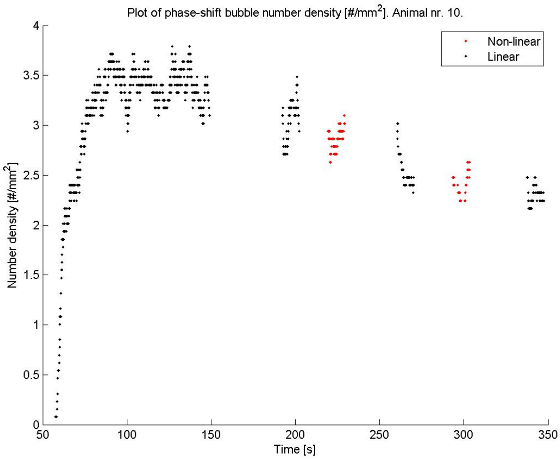

Figure B.10: Number density curve for animal number 10. Black and red data points represent data from linear contrast and non-linear imaging modes, respectively.

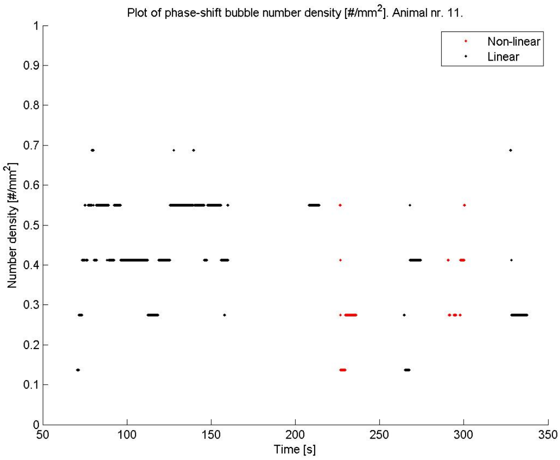

Figure B.11: Number density curve for animal number 11. Black and red data points represent data from linear contrast and non-linear imaging modes, respectively.

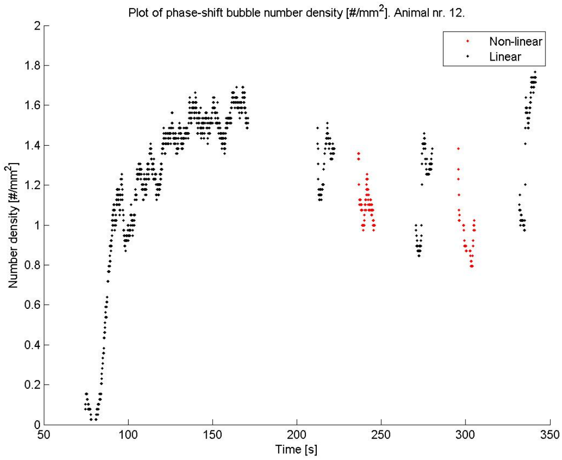

Figure B.12: Number density curve for animal number 12. Black and red data points represent data from linear contrast and non-linear imaging modes, respectively.

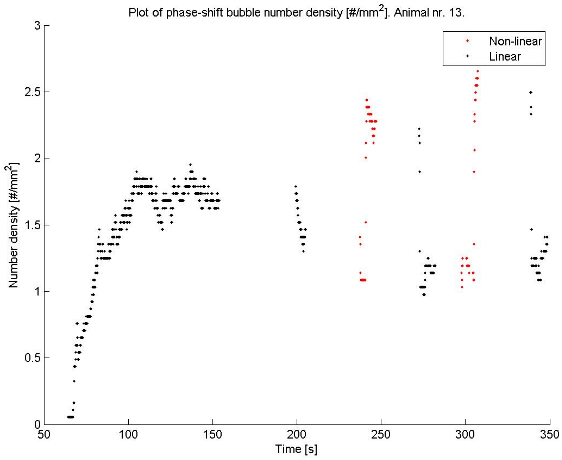

Figure B.13: Number density curve for animal number 13. Black and red data points represent data from linear contrast and non-linear imaging modes, respectively.

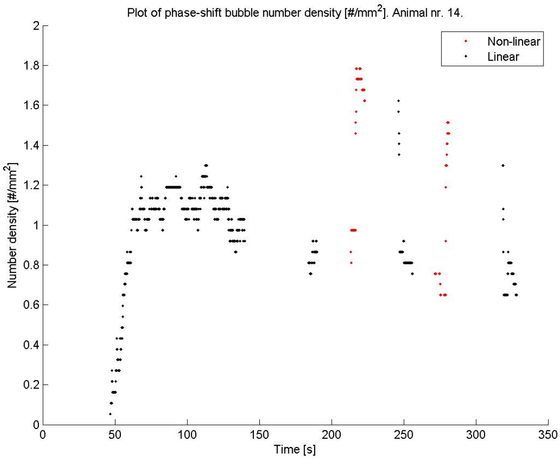

Figure B.14: Number density curve for animal number 14. Black and red data points represent data from linear contrast and non-linear imaging modes, respectively.

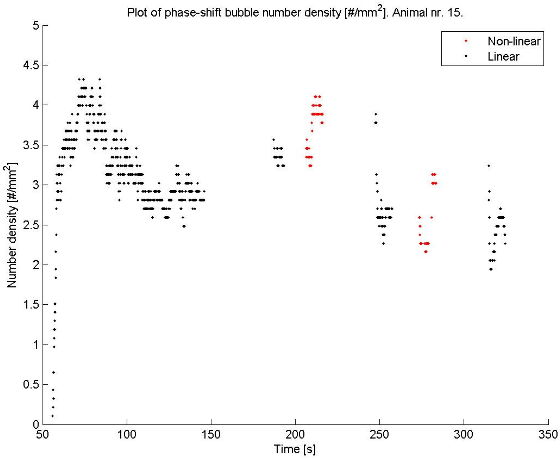

Figure B.15: Number density curve for animal number 15. Black and red data points represent data from linear contrast and non-linear imaging modes, respectively.

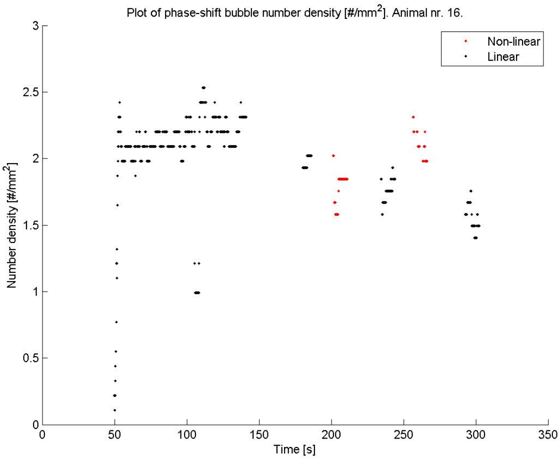

Figure B.16: Number density curve for animal number 16. Black and red data points represent data from linear contrast and non-linear imaging modes, respectively.

C

TIME-INTENSITY CURVES

Time-intensity curves for all 16 animals are presented below. Black and red data points represent data from linear contrast and non-linear imaging modes, respectively.

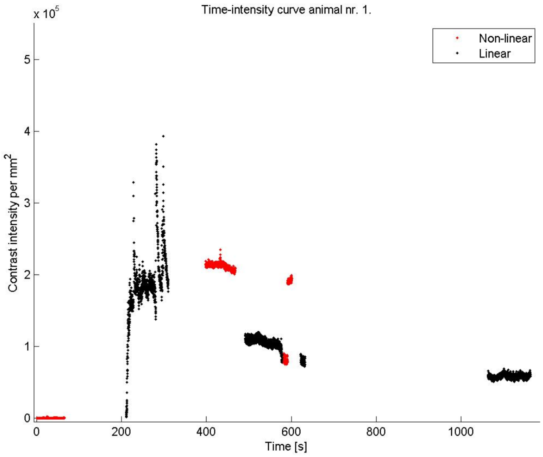

Figure C.1: Time-intensity curve for animal number 1. Black and red data points represent data from linear contrast and non-linear imaging modes, respectively.

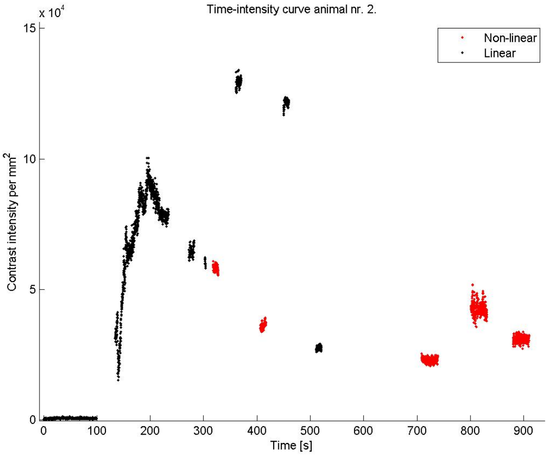

Figure C.2: Time-intensity curve for animal number 2. Black and red data points represent data from linear contrast and non-linear imaging modes, respectively.

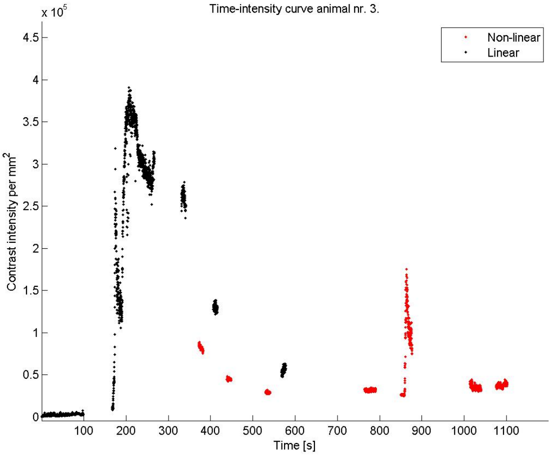

Figure C.3: Time-intensity curve for animal number 3. Black and red data points represent data from linear contrast and non-linear imaging modes, respectively.

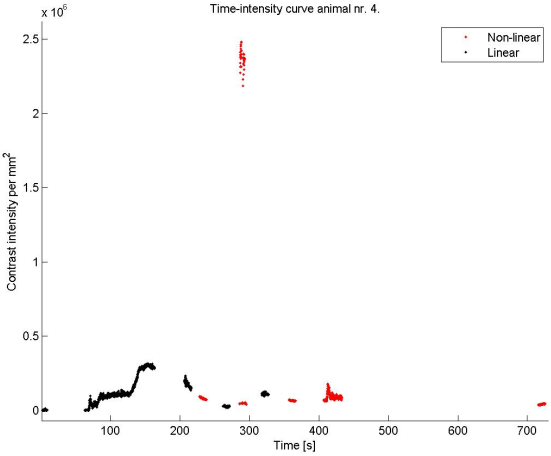

Figure C.4: Time-intensity curve for animal number 4. Black and red data points represent data from linear contrast and non-linear imaging modes, respectively.

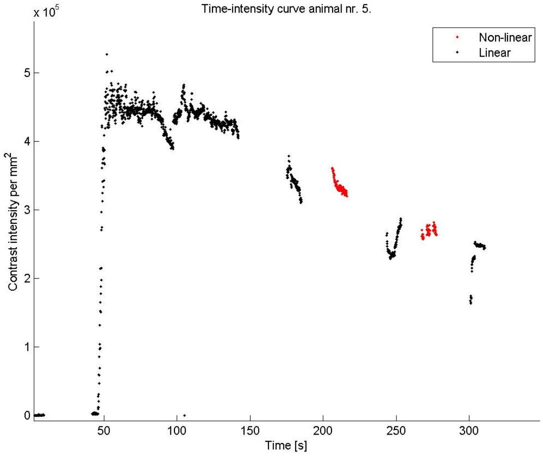

Figure C.5: Time-intensity curve for animal number 5. Black and red data points represent data from linear contrast and non-linear imaging modes, respectively.

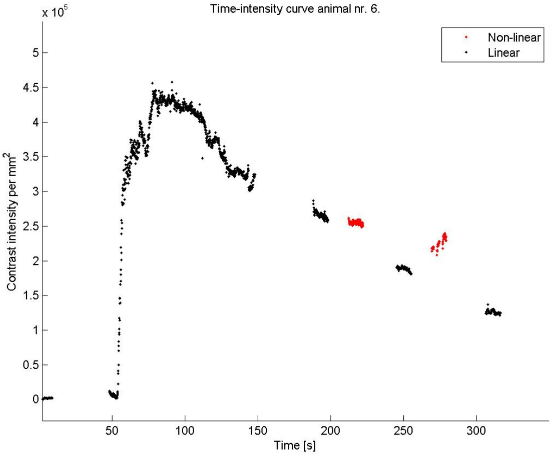

Figure C.6: Time-intensity curve for animal number 6. Black and red data points represent data from linear contrast and non-linear imaging modes, respectively.

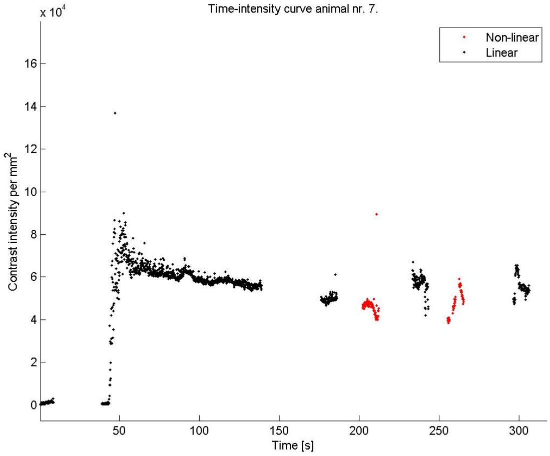

Figure C.7: Time-intensity curve for animal number 7. Black and red data points represent data from linear contrast and non-linear imaging modes, respectively.

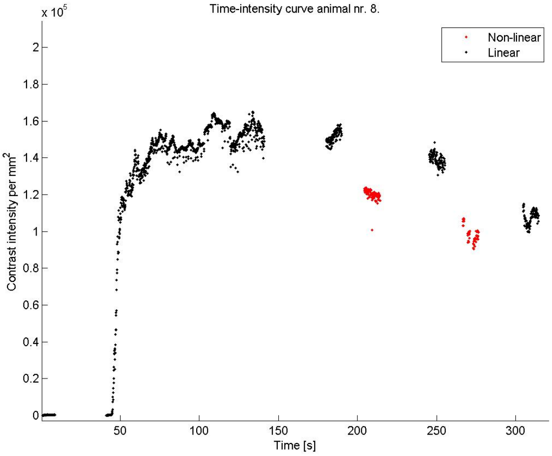

Figure C.8: Time-intensity curve for animal number 8. Black and red data points represent data from linear contrast and non-linear imaging modes, respectively.

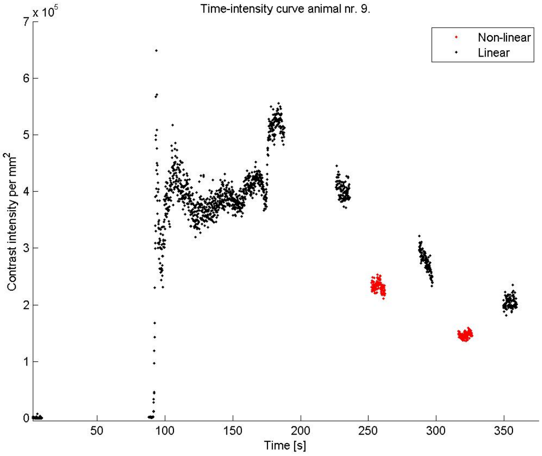

Figure C.9: Time-intensity curve for animal number 9. Black and red data points represent data from linear contrast and non-linear imaging modes, respectively.

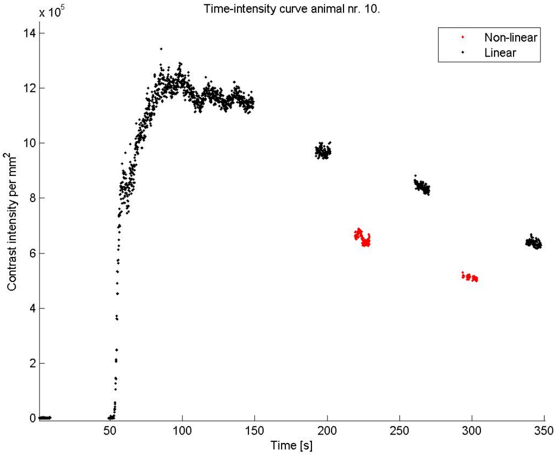

Figure C.10: Time-intensity curve for animal number 10. Black and red data points represent data from linear contrast and non-linear imaging modes, respectively.

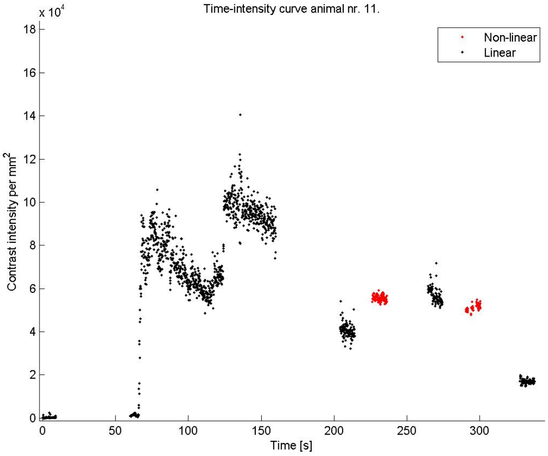

Figure C.11: Time-intensity curve for animal number 11. Black and red data points represent data from linear contrast and non-linear imaging modes, respectively.

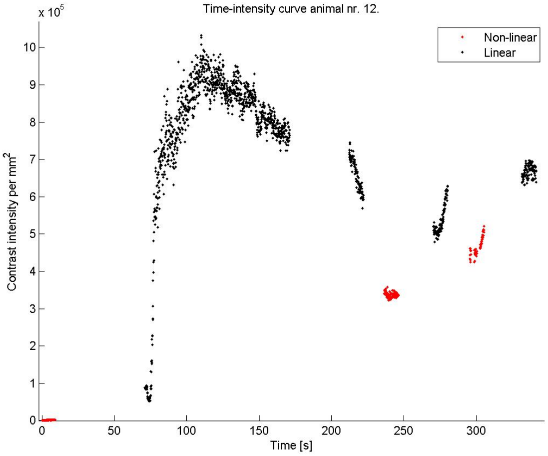

Figure C.12: Time-intensity curve for animal number 12. Black and red data points represent data from linear contrast and non-linear imaging modes, respectively.

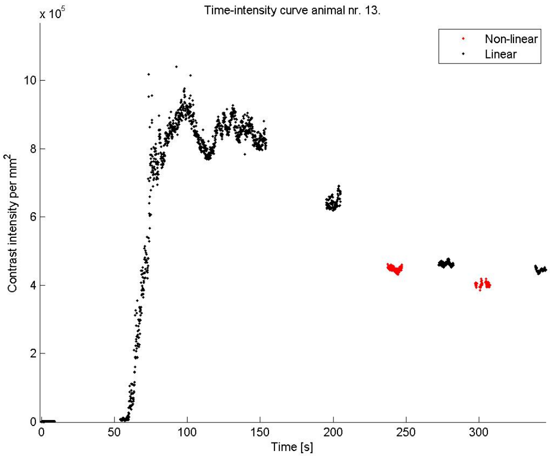

Figure C.13: Time-intensity curve for animal number 13. Black and red data points represent data from linear contrast and non-linear imaging modes, respectively.

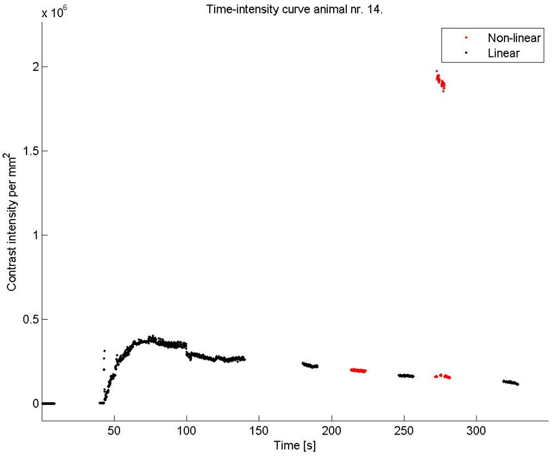

Figure C.14: Time-intensity curve for animal number 14. Black and red data points represent data from linear contrast and non-linear imaging modes, respectively.

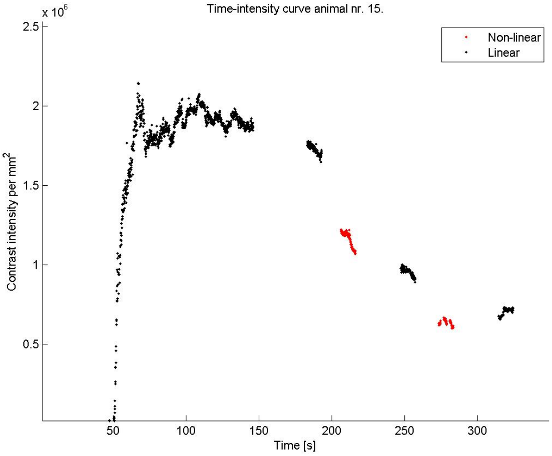

Figure C.15: Time-intensity curve for animal number 15. Black and red data points represent data from linear contrast and non-linear imaging modes, respectively.

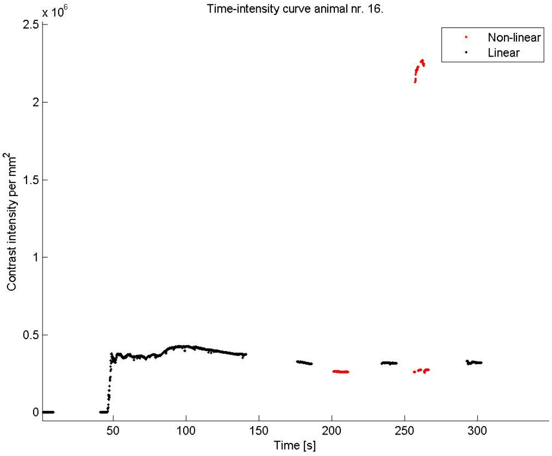

Figure C.16: Time-intensity curve for animal number 16. Black and red data points represent data from linear contrast and non-linear imaging modes, respectively.

D

RAW COUNTING RESULTS

A key columns from the counting results of the real ultrasound data are presented in Table D.1. The full results are found in `E:\excel\counting sheet.xlsx`. The full information about the synthesize data set is found at`E:\excel\counting sheet synthesized data.xlsx`).

Table D.1: Counted real ultrasound data.

File id	Animal nr	Density of bubbles (automatic)	Density of bubbles (manual)
2014-11-04-15-29-07	0		
2014-11-04-15-31-39	0		
2014-11-04-15-36-35	0		
2014-11-04-15-38-42	0		
2014-11-04-15-40-50	0		
2014-04-28-10-37-22.rf	1	0.00	
2014-04-28-10-40-53.rf	1	1.54	0.75
2014-04-28-10-44-00.rf	1	1.54	
2014-04-28-10-45-33.iq	1	0.73	
2014-04-28-10-47-00.rf	1	1.22	
2014-04-28-10-47-31.rf	1	0.57	
2014-04-28-10-54-52.iq	1	0.41	
2014-04-29-09-43-36.iq	2	0.00	
2014-04-29-09-45-50.iq	2	0.96	1.35
2014-04-29-09-48-08.iq	2	0.73	

Table D.1: Counted real ultrasound data.

File id	Animal nr	Density of bubbles (automatic)	Density of bubbles (manual)
2014-04-29-09-48-38.iq	2	0.63	
2014-04-29-09-48-53.rf	2	0.60	
2014-04-29-09-49-36.iq	2	0.70	
2014-04-29-09-50-22.rf	2	0.17	
2014-04-29-09-51-05.iq	2	0.63	
2014-04-29-09-52-06.iq	2	0.17	
2014-04-29-09-55-24.rf	2	0.13	
2014-04-29-09-56-56.rf	2	0.20	
2014-04-29-09-58-15.rf	2	0.23	
2014-04-30-08-45-53.iq	3	0.00	
2014-04-30-08-48-40.iq	3	0.52	0.36
2014-04-30-08-51-24.iq	3	0.31	
2014-04-30-08-52-05.rf	3	0.26	
2014-04-30-08-52-39.iq	3	0.52	
2014-04-30-08-53-11.rf	3	0.21	
2014-04-30-08-54-43.rf	3	0.16	
2014-04-30-08-55-20.iq	3	0.37	
2014-04-30-08-58-37.rf	3	0.42	
2014-04-30-09-00-03.rf	3	0.21	
2014-04-30-09-02-46.rf	3	0.42	
2014-04-30-09-03-48.rf	3	0.31	
2014-05-04-11-37-15.iq	4	0.00	
2014-05-04-11-38-18.iq	4	0.96	0.5
2014-05-04-11-40-41.iq	4	0.72	
2014-05-04-11-41-03.rf	4	1.20	
2014-05-04-11-41-36.iq	4	0.72	
2014-05-04-11-42-00.rf	4	0.72	
2014-05-04-11-42-32.iq	4	0.24	

Table D.1: Counted real ultrasound data.

File id	Animal nr	Density of bubbles (automatic)	Density of bubbles (manual)
2014-05-04-11-43-11.rf	4	0.96	
2014-05-04-11-44-01.rf	4	0.96	
2014-05-04-11-49-10.rf	4	0.48	
2014-05-02-10-39-41.iq	5	0.00	
2014-05-02-10-40-23.iq	5	2.16	1.625
2014-05-02-10-42-36.iq	5	1.44	
2014-05-02-10-43-07.rf	5	2.94	
2014-05-02-10-43-44.iq	5	1.22	
2014-05-02-10-44-08.rf	5	2.55	
2014-05-02-10-44-41.iq	5	1.16	
2014-05-03-09-52-43.iq	6	0.00	
2014-05-03-09-53-31.iq	6	1.96	1.6
2014-05-03-09-55-51.iq	6	1.13	
2014-05-03-09-56-15.rf	6	2.66	
2014-05-03-09-56-48.iq	6	1.05	
2014-05-03-09-57-12.rf	6	2.53	
2014-05-03-09-57-49.iq	6	0.65	
2014-05-03-10-28-05.iq	7	0.00	
2014-05-03-10-28-44.iq	7	0.76	0.886
2014-05-03-10-31-01.iq	7	0.61	
2014-05-03-10-31-27.rf	7	0.41	
2014-05-03-10-31-58.iq	7	0.71	
2014-05-03-10-32-20.rf	7	0.71	
2014-05-03-10-33-01.iq	7	0.81	
2014-05-03-11-26-50.iq	8	0.00	
2014-05-03-11-27-31.iq	8	1.26	1.34
2014-05-03-11-29-50.iq	8	1.15	
2014-05-03-11-30-14.rf	8	0.92	

Table D.1: Counted real ultrasound data.

File id	Animal nr	Density of bubbles (automatic)	Density of bubbles (manual)
2014-05-03-11-30-55.iq	8	1.15	
2014-05-03-11-31-16.rf	8	1.29	
2014-05-03-11-31-54.iq	8	1.11	
2014-04-30-10-02-26.iq	9	0.00	
2014-04-30-10-03-54.iq	9	2.03	2.2
2014-04-30-10-06-12.iq	9	2.30	
2014-04-30-10-06-38.rf	9	1.90	
2014-04-30-10-07-13.iq	9	1.62	
2014-04-30-10-07-42.rf	9	1.22	
2014-04-30-10-08-15.iq	9	1.35	
2014-04-30-10-53-51.iq	10	0.00	
2014-04-30-10-54-40.iq	10	3.79	3.83
2014-04-30-10-57-03.iq	10	3.48	
2014-04-30-10-57-30.rf	10	3.10	
2014-04-30-10-58-11.iq	10	2.71	
2014-04-30-10-58-44.rf	10	2.63	
2014-04-30-10-59-28.iq	10	2.48	
2014-05-04-10-33-26.iq	11	0.00	
2014-05-04-10-34-26.iq	11	0.69	0.76
2014-05-04-10-36-50.iq	11	0.55	
2014-05-04-10-37-12.rf	11	0.27	
2014-05-04-10-37-50.iq	11	0.55	
2014-05-04-10-38-16.rf	11	0.55	
2014-05-04-10-38-53.iq	11	0.27	
2014-05-04-12-09-24.rf	12	0.00	
2014-05-04-12-10-35.iq	12	1.69	1.76
2014-05-04-12-12-56.iq	12	1.51	
2014-05-04-12-13-20.rf	12	1.25	

Table D.1: Counted real ultrasound data.

File id	Animal nr	Density of bubbles (automatic)	Density of bubbles (manual)
2014-05-04-12-13-54.iq	12	1.46	
2014-05-04-12-14-19.rf	12	1.02	
2014-05-04-12-14-55.iq	12	1.77	
2014-05-01-11-22-10.iq	13	0.00	
2014-05-01-11-23-04.iq	13	1.95	2.42
2014-05-01-11-25-25.iq	13	1.79	
2014-05-01-11-26-07.rf	13	2.44	
2014-05-01-11-26-42.iq	13	1.25	
2014-05-01-11-27-07.rf	13	2.66	
2014-05-01-11-27-48.iq	13	1.41	
2014-05-01-13-29-22.iq	14	0.00	
2014-05-01-13-30-02.iq	14	1.30	0.82
2014-05-01-13-32-22.iq	14	0.92	
2014-05-01-13-32-55.rf	14	1.78	
2014-05-01-13-33-28.iq	14	0.92	
2014-05-01-13-33-53.rf	14	1.51	
2014-05-01-13-34-40.rf	14	0.87	
2014-05-02-09-33-06.iq	15	0.00	
2014-05-02-09-33-52.iq	15	4.32	4.6
2014-05-02-09-36-09.iq	15	3.56	
2014-05-02-09-36-32.rf	15	4.10	
2014-05-02-09-37-13.iq	15	2.81	
2014-05-02-09-37-39.rf	15	3.13	
2014-05-02-09-38-20.iq	15	2.70	
2014-05-03-11-57-58.iq	16	0.00	
2014-05-03-11-58-39.iq	16	2.53	2.21
2014-05-03-12-00-54.iq	16	2.02	
2014-05-03-12-01-19.rf	16	1.84	

Table D.1: Counted real ultrasound data.

File id	Animal nr	Density of bubbles (automatic)	Density of bubbles (manual)
2014-05-03-12-01-52.iq	16	1.93	
2014-05-03-12-02-14.rf	16	2.20	
2014-05-03-12-02-50.iq	16	1.76	

E

MATLAB FILES

The program developed in this work is written in Matlab. All written Matlab files and a short description is given in the table below (E.1). Note that the key files are written in bold text. The actual Matlab files are found in `E:\mfiles\`. A simple description on how to use the program is given in the following paragraph.

The main file in this program is *run_program.m*. The first input is the full file name of the raw ultrasound data (e.g. `D:\Ultrasound image data\2014-04-28-10-23-41.rf`). The second input argument is an array of frame numbers from which the background should be computed (e.g. `1:10`). The third and fourth argument are true/false statements. The decide if counting or background subtraction is performed, respectively. The fifth and sixth argument may be omitted, if the background file is based on frames within the video given in argument one. The sixth argument is the full file name of a .mat file, where the correlation matrix for the previous video is stored (e.g.`C:\Phaseshiftcounting\2014-05-02-10-44-08\_PS\_count.mat`). This allow the counting of phase-shift bubble to continue from where the last video ended. The *run_program.m* perform motion correction, background subtraction and counting, in the respective order. The computation time will depend on the computer performance and the size of the raw ultrasound file, but between one and ten hours per file must be expected. Note that this script load and save several files to directories available on my computer. Directories and file names in the Matlab files may therefore be corrected for the program to work properly. the An example on how to run through a large set of ultrasound image data is given in *batch_process.m*

Table E.1: List of Matlab files. The most important files are written in bold text.

Name	Input	Output	Function
align_image.m	fixed image, moving image, transformation type, max iterations, initial transform, max step length)		Align the moving image to the fixed image using MATLAB functions imregtform and imwarp.
all_counted_vs_inserted.m			Perform non-linear fit of synthesized data
batch_process.m			This script perform batch processing of the rf-data specified in `counting sheet.xlsx`. For all file names, the function run_program is launched.
bubble_count_curve.m		.mat files	Produce .mat files containing data later used for plotting of Number density as a function of time
bubble_density.m	Number of bubbles, region of interest, Bmode parameters	number density	Compute number density from a given number of bubbles and a ROI.
bubble_growth.m			Estimate bubble growth curve from existing single bubble tic curve
bubble_tic.m		.mat files	Produce .mat files with data later used to plot tic-curves

Table E.1: List of Matlab files. The most important files are written in bold text.

Name	Input	Output	Function
bubble_zoom.m	frames, chosen pixels, show images(true/false)	maximum intensity	Zoom in on a region defined by the chosen pixels, and produce a smoothed close up video of these pixels.
color_code.m	frame, contrast mask	RGB image	Colour the contrast green in the .avi files.
compare_manual_and_auto_count.m		Figures	Make histograms comparing manually and automatically counted data.
counted_vs_inserted.m			Compare results from the three different backgrounds
count_max_real_data.m		.txt file	Count the maximum counted number of phase-shift bubble for each video, and store in .txt file.
count_PS_bubbles.m	motion corrected file name, subtracted file name	.avi file and .mat file	Count the number of phase-shift bubbles and make the final .avi file.
do_subtraction.m	frames	subtracted frames and background frame	Compute background and subtract the background from all frames.
draw_roi.m	frame	ROI	Allow the user to draw a ROI on a frame.
evalc2decimal.m	string	decimal number	Convert a string to a decimal number

Table E.1: List of Matlab files. The most important files are written in bold text.

Name	Input	Output	Function
frame_counter.m	Full file name of raw US data	Total number of frames in file	Count the number ov video frames in a raw file (.rf/.iq)
get_background.m	Frames	background	Compute background by maximum projection of the given frames
get_correlation.m	frame A, frame B,	correlation	Compute correlation between two frames
get_growth_intensity.m	max intensity, start frame, length	intensity array	Multiply the intensity obtained with growth_fun.m to obtain correct intensity function
get_param.m	file name raw US data	image parameter	Obtain image parameters
get_RF_from_IQ.m	Full file name of raw US data, frame number	RF data, parameters	Obtain RF-data from IQ data.
get_tic.m	file_reference, t	intensity array	Compute time intensity curve for a file given by the file reference. t(seconds) is a time array.
growth_fun.m	frame numbers	growth function	Calculate the bubble growth function for the given frame numbers
hms2sec.m	d1,h1, m1, s1, d2, h2, m2, s2	seconds	Compute seconds elapsed between two timestamps.

Table E.1: List of Matlab files. The most important files are written in bold text.

Name	Input	Output	Function
im_sub.m	frame A, frame B, type	Difference frame	Subtract frame B from A, and set all values less than zero equal to zero.
insert_bubble.m	Intensity, x-position, y-position, frame	frame with bubble	Insert a synthesized bubble at a given position and and intensity given in the given frame
investigate_pixels.m		Figures	Plot the intensity as a function of frame for a given pixel.
log_compress_2.m	array, 'compress/decompress'	array	Approximation to log-compression(envelope) in log_compress.m Can compress or decompress.
log_compress.m	RF-data	compressed data	Perform hilbert transform and log compression on RF-data
make_intensity_distribution.m		probability object	Compute probability density function for the intensity distribution.
make_ref_frame.m	Full filename, frame indexes, extension(rf/iq)	reference frame and parameters	Make reference frame for motion correction.
mat2avi.m	filename	.avi file	Contruct .avi file from .mat file
motion_correction.m	Filename(mat file)	motion corrected .mat file	Compute motion corrected .mat file from a .mat file

Table E.1: List of Matlab files. The most important files are written in bold text.

Name	Input	Output	Function
mse.m	frame A, frame B	Mean square error	Compute mean square error between two frames.
plot_bubble_count_curve.m		Figures	Plot bubble count curves from .mat files produced with bubble_count_curve.m
plot_bubble_tic.m		Figures	Plot tic curves from the .mat files produced with bubble_tic.m
plot_tic_curves.m	Counted .mat file name, subtracted .mat file name	time array, intensity curves	Calculate intensity curves for single bubbles and show close-up video of bubbles.
point_spread_fun.m			Calculate the PSF from an identified bubble.
progressbar.m	ratio	Figure	Show progress bar. Public available script.
psf.m			return the PSF
random_intensity.m	intensity distribution	intensity	Draw a random intensity from the intensity distribution.
random_position.m	Roi, N	x and y coordinate	Draw N random positions within ROI.
ReadRF.m	full filename, mode name, and frame number	RF data, parameters	Read in RF data. Written by A.Healey.
RF2mat.m	Full filename	.mat file	Convert raw US data to .mat file.

Table E.1: List of Matlab files. The most important files are written in bold text.

Name	Input	Output	Function
run_program.m	File name raw US data, background frame index, count(true/false), bg_subtraction(true/false), background file name, correlation array file name.	.avi file and . Mat file	Perform all processing from raw US data to counted .avi file and .mat file. If count or background_subtraction is false, the program will not perform these tasks. Background file name must be included if the background is supposed to be made from another file. Correlation array file name is the name of the previous video sequence.
subtraction_fun.m	File name motion corrected .mat file, indexes for background	.mat file(subtracted data)	Create background file, and subtract the background from all frames. Save subtracted frames as .mat file
time_array_from_time_stamps.m	time stamp 1, time stamp 2.	time array(seconds)	Make time array from two time stamps
VsiBModeIQ.m	Full file name, mode name, and frame number	IQ data and parameters	Compute IQ data from RF-data. Written by A. Needles, J. Mehi. Copyright VisualSonics 1999-2010